

## ABSTRACT

LI, LE. Membrane Arrangement of  $\alpha$ -Helices from the Transmembrane Domain of Cellulose Synthase Protein GhCesA1 from *Gossypium hirsutum*. (Under the direction of Prof. Smirnov).

Cellular membranes represent a highly heterogeneous and anisotropic environment that subjects membrane proteins to rather large gradients of local polarity that drives inter- and intra-residue hydrogen bonding and hydrophobic interactions. Accurate determination of polarity gradients experienced by transmembrane helices (TMHs) provides both the means for evaluating the TMH membrane structure and essential data on physical interactions responsible for helix-to-helix interactions. Such experimental data are important in view of the emerging plant CesaA computational models and recently solved crystal structures of related bacterial BcsA and BcsB complexes by Zimmer and coworkers. Here we report on the use of a battery of spin-labeling EPR methods to study membrane insertion and helix-to-helix interactions of CesaA TMH 4 and 5 using a biophysical model system. TMH 4 and 5 without the connecting loop were prepared using solid-state peptide synthesis, covalently modified with an EPR-active side chains at selected positions of the peptide sequence, and inserted into bilayers prepared from DOPC lipids. Local polarity experienced by the nitroxide-labeled side chains was measured based on the exquisite sensitivity of EPR parameters to dielectric and hydrogen-bonding effects. In addition, we found the charge state effected by pH also effect the aggregating behavior of TMH5 in membrane arrangement. Further, we investigated effects of membrane-spanning  $\alpha$ -helical WALP23 peptide on TMH5 membrane insertion and helix-to-helix interactions. Polarity and oxygen accessibility profiles for bilayers of the same lipid compositions were separately calibrated using WALP

peptide. One of the conclusions of this work is that the presence of various lipids and other membrane-spanning helices appears to be an important requirement for proper insertion of individual Cesa TMHs in lipid bilayers. Another conclusion is the interaction of the charged residues along the transmembrane peptide is dominant in the lipid bilayer.

© Copyright 2014 Le Li

All Rights Reserved

Membrane Arrangement of  $\alpha$ -Helices from the Transmembrane Domain of Cellulose  
Synthase Protein GhCesA1 from *Gossypium hirsutum*

by  
Le Li

A dissertation submitted to the Graduate Faculty of  
North Carolina State University  
in partial fulfillment of the  
requirements for the degree of  
Doctor of Philosophy

Chemistry

Raleigh, North Carolina

2014

APPROVED BY:

---

Alex Smirnov  
Committee Chair

---

Alexander Nevzorov

---

Reza Ghiladi

---

Edmond Bowden

## **DEDICATION**

To my family

## **BIOGRAPHY**

Le Li was born on February 8<sup>th</sup>, 1987 to Hui Zhou and Weiheng Li in one of the oldest cities in China, Xi'an. They wished her always be happy and named her Le meaning joyful in Chinese. She attended Xi'an Gaoxin No.1 High School and made lifetime and important friends here.

After eighteen years living in this ancient and beautiful city, she was accepted by one of the oldest universities in China, Tianjin University and majored in Pharmaceutical Sciences and Technology where she fell in love with protein chemistry. With the encouragement and support from Prof. Jin-Feng Wang, she spent almost two years in his laboratory and made up her mind to pursue a graduate study in the United States.

In August 2009, she enrolled in North Carolina State University in Raleigh and joined Prof. Smirnov's research group continuing her interesting in protein structure. Upon graduation, Le would like to start a biopharmaceutical industry career.

## **ACKNOWLEDGMENTS**

The following people are acknowledged for their contribution:

Prof. Alex Smirnov, Advisor;

Prof. Alex Nevzorov, Prof. Reza Ghiladi, Prof. Edmond Bowden, Prof. Yaroslava Yingling

for being a part of the advisory committee;

Prof. Maxim Voynov and Prof. Tatyana Smirnova for the many discussions and help;

Everyone in the Smirnov/Smirnova group and Nevzorov group;

Family and Friends-Hui Zhou, Weiheng Li, Dr. Chih-Yuan Chen, Shuang Liang, Dr. Zhi Xia

Ye, Lan Luo.

## TABLE OF CONTENTS

<b>LIST OF FIGURES</b> .....	<b>viii</b>
<b>LIST OF TABLES</b> .....	<b>xvi</b>
<b>LIST OF EQUATIONS</b> .....	<b>xvii</b>
<b>Chapter 1 General Introduction</b> .....	<b>1</b>
1.1 Importance of membrane proteins in biological systems .....	1
1.2 Introduction to CesA TMHs .....	3
1.3 Theoretic background.....	6
<b>Chapter 2 Experimental</b> .....	<b>19</b>
2.1 Materials .....	19
2.2 Spin labeling of TMH peptides with S-(2,2,5,5-tetramethyl-2,5-dihydro-1H-pyrrol-3-yl)methyl methanesulfonylthioate (MTSL).....	19
2.3 Reconstitution of MTSL-labeled TMH peptides into the lipid vesicles.....	20
2.4 Purification and lipid reconstitution of MTSL-labeled WALP23 peptides .....	21
2.5 Sucrose differential centrifugation of TMH peptides embedded in lipid bilayers .....	22
2.5 Reconstitution of native CesA TMHs to DOPC vesicles doped with 1 mol% of n-doxyl-PC lipid .....	22
2.6 Preparation of nickel(II)-EDDA complex (NiEDDA) .....	22
2.7 Circular Dichroism Spectroscopy of MTSL labeled CesA TMH peptides .....	25
2.8 Attenuated total reflectance (ATR) FT-IR spectroscopy .....	25
2.9 X-band (9.5 GHz) CW EPR spectroscopy .....	25
2.10 Pulsed saturation recovery (pSR) .....	26

2.11 EPR spectral line width broadening induced by molecular oxygen as measured by CW X-band EPR spectroscopy .....	26
2.12 Modeling the membrane hydrophobicity profile.....	27
<b>Chapter 3 Membrane insertion, orientation, and inter-helical oligomerization.....</b>	<b>29</b>
3.1 Introduction .....	29
3.2 Results and discussions .....	33
3.3 Conclusion.....	61
<b>Chapter 4 Ionization state of amino acid residues and inter-helical oligomerization .....</b>	<b>63</b>
4.1 Introduction .....	63
4.2 Results and discussions .....	65
4.3 Conclusion.....	79
<b>Chapter 5 Helices disaggregation mediated by an extrinsic membrane-spanning non-aggregating <math>\alpha</math>-helical peptide.....</b>	<b>81</b>
5.1 Introduction .....	81
5.2 Results and discussion.....	85
5.3 Conclusion.....	109
<b>APPENDICES .....</b>	<b>111</b>
<b>Appendix A TMH5 reconstitution into mixed lipid bilayers .....</b>	<b>112</b>
<b>Appendix B <math>\alpha</math>-Helical membrane-spanning WALP peptide as a reference for the determination of membrane arrangement of the transmembrane helices.....</b>	<b>121</b>
<b>Appendix C Reconstitution of Cesa TMH5 to Nanodiscs for EPR Study.....</b>	<b>136</b>
<b>Appendix D EPR Power Saturation Experiments at 77K.....</b>	<b>150</b>

**Appendix E References .....153**

## LIST OF FIGURES

Figure 1.1 Cysteine-specific spin label I, II, and III and the corresponding side chains R1, R2, and R3. ....	3
Figure 1.2 Freeze fracture replicas of rosettes associated with cellulose microfibril biogenesis.....	5
Figure 1.3 The hypothetical model for topology of one CesA protein subunit in the plasma membrane of plants.....	5
Figure 1.4 Predicted homology between putative TMHs in plant CesA and TMHs in BcsA. The homology based on protein sequence alignment is indicated by as the same colors. ....	6
Figure 1.5 Electron spin energy levels in a magnetic field.....	7
Figure 1.6 The hyperfine interaction between an electronic spin $S=1/2$ and a nuclear spin $I = 1$ nucleus results in six energy levels and 3 allowed electronic (transitions labeled $k$ , $l$ and $m$ ) in place of the original two. ....	9
Figure 1.7 Membrane depth measurements by SDSL-EPR, from accessibility measurements. ....	11
Figure 3.1 Room temperature X-band (9.5 GHz) EPR spectra of: (A) TFE solution of SL-TMH5 L13C containing residuals of TFA revealed no detectable nitroxide signals; (B) from the same solution after 24 hrs. neutralization with TEA; (C) Non-aggregating WALP23 C12 with MTSL and incorporated into DOPC multilamellar vesicles (MLVs) at pH = 7.0. ....	35
Figure 3.2 Circular dichroism spectra: (A) TMH5 V9C (solid line), SL-TMH5 V9C peptides (dotted line), TMH4 L7C (dash-dotted line), SL- TMH4 L7C (dashed line) in TFE solution; (B) CD spectra of SL-TMH5 V9C peptide (dashed line) and SL- TMH4 L7C (solid line) in	

100 nm unilamellar DOPC vesicles.....	37
Figure 3.3 Decomposition of X-band (9.5 GHz) EPR spectra acquired from MTSL-labeled TMH5 L13C in the fluid phase bilayers of different lipid composition: (A) DOPC (room temperature); (B) DLPC (room temperature); (C) DMPC (34 °C); (D) DPPC (48 °C).....	41
Figure 3.4 Room temperature X-band (9.5 GHz) EPR spectra acquired from series of SL-TMH4 (A) and SL-TMH5 (B) variants reconstituted to the DOPC bilayer. ....	42
Figure 3.5 (A) A photograph of the centrifuge tube taken after the 3% sucrose separation of SL-TMH5 L13C peptide reconstituted to DOPC lipids. (B) ATR FT-IR spectra from the individual layers obtained after the sucrose separation of the native TMH5 peptide reconstituted to DOPC lipids (top layer, dotted line; bottom layer, dash-dotted line). FT-IR spectrum of the DOPC-embedded native TMH4 is shown in dashed line. The spectrum of the reference MTSL-labeled WALP23 C10 is shown in solid line.....	45
Figure 3.6 Room temperature <sup>31</sup> P solid NMR spectra from the membrane-embedded TMH4 (A) and the top layer (B) and bottom layer (C) obtained after sucrose centrifugation of TMH5 reconstituted in DOPC bilayers. ....	46
Figure 3.7 X-band EPR spectra from the individual layers obtained after sucrose differential centrifugation of SL-TMH5 variants reconstituted to DOPC lipids: top layer (solid line), bottom layer (dashed line). ....	47
Figure 3.8 X-band (9.5 GHz) EPR spectra acquired from SL-TMH4 C2 (A) and SL-TMH5 C23 (top layer collected after sucrose separation) (B) magnetically diluted with corresponding native TMH peptides in 1:1, and 1:4 ratios (see text inset) at 140K.....	48
Figure 3.9 Oxygen line width and polarity profile of TMH4 and 5 in DOPC membrane.....	52

Figure 3.10 Chemical structures of spin-labeled phospholipids 12-doxyl-PC and 16-doxyl-PC.....	56
Figure 3.11 (A) X-band (9.5 GHz) EPR spectra of N <sub>2</sub> -equilibrated DOPC vesicles doped with 1 mol% of 12-doxyl-PC measured in the absence (dotted line) and presence (solid line) of CesA TMH5. The spectra were measured at 11 °C and pH = 7.0 for the peptide-to-lipid ratio of 1:25. ....	57
Figure 4.1. Circular dichroism spectra of MTSL-labeled CesA TMH5 V9C peptide in 100 nm unilamellar DOPC vesicles equilibrated with buffers at pH = 7.0 (dashed line) and pH = 3.3 (solid line). ....	67
Figure 4.2 ATR FT-IR spectra from the top layers obtained after the sucrose centrifugation of native TMH5 in 100 nm unilamellar DOPC vesicles equilibrated at pH = 7.0 (solid line) and pH = 3.3 (dashed line), respectively.....	68
Figure 4.3 Decompositions of series of X-band (9.5 GHz) EPR spectra acquired from a spin-labeled TMH5 L13C mutant in DOPC lipids hydrated with buffer solutions at pH = 3.3 (A), pH = 5.6 (B) and pH = 7.0 (C). ....	70
Figure 4.4 Room temperature X-band (9.5 GHz) EPR spectra acquired from serious MTSL-CesA TMH5 mutant in DOPC bilayer at pH = 3.3. ....	71
Figure 4.5 (A) X-band (9.5 GHz) EPR spectra of N <sub>2</sub> -equilibrated DOPC vesicles doped with 1 mol% of 12-doxyl-PC measured in the absence (dotted line) and presence (solid line) of CesA TMH5. (B) Zoom-in low field components of the same spectra. ....	73
Figure 4.6. Line width broadening induced by oxygen and polarity profiles of TMH5 in DOPC vesicles at pH = 7.0 and pH = 3.0. ....	75

Figure 4.7. A cartoon illustrating the effect of pH (of the ionization state of the TMH5 helices) on the interhelical association. (A): pH = 7.0 (zwitterionic form); (B): pH = 3.3 (positively charged form)..... 77

Figure 5.1 Helical wheel of diagram of TMH5. .... 82

Figure 5.2 Series of X-band (9.5 GHz) EPR spectra acquired from nitrogen-equilibrated TMH5 spin-labeled at various positions (A) in DOPC vesicles equilibrated at pH = 7.0 (top layer obtained after sucrose separation); (B) in DOPC vesicles co-inserted with WALPL23 L8S peptide at pH = 7.0; (C) in DOPC vesicles co-inserted with WALP23 L8S peptide at pH = 3.3. .... 89

Figure 5.3 Decompositions of series of X-band (9.5 GHz) EPR spectra acquired from a spin-labeled TMH5 L13C mutant co-inserted with WALPL8S peptide in DOPC lipids hydrated with buffer solutions at pH = 3.3 (A), and pH = 7.0 (B). Top spectra are experimental spectra. Middle and bottom ones are decomposed two components. .... 90

Figure 5.4 (A): $\Delta H(0)_{p-p}^{-1}$  versus the label position in TMH5 co-inserted with WALP23 L8S peptide at pH = 7.0 ( $\circ$ ) and pH = 3.3 ( $\bullet$ ) in DOPC vesicles. A comparison of SL-TMH5 embedded into DOPC bilayer without WALP23 L8S co-insertion pH = 7.0 ( $\square$ ) and pH = 3.3 ( $\blacksquare$ ) is shown. (B): Amplitude of central component versus the label position in TMH5 co-inserted with WALP23 L8S peptide in DOPC vesicles. .... 93

Figure 5.5 Overlapped  $\Delta\Delta B_{p-p}^L$  vs. labeling position plots for SL-TMH5 co-inserted with 3 fold molar excess of WALP23 L8S in DOPC vesicles at pH = 3.3 ( $\bullet$ ) and pH = 7.0 ( $\circ$ ), SL-WALP23 in DOPC ( $\blacksquare$ ) and DLPC ( $\square$ ) vesicles..... 96

Figure 5.6 Rigid-limit (77K) CW X-band EPR spectra of SL-TMH5 L13C co-inserted with

three-fold excess of WALP23 L8S peptide in DOPC bilayers at pH = 3.3 (solid line) and pH = 7.0 (dashed line). .....	97
Figure 5.7 (A): Anisotropic nitrogen hyperfine coupling constants $A_{zz}$ acquired from X-band CW EPR of MTSL-labeled TMH5 peptides co-inserted with three-fold excess of WALP23 L8S peptide in DOPC bilayers at pH = 3.3 (●) and pH = 7.0 (○) and MTSL-labeled WALP23 peptides in DOPC (■) vesicles (pH = 7.0). (B): Anisotropic $A_{zz}$ coupling constants for MTSL-labeled WALP23 in DOPC (■) and DLPC (□) bilayers. ....	98
Figure 5.8. Spin label reduction with ascorbic acid experiment with continuous N <sub>2</sub> flow... 103	103
Figure 5.9. Central EPR spectral component intensity decay for MTSL-labeled WALP23 peptides in DOPC induced by five-fold molar excess of ascorbic acid at pH = 3.3 and under continuous N <sub>2</sub> flow (21.5 °C). ....	105
Figure 5.10 Reduction of MTSL-labeled Cesa TMH peptides co-inserted with 3-fold excess of WALP C8S in DOPC bilayers with ascorbic acid. ....	108
Figure A1. Room temperature X-band CW EPR of MTSL-labeled Cesa TMH5 embedded in DOPC/DOPC (4:1) vesicles at pH = 3.3.....	113
Figure A2. $\Delta B(0)_{p-p}^{-1}$ for TMH5 peptides in DOPC/DLPC (4:1) bilayer plotted against the label positions. ....	114
Figure A3. (A) Central EPR line width broadening $\Delta \Delta B_{p-p}^L$ induced by oxygen and (B) polarity profile of TMH5 (pH = 3.3) in DOPC/DLPC (4:1) vesicles. ....	116
Figure A4. Chemical structures of the spin-labeled DLPC lipid. ....	117
Figure A5 (A): Room temperature X-band CW EPR spectra of DOPC/DLPC (4:1) vesicles doped with the spin-labeled DLPC, pH = 3.3. (B): DOPC vesicles doped with 20 mol % of	

Tempo-POPC, pH = 3.3.....	119
Figure A6. Room temperature X-band CW EPR spectra of DOPC/DLPC (4:1) bilayers containing 10 mol % of SL-DLPC (A) and DOPC bilayers doped with only 1 mol % of SL-DLPC (B) are shown in a solid line. Dashed line - in the present of native Cesa TMH5 at pH = 3.3. ....	120
Figure B1. Circular dichroism spectra of SL-WALP23-C12 peptide in the bilayers composed of DOPC (solid line) and DLPC (dashed line). Peptide concentrations were the same. ....	123
Figure B2. First 10 $\mu$ s of the experimental pulse saturation recovery curves of MTSL-WALP23-C4 in the presence and absence of relaxing agents.....	124
Figure B3. Room temperature relaxation rates acquired from the saturation recovery pulsed EPR experiments for the spin-labeled WALP23 peptide reconstituted into DOPC (A) or DLPC (C) bilayers. (B) Comparison of relaxation rate enhancement by air for MTSL-WALP23 in DOPC bilayers (●) (room temperature, this study) and data reported by Nielsen <i>et al</i> <sup>28</sup> (△) (Solid line represent the fits of the experimental data acquired from this work). For the calculation of distance from the center of the bilayer (top X axis) see the Experimental Section. (D) Relaxation rate enhancement by air for MTSL-WALP23 in DLPC bilayers, room temperature. ....	125
Figure B4. Overlap of $\Delta B_{p-p}^L$ profiles (●) acquired from X-band CW EPR with the relaxation rate profiles (◉) acquired from pulsed saturation recovery EPR for the spin-labeled WALP23 in DOPC (A) and DLPC (B) vesicles. ....	128
Figure B5. Rigid-limit EPR spectra (77K) of MTSL-WALP23-C23 in DOPC bilayers overlapped with the simulated high- and low-field components shown in red. ....	130

Figure B6. The anisotropic nitrogen hyperfine coupling constant  $A_{zz}$  for SL-WALP23 peptide in DOPC (○) and DLPC (●) bilayers. Solid line represents the fit of the experimental data to the Equation 2.3. .... 131

Figure B7 Helical wheel projection for WALP23 peptide. Residues above the solid line seems to belong to the peptide face involved into association with another peptide molecule. .... 132

Figure B8. A cartoon illustrates the proposed arrangement of the N-terminal and C-terminal domains of the WALP23 peptide in the DLPC bilayers. .... 133

Figure C1. This cartoon illustrates the structure of nanodiscs (generated by the PyMOL Molecular Graphics system) modeled using POPC as a lipid. .... 137

Figure C2. SDS-page of MSP1 purification fractions. .... 139

Figure C3. Cartoon illustrates the preparation of nanodiscs. .... 140

Figure C4. Characterization of POPC nanodiscs. .... 141

Figure C5. SEC purification of DOPC nanodiscs obtained at MSP1-to-DOPC molar ratio of 1:70 (A) and 1:100 (B). .... 143

Figure C6. Characterization of DOPC nanodiscs. .... 143

Figure C7. SEC purification of DOPC nanodiscs (MSP1:DOPC lipids = 1:50) assembly mixture containing MTSL labeled Cesa TMH5 L13. .... 145

Figure C8. Dynamic light scattering size distribution for MTSL-labeled Cesa TMH5 L13 DOPC nanodiscs with peptide introduced with TFE ((A); for the elution profile see Figure C7, black trace) and without TFE ((B), black, for the elution profile see Error! Reference source not found., red trace). The DLS data for the purified nanodiscs containing TMH5 are

shown in red (B).....	146
Figure C9. Room temperature X-band EPR spectrum of MTSL labeled Cesa TMH5 L13 DOPC nanodiscs, pH = 7.0. MSP1:peptide molar ratio was 2:1.....	147
Figure C10. Characterization of MTSL-Cesa TMH5 L13C peptide reconstituted into DOPC nanodiscs.....	148
Figure C11. Room temperature X-band EPR spectrum of the purified fractions collected at about 50 mL (A) and 60 mL (B) for MTSL labeled Cesa TMH5 L13/DOPC nanodiscs, pH = 7.0. MSP1: peptide molar ratio was 5:1.....	149
Figure D1. An $A_{zz}$ vs. $B_1$ plots for MTSL-WALP peptides embedded into DOPC membrane at 77K.....	151
Figure D2. An $A_{zz}$ vs. $B_1$ plots for 1mM MTSL in a frozen glass (water-glycerol mixture at 40:1 v/v ratio) and in toluene at 77K. The solvents are indicated in the inset.....	151
Figure D3. (A) An $A_{zz}$ vs. $B_1$ plot for 1mM PDT in isopropanol- $d_8$ at 77K. The corresponding power saturation curves for the low-field component (B) and the central component (B) for 1mM PDT in an isopropanol- $d_8$ at 77K.....	152

## LIST OF TABLES

Table 2.1 One-letter sequence and mass spectroscopy data for spin labeled CesATMH4 peptides .....	23
Table 2.2. One-letter sequence and mass spectroscopy data for spin labeled CesA TMH5 peptides .....	23
Table 2.3. One-letter sequence and mass spectrometry data for spin-labeled WALP23 peptides .....	24
Table 3.1 Calculated broadening of SL-TMHs relative to the 1:4 magnetic diluted spectra at 140K.....	50
Table 5.1 Reduction rate constants of SL-WALP23 peptides in DOPC membrane by ascorbic acid at 21.5 °C.....	105
Table 5.2 Reduction rate constants of SL-TMH5 co-inserted with 3 fold WALPL8S in DOPC membrane by ascorbic acid at 21.5 °C. ....	107
Table B1. Optimal least-square fit to Equation 2.3 parameters calculated from various methods.....	128

## LIST OF EQUATIONS

Equation 1.1 .....	7
Equation 1.2 .....	8
Equation 1.3 .....	8
Equation 1.4 .....	12
Equation 1.5 .....	12
Equation 1.6 .....	13
Equation 1.7 .....	13
Equation 1.8 .....	13
Equation 1.9 .....	14
Equation 1.10 .....	14
Equation 1.11 .....	14
Equation 1.12 .....	14
Equation 1.13 .....	15
Equation 1.14 .....	15
Equation 1.15 .....	15
Equation 1.16 .....	15
Equation 1.17 .....	16
Equation 1.18 .....	16
Equation 1.19 .....	16
Equation 1.20 .....	16
Equation 1.21 .....	17

Equation 1.22 .....	17
Equation 1.23 .....	17
Equation 1.24 .....	17
Equation 1.25 .....	17
Equation 1.26 .....	17
Equation 2.1 .....	27
Equation 2.2 .....	28
Equation 2.3 .....	28
Equation 3.1 .....	58
Equation 5.1 .....	102

## Chapter 1 General Introduction

### 1.1 Importance of membrane proteins in biological systems

Biological membranes are essential structures of all the living cells. Although these membranes are only about 4 nm thick, they are maintaining the integrity of the cell, its homeostatic environment, and are responsible for many biochemical processes, such as molecular transport, cellular signaling and recognition, intercellular fusion, to name a few<sup>1-4</sup>.

The dominating compositions of membranes are the lipids and proteins. Lipid is an amphiphilic molecule that consists of a polar headgroup and the hydrophobic acyl chain. In an aqueous environment lipids spontaneously arrange into bilayers with the hydrophobic chains shielded from polar environment while the hydrophilic head groups are exposed to the outside aqueous phase<sup>5</sup>. Lipids bilayers with embedded integral membrane proteins form a sharp interface between the cell interior and aqueous environment<sup>6-7</sup>.

In biological membranes lipid chains are disordered and highly dynamic, and only the time-averaged structure could be defined probabilistically<sup>8</sup>. Together with the membrane, membrane proteins play a vital role in many biological functions. Several classes of membrane proteins are involved in biological processes: structural proteins stabilize the cell, cell recognition proteins are responsible for the intracellular interactions, enzymatic proteins produce essential chemicals which maintain the living system, and transport proteins help to modulate the concentration of some small molecules within the cell<sup>6, 8</sup>. There are two ways to associate these proteins with the membrane: one is through permanent attachment, and the other is through a temporary contact with the membrane. The permanently attached proteins

are either associated with only one membrane leaflet or span the entire membrane. The latter are called transmembrane proteins whose transmembrane domains are usually arranged as  $\alpha$ -helices or  $\beta$ -barrels. Temporarily associated membrane proteins are attached to an integral protein or the lipids through electrostatic and hydrophobic interactions<sup>9</sup>.

Studying of membrane proteins, especially their structure-function relationships, is an important task for many reasons. About 25-30% of Human genome encodes for the membrane proteins<sup>4, 9-10</sup>. Currently, only 476 unique structures of membrane proteins have been solved and the number is growing exponentially but at significantly slower rate than for water soluble proteins that constitute > 99% in the protein data base (PDB)<sup>11-12</sup>.

Among other biophysical methods, electron paramagnetic resonance (EPR) spectroscopy in combination with site-directed spin-labeling (SDSL) technique has been proven to be a powerful tool for probing the structural and dynamic information in biological system; this method is especially useful in membrane proteins studies<sup>13-15</sup>. The basic the procedure is as follows: a native residue (or a series of residues) is selected and mutated to cysteine and followed by a chemical modification with sulfhydryl specific nitroxide radical<sup>16</sup>. Commonly used nitroxide labels are showed in Figure 1.1. In this work we utilized a broad arsenal of EPR methods in combination with spin-labeling technique to obtain information on the transmembrane structure of cellulose synthase transmembrane helices (CesA TMHs).

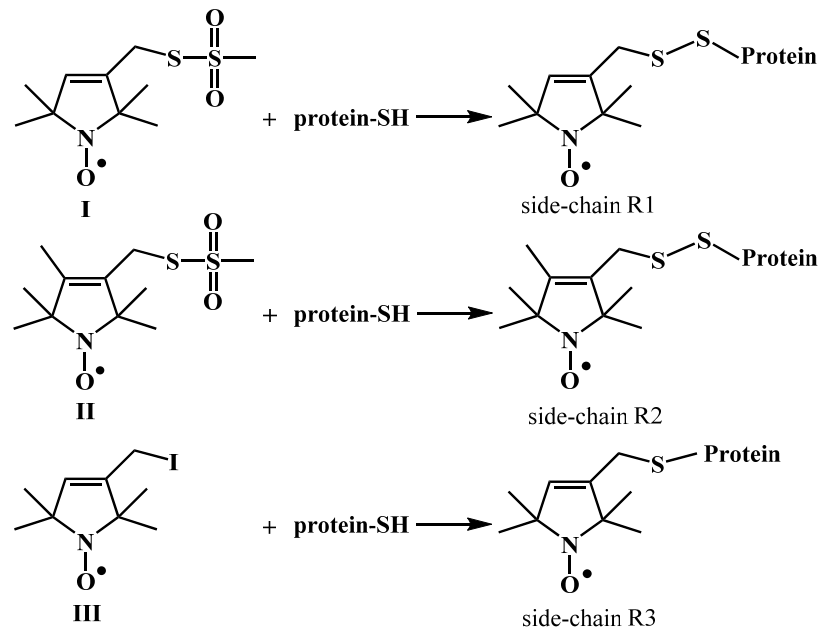


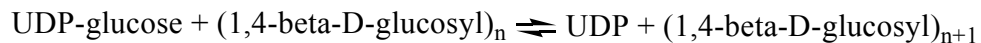
**Figure 1.1** Cysteine-specific spin label I, II, and III and the corresponding side chains R1, R2, and R3.<sup>16</sup>

## 1.2 Introduction to Cesa TMHs

Cellulose is the most abundant biopolymer in nature<sup>17-18</sup>. Recently, the complex crystal structure of cellulose synthase protein complex including one uridine diphosphate (UDP) molecule and a translocating glucan from *Rhodobacter sphaeroids* (BcsA) was reported<sup>19</sup>. This structure demonstrates that transmembrane helices (TMHs) play an important role in translocation of the glucan chain. The structure of the plant cellulose synthase (CesA) proteins is predicted to be similar to BcsA. Specifically, CesA is predicted to have two transmembrane helices (TMHs) in the N-terminal region and six in the C-terminal region from hydrophathy plots.

Despite this progress, detailed mechanism of cellulose biosynthesis in plant is still unclear<sup>20</sup>. So far, it is known that cellulose is synthesized in plasma membrane by a complex of terminal proteins<sup>21</sup>. Cellulose synthase catalytic subunit (CesA) is the only known protein localized in the rosette complex<sup>17</sup>. As it could be seen from the images obtained by freeze-fracture electron microscopy (Figure 1.2), six CesA catalytic subunits are assembled into rosettes with apparent hexagonal symmetry<sup>17, 22</sup>. A computational 3D structure of the cytosolic domain of the plant cellulose synthase protein (GhCesA1 from cotton, *Gossypium hirsutum*) was published recently<sup>23</sup>. However, structure of the transmembrane domain is still missing. Detailed biophysical studies of CesA are complicated because of the absence of the crystal structure proper experimental protocols for CesA over-expression<sup>21</sup>.

The main biological function of cellulose synthase is the catalytic elongation of the polymer chains built of 1,4-beta-D-glucosyl residues<sup>18</sup>:



Currently, it is believed that the substrate – UDP-glucose – binds to the active site on the cytoplasmic side of the membrane, while the produced glucan chain traverses the membrane and accumulates within the cell wall in plants<sup>21</sup>. Therefore, a tentative model of a single CesA subunit in the membrane (Figure 1.3) predicts that the TMHs would interact to form a central pore through which the glucan could be secreted<sup>17</sup>. Computational studies show that TMHs are amphipathic, with the hydrophobic residues facing the lipid phase, leaving the hydrophilic surfaces facing the central part of the pore. Similar models were proposed for proton and Ca<sup>2+</sup> ATPases that also arranged into complexes exhibiting a hexagonal symmetry<sup>17</sup>.

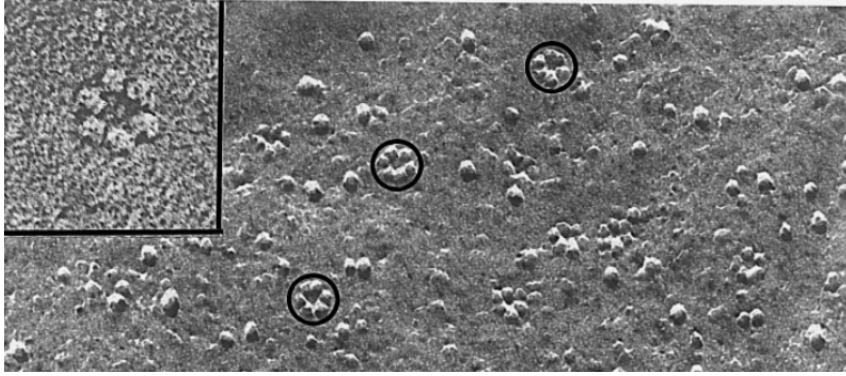


**Figure 1.2** Freeze fracture replicas of rosettes associated with cellulose microfibril biogenesis.<sup>17</sup>

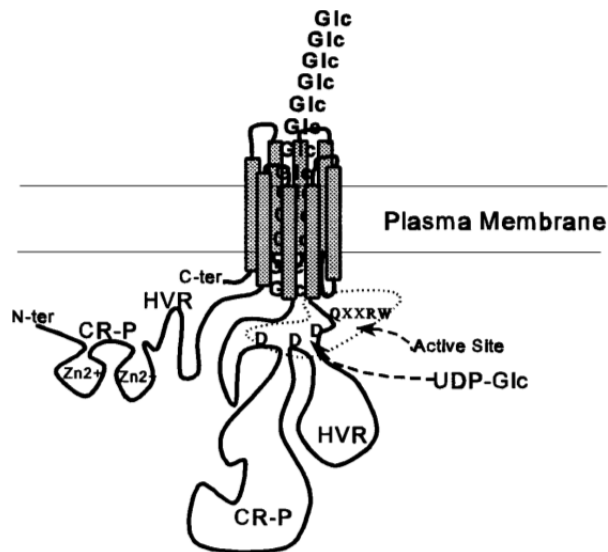


**Figure 1.3** The hypothetical model for topology of one CesA protein subunit in the plasma membrane of plants.<sup>17</sup>

For EPR studies described in this thesis, the CesA TMHs 4 and 5 were chosen as they have been predicted most likely to interact with each other when embedded into lipid membranes. A 12-member library of Cys mutants of TMHs 4 and 5 was designed and peptides were synthesized through a solid phase peptide synthesis by Synbiosci (San Francisco, CA). Using SDSL-EPR, we have carried out a series of experiments to detect the transmembrane insertion pattern and confirm the self-assembling of these two TMHs.

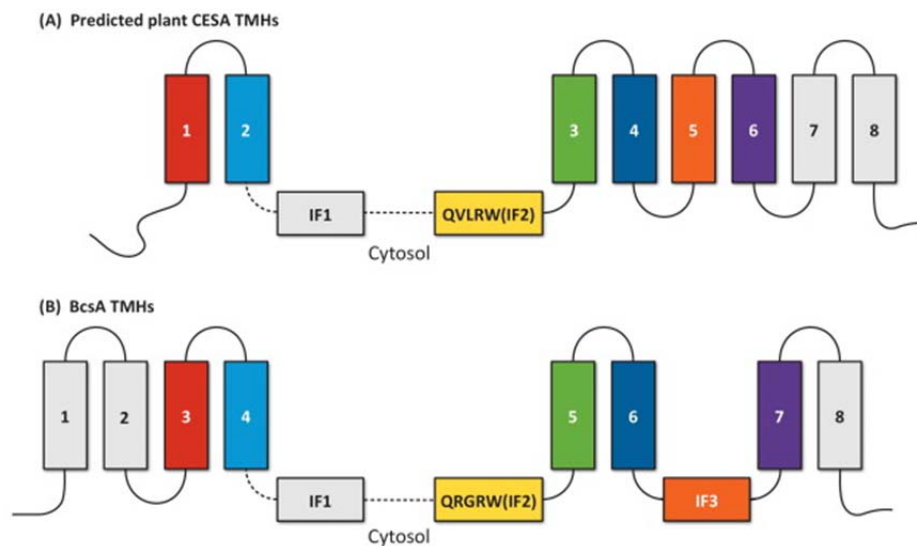


**Figure 1.4** Predicted homology between putative TMHs in plant CesA and TMHs in BcsA. The homology based on protein sequence alignment is indicated by as the same colors.<sup>20</sup>

### 1.3 Theoretic background

#### 1.3.1 An introduction to EPR

EPR is a spectroscopic technique to characterize molecular species that have unpaired electrons. It can detect transitions induced by electromagnetic radiation between energy

levels of electron spins in the presence of static magnetic field. Electron has spin  $S=1/2$  with projection quantum number  $m_s = \pm 1/2$ . In the absence of external magnetic field, the states of  $m_s = 1/2$  and  $m_s = -1/2$  are degenerate. When an external magnetic field,  $B_0$ , is applied, the degeneracy is lifted: the state with  $m_s = 1/2$  moves up in energy  $(1/2)g_e\mu_B B_0$  and the other state with  $m_s = -1/2$  moves down by  $(1/2)g_e\mu_B B_0$  (the Zeeman effect) (Figure 1.5)<sup>24</sup>. The separation between the two energy levels of an electron spin in a magnetic field  $B_0$  is,

$$\Delta E = g_e \mu_B B_0 \quad \text{Equation 1.1}$$

where  $\mu_B$  is the *Bohr* magneton.  $g_e$  is the electronic g-factor:  $g_e = 2.002319$ . The exact value of  $g_e$  is determined by relativistic effects and interactions of the electron with the electromagnetic fluctuations of the vacuum that surround the electrons<sup>24</sup>.

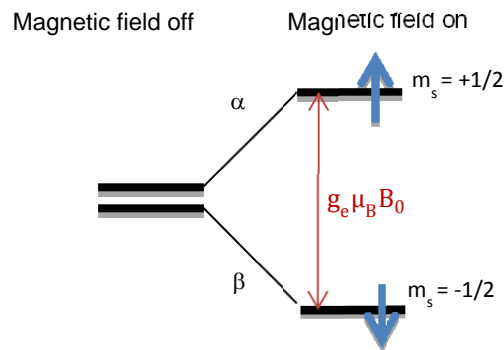


**Figure 1.5** Electron spin energy levels in a magnetic field.<sup>24</sup>

Magnetic moment of the electron can flip from the state with a lower energy level to the one with a higher energy when the electron absorbs an electromagnetic radiation with frequency  $\nu$  and energy  $\varepsilon = h\nu$ , provided that the resonance condition  $\varepsilon = \Delta E$  is fulfilled.

Thus, the resonance condition for EPR is given by:

$$h\nu = g_e\mu_B B_0 \quad \text{Equation 1.2}$$

Most of the commercial EPR spectrometers operate at resonance frequency of *ca.* 9-10GHz (that falls within X-band microwave band), then the resonant magnetic field of for species with  $g \approx 2$  is *ca.* 0.3 T and such a field is readily obtained with an electromagnet.

EPR experiments can be carried out in continuous wave (CW) and pulsed modes. In CW EPR, the frequency of photon radiation on the sample is fixed while the external magnetic field sweeps through the resonance conditions. The difference in spin populations between the two energy levels, which are initially in the thermal equilibrium with the lattice, is given by the Boltzmann distribution that is function of the, energy splitting ( $\Delta E$ ) and temperature (T). (Note that in magnetic resonance the following notations of spin states are used interchangeably:  $|+\frac{1}{2}\rangle = |+\rangle = |\alpha\rangle$ ,  $|-\frac{1}{2}\rangle = |-\rangle = |\beta\rangle$ .)

$$\frac{N_\alpha}{N_\beta} = e^{-\Delta E/kT} \quad \text{Equation 1.3}$$

At the resonance condition the rate of transitions from the lower to the higher spin states are higher than the reverse. If the spin system remains at thermal equilibrium with the lattice, thus, there is a net absorption of energy. This absorption is detected electrically and converted into the EPR spectrum. Most EPR spectra are recorded in form of first derivative by phase-sensitive detection using modulation of the external magnetic field at *ca.* 100 kHz.

The g-factor of an electronic spin confined to an ion or an organic molecule is different from  $g_e \approx 2.0023$  because of local magnetic fields induced by orbital effects as well as other spins in the immediate molecular environment. However, for organic radicals, the g-

factors are very close to 2.0023, since the unpaired electron has very little orbital contribution to the magnetic moment. Because the spin magnetic moment for the electron is constant (approximately the *Bohr* magneton), the deviation of g-factor from  $g_e$  is mainly induced by spin-orbit coupling (interaction of the spin with orbital angular momentum of the unpaired electron).

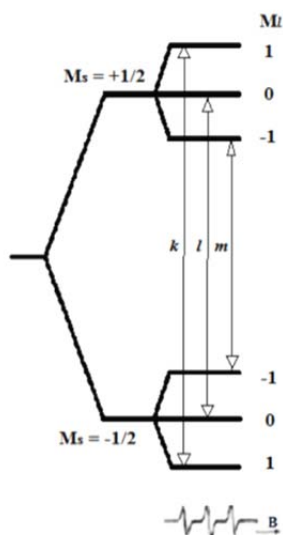


**Figure 1.6** The hyperfine interaction between an electronic spin  $S=1/2$  and a nuclear spin  $I = 1$  nucleus results in six energy levels and 3 allowed electronic (transitions labeled  $k, l$  and  $m$ ) in place of the original two.<sup>25</sup>

Another important feature of the EPR spectra is the splitting of the resonance lines, which is called the hyperfine coupling splitting. The source of the hyperfine splitting is the magnetic interaction between the electronic spin and the nuclear spins nearby. The nitroxide labels employed in this PhD thesis project possess an electronic spin that is delocalized

primarily over N-O moiety. The most abundant  $^{16}\text{O}$  has no nuclear spin while the abundant  $^{14}\text{N}$  atom possesses nuclear spin  $I=1$ . The latter spin  $I=1$  splits the EPR spectrum into three additional lines (Figure 1.6). The general line splitting rule is  $2I + 1$ .

### **1.3.2 Solvent accessibility of a nitroxide side chain measured by EPR**

Solvent accessibilities of nitroxide side chain in a macromolecule measured by SDSL-EPR can be used to map structure and serve to compare and confirm the structure of a protein obtained from a crystal or a computational model<sup>13, 26-27</sup>. The larger solvent accessibility of the nitroxide labels indicates an exposed labeled site. Thus, plotting the EPR accessibility parameters for residues along a helix or for different positions in the protein vs. the residue position in the protein sequence would provide instructive information even without knowing the detailed structure at atomic level (Figure 1.7)<sup>28-29</sup>. Membrane depth could also be measured through compared different accessibility between non-polar and polar paramagnetic exchange reagents (Figure 1.7)<sup>28-29</sup>.

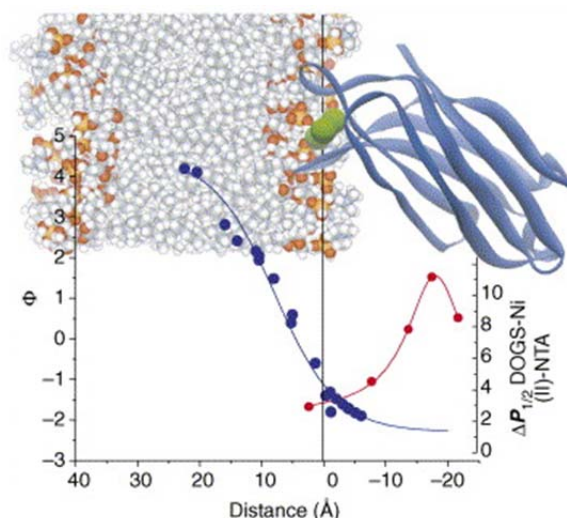


**Figure 1.7** Membrane depth measurements by SDSL-EPR, from accessibility measurements. The blue line represents a depth parameter,  $\Phi$ , obtained from measurements with paramagnetic NiEDDA and molecular oxygen. The red line shows the variation in the progressive power saturation parameter,  $\Delta P_{1/2}$ , for a paramagnetic lipid metal chelate (DOGS-Ni(II)-NTA) as a function of distance into the aqueous phase.<sup>13</sup>

The magnitude of the accessibility of a nitroxide side chain in a macromolecule depends on the Heisenberg exchange rate ( $W_{ex}$ ) of the probe with a paramagnetic exchange reagent in solution, see Equation 1.4 below<sup>30</sup>. Paramagnetic exchange reagents such as paramagnetic metal ion complexes, molecular oxygen, or another nitroxide could be employed in the accessibility measurement<sup>15</sup>. When the electronic spin-lattice relaxation time of the reagent, like  $O_2$  or NiEDDA, is much shorter than the spin-lattice relaxation time of the nitroxide ( $T_{1e}$ ), the contributions from the dipolar interaction can be neglected and the Heisenberg exchange (HE) would be the prevailing spin-spin relaxation mechanism for the

nitroxide. Heisenberg exchange will affect both spin-spin and spin-lattice relaxation but spin-lattice relaxation time is longer and it is easier to measure in pulsed EPR experiment.

The exchange rate  $W_{\text{ex}}$  can be measured as:

$$W_{\text{ex}} = \left[ \frac{1}{T_{1e}(\text{R})} - \frac{1}{T_{1e}(\text{O})} \right] \quad \text{Equation 1.4}$$

where  $T_{1e}(0)$  is the nitroxide intrinsic spin-lattice relaxation time, and  $T_{1e}(\text{R})$  is the effective spin-lattice relaxation time in the presence of an exchange reagent. Measuring a difference in the effective  $T_{1e}$  will provide relative values of  $W_{\text{ex}}$ . Two methods for measuring  $T_{1e}$  are commonly used: (1) continuous wave (CW) power saturation under condition of  $W_{\text{ex}} \ll 1/T_{2e}$ , where  $T_{2e}$  is the spin-spin relaxation time, and (2) saturation recovery measurements, which require pulse EPR instrumentation. In the first method, the nitroxide saturates in a homogeneous fashion. The pulse saturation recovery experiment, however, provides a more direct measurement of  $T_{1e}$ . For SDSL-EPR methods applied to peptides and proteins studies with  $T_{1e} < \tau_C$ , measurement of the spin-spin relaxation ( $T_{2e}$ ) could also provide means to measure  $W_{\text{ex}}$ . Details of the underlying theory will be presented in the following sections.

### 1.3.3 Brief theory of Heisenberg spin exchange and nitroxide side-chain accessibility<sup>26</sup>

The Heisenberg exchange (HE) rate,  $W_{\text{ex}}$ , between a small nitroxide (N) in solution and an exchange reagent R, is given by,

$$W_{\text{ex}} = k_{\text{ex}} C_{\text{R}} \quad \text{Equation 1.5}$$

where  $k_{\text{ex}}$  is the exchange rate constant and  $C_{\text{R}}$  is the concentration of R. In the strong exchange limit, when the Heisenberg exchange is diffusion controlled,  $k_{\text{ex}}$  is given by (in L

mol<sup>-1</sup> s<sup>-1</sup> unit),

$$\mathbf{k}_{\text{ex}} = \mathbf{P}_{\text{max}} \mathbf{f} \mathbf{k}_{\text{D}} = \mathbf{P}_{\text{max}} \mathbf{f} 4 \pi (\mathbf{N}_{\text{A}}/1000) (\mathbf{D}_{\text{N}} + \mathbf{D}_{\text{R}}) \mathbf{r}_{\text{c}} \quad \text{Equation 1.6}$$

where

$$\mathbf{k}_{\text{D}} = 4 \pi \left( \frac{\mathbf{N}_{\text{A}}}{1000} \right) (\mathbf{D}_{\text{N}} + \mathbf{D}_{\text{R}}) \mathbf{r}_{\text{c}} \quad \text{Equation 1.7}$$

is the diffusion-controlled rate constant,  $\mathbf{P}_{\text{max}}$  is the maximum exchange efficiency,  $\mathbf{f}$  is the “steric factor”, and  $\mathbf{D}_{\text{N}}$  and  $\mathbf{D}_{\text{R}}$  are the diffusion constants for the nitroxide and a reagent, respectively,  $\mathbf{r}_{\text{c}}$  is the collision radius which is the sum of the effective radii of the nitroxide ( $\mathbf{r}_{\text{N}}$ ) and reagent ( $\mathbf{r}_{\text{R}}$ ).  $\mathbf{P}_{\text{max}} = 1$  in the case of  $\text{O}_2$  or NiEDDA as the reagent, since the encounters are in the strong exchange limit and  $\mathbf{T}_{\text{IR}} < \tau_{\text{c}}$ .

When a nitroxide is tethered to a protein, the translational diffusion coefficient is assumed to equal to that of the protein itself and, therefore, is comparatively very small *vs.* the diffusion coefficient of the smaller relaxation agent in the solution. Thus,  $\mathbf{D}_{\text{N}} + \mathbf{D}_{\text{R}} \approx \mathbf{D}_{\text{R}}$ . However, the rotational degrees of freedom of the tethered nitroxide are retained. Parameter  $\mathbf{r}_{\text{c}}$  remains the same due to the same colliding species involved (between R and the nitroxide), but the local environment of protein and the interactions of the nitroxide with the protein would cause a reduction in collisions compared to the free nitroxide. All these factors are taken into account by the “accessibility factor”,  $\rho$ . Thus, the HE rate for a protein-associated nitroxide in the strong exchange limit is given by,

$$\mathbf{W}_{\text{ex}}^{\text{P}} = \rho \mathbf{f} 4 \pi (\mathbf{N}_{\text{A}}/1000) \mathbf{D}_{\text{R}} \mathbf{r}_{\text{c}} \mathbf{C}_{\text{R}} \quad \text{Equation 1.8}$$

Dividing Equation 1.8 by Equation 1.5 with  $\mathbf{k}_{\text{ex}}$  substituted by Equation 1.6, we can obtain the accessibility factor,  $\rho$ ,

$$\rho = \frac{W_{\text{ex}}^{\text{P}}/C_{\text{ex}}^{\text{P}}}{W_{\text{ex}}/C_{\text{ex}}} - \frac{D_{\text{R}} + D_{\text{N}}}{D_{\text{R}}} \quad \text{Equation 1.9}$$

where

$$k_{\text{ex}}^{\text{P}} = W_{\text{ex}}^{\text{P}}/C_{\text{ex}}^{\text{P}} \quad \text{Equation 1.10}$$

$$k_{\text{ex}} = W_{\text{ex}}/C_{\text{ex}} \quad \text{Equation 1.11}$$

are defined.  $C_{\text{ex}}^{\text{P}}$  and  $C_{\text{ex}}$  are the concentrations of R at the corresponding conditions. Thus, for a small, electrically neutral but polar exchange reagent,  $\rho = 0$  when the nitroxide is buried in the protein interior and  $\rho = 1$  when it is located at the solvent exposed site.

### 1.3.4 Measurement of Heisenberg spin exchange rate

#### 1.3.4.1 Methods based on $T_{2e}$ measurement

For SDSL methods applied to peptides and proteins with  $T_{1e} < \tau_{\text{C}}$ , Heisenberg exchange (HE) generally leads to equal changes in  $T_{1e}$  and  $T_{2e}$  of the nitroxide, therefore,

$$W_{\text{ex}} = \Delta[1/T_{1e}] = \Delta[1/T_{2e}] = k_{\text{ex}}C_{\text{R}} \quad \text{Equation 1.12}$$

Based on Equation 1.12,  $W_{\text{ex}}$  could be extracted either from measurement of  $T_{1e}$  or  $T_{2e}$ . Spin-spin relaxation time ( $T_{2e}$ ) characterizes relaxation of the transverse component of the magnetization vector, that exponentially decays towards zero, thus, leading to Lorentzian line broadening of CW EPR spectra.  $\Delta T_{2e}$  could be measured from EPR line broadening as described below and related to  $W_{\text{ex}}$  as:

$$\begin{aligned}
W_{\text{ex}} &= \Delta[1/T_{2e}] = \gamma\Delta B_{1/2}/2 \\
&= 0.44 \times 10^7 \text{ (g)}\Delta B_{1/2} && \text{Equation 1.13} \\
&= 0.44 \times 10^7 \text{ (g)}3^{1/2}\Delta\Delta B_{\text{pp}}
\end{aligned}$$

where  $g$  is the electronic  $g$ -factor of the nitroxide,  $\Delta B_{1/2}$  is the Lorentzian line width at half-height of the absorption spectrum. For the first-derivative EPR spectra “peak-to-peak” linewidth,  $\Delta B_{\text{pp}}$  is usually reported.  $\Delta\Delta B_{\text{pp}}$  is an increase in peak-to-peak of the Lorentzian component of the first derivative EPR spectrum due to the presence of the exchange reagent. However, when the spectrum is noisy or the broadening is small compared with inhomogeneous linewidth, it is more accurate to use the spectra simulation to obtain  $\Delta B_{\text{pp}}$  to calculate  $W_{\text{ex}}$ , because the entire lineshape is used to obtain the result. These parameters are related to  $T_{2e}$  as follows,

$$\Delta B_{1/2} = \frac{2}{\gamma} \times \frac{1}{T_{2e}} \quad \text{Equation 1.14}$$

$$\Delta B_{\text{pp}} = \frac{2}{\sqrt{3}\gamma} \times \frac{1}{T_{2e}} \quad \text{Equation 1.15}$$

$$\gamma = -g\mu_B/\hbar \quad \text{Equation 1.16}$$

#### 1.3.4.2 Saturation recovery EPR

A commonly used method to measure HE rate is saturation recovery (SR) EPR which provides a direct means to measure  $T_{1e}$ <sup>31</sup>. In this method, saturating microwave pulses are delivered to the sample effectively flipping the magnetization vector into x-y plane and the recovery of the z-magnetization is monitored in real time.  $T_{1e}$  could be obtained from the

differences between the recovery curves measured in the absence and presence of an exchange reagent.

The amplitude of the SR-EPR signal,  $f$ , measured at the central line of a nitroxide spin label ( $m_l = 0$ ) of a single population in the presence of an exchange reagent is given as:

$$\begin{aligned}
 f = & \mathbf{A}_1 \mathbf{e}^{-(2W_e + 2W_{ex})t} + \mathbf{A}_2 \mathbf{e}^{-(2W_e + 2W_{ex} + 3W_n)t} \\
 & + \mathbf{A}_3 \mathbf{e}^{-(2W_e + 2W_{ex} + 3W_R)t} \qquad \qquad \qquad \mathbf{Equation\ 1.17} \\
 & + \mathbf{A}_4 \mathbf{e}^{-(2W_e + 2W_{ex} + 3W_n + 2W_R)t} + \mathbf{H.O.T}
 \end{aligned}$$

where  $W_e$  is the electron spin-lattice relaxation rate,  $W_n$  is the  $^{14}\text{N}$  nuclear spin-lattice relaxation rate,  $W_{ex}$  is the bimolecular exchange rate of the exchange reagent with nitroxide,  $W_R$  is the rotational diffusion rate of the nitroxide, and H.O.T is higher order terms. The first term of the Equation 1.17 describes the sum of the electronic relaxation rate and exchange rate alone. The relaxation rates are related to the corresponding relaxation times as,

$$2W_e = T_{1e}^{-1} \qquad \qquad \qquad \mathbf{Equation\ 1.18}$$

$$2W_n = T_{1n}^{-1} \qquad \qquad \qquad \mathbf{Equation\ 1.19}$$

$$2W_R = \tau_{1R}^{-1} \qquad \qquad \qquad \mathbf{Equation\ 1.20}$$

where  $\tau_R$  is the rotational correlation time of the nitroxide.

For correlation time in the range of 1- 6 ns,  $W_R$  for protein-bound nitroxide is of the order  $10^8 \text{ s}^{-1}$ , and  $W_n$  is of the order  $10^7 \text{ s}^{-1}$ . Hence, saturation recovery due to rotational diffusion and nuclear relaxation generally completes within the dead time of data collection set by the bandwidth of the spectrometer. As a result,  $W_{ex}$  and  $W_e$ , which are of the order  $10^5 \text{ s}^{-1}$ , are the only recovery processes observed. Thus, a single exponential decay reflecting only the first term in the Equation 1.17 is expected for a single population of nitroxide. More

commonly, the EPR spectrum of the nitroxide in protein or peptide reflects two dynamic states, thereby leading to a double exponential SR curve.

As a result, the first step in the experimental data analysis is to fit single or double exponential curves to each SR curve. From these fits, the first approximations to  $W_{ex}$  and  $W_e$  will be obtained. For the single exponential, the SR curves are described by,

$$f_1 = A_{10} + A_{11}e^{-2W_e t} \quad \text{Equation 1.21}$$

$$f_2 = A_{20} + A_{21}e^{-(2W_e + W_{ex2})t} \quad \text{Equation 1.22}$$

$$f_3 = A_{30} + A_{31}e^{-(2W_e + W_{ex3})t} \quad \text{Equation 1.23}$$

where  $f_1$ ,  $f_2$  and  $f_3$  represent SR curves under inert atmosphere, in equilibrium with air, or in the presence of 3mM NiEDDA under inert atmosphere, respectively.  $W_{ex2}$  and  $W_{ex3}$  are the exchange rates for oxygen and NiEDDA, respectively.  $A_{i0}$  and  $A_{i1}$  have to be fit to a set of experimental curves for a spin-labeled residue. For a biexponential decay, the SR curves are described by the following set of equations:

$$f_1 = A_{10} + A_{11}e^{-2W_{e1}t} + A_{12}e^{-2W_{e2}t} \quad \text{Equation 1.24}$$

$$f_2 = A_{20} + A_{21}e^{-(2W_{e1} + W_{ex21})t} + A_{22}e^{-(2W_{e2} + W_{ex22})t} \quad \text{Equation 1.25}$$

$$f_3 = A_{30} + A_{31}e^{-(2W_{e1} + W_{ex31})t} + A_{32}e^{-(2W_{e2} + W_{ex32})t} \quad \text{Equation 1.26}$$

where the additional subscripts 1 and 2 in the exponentials refer to the two population. The baselines  $A_{i0}$ , and the amplitude  $A_{i1}$  and  $A_{i2}$  have to be fit to a set of experimental curves for spin-labeled residues.

The values of the Heisenberg exchange rates determined by CW power saturation have been shown to agree closely with the corresponding values measured directly by saturation recovery EPR<sup>28</sup>. The higher  $W_{ex}$  indicates the higher accessibility of the labeled

sites to the relaxation reagents, thereby more exposing to the solvent; while sites are buried from the solvent with smallest  $W_{ex}$ . The trends of  $W_{ex}$  have been reported to coincide with the known x-ray crystal structure of proteins<sup>31-32</sup>.

## Chapter 2 Experimental

**2.1 Materials:** 1,2-*di*-(9Z-octadecenoyl)-*sn*-glycero-3-phosphocholine (DOPC), 1,2-dihexadecanoyl-*sn*-glycero-3-phosphocholine (DPPC), 1,2-ditetradecanoyl-*sn*-glycero-3-phosphocholine (DMPC), 1,2-didodecanoyl-*sn*-glycero-3-phosphocholine (DLPC), 1-palmitoyl-2-stearoyl-(12-*doxyl*)-*sn*-glycero-3-phosphocholine (12-*doxyl*-PC) and 1-palmitoyl-2-stearoyl-(16-*doxyl*)-*sn*-glycero-3-phosphocholine (16-*doxyl*-PC) were purchased from Avanti Lipids (Alabaster, AL) and used without further purification. Cesa TMH4 and TMH5 peptides (ca.70% purity) and WALP23 C12 peptide were synthesized through solid phase peptide synthesis by Synbiosci (San Francisco, CA) and RS Synthesis, LLC (Louisville, KY), respectively. One-letter sequences for Cesa TMH4 and 5 peptides and their abbreviated names used throughout the text are given in Table 1. All other chemicals were optioned from Alfa Aesar, Sigma-Aldrich, and Oakwood.

**2.2 Spin labeling of TMH peptides with S-(2,2,5,5-tetramethyl-2,5-dihydro-1H-pyrrol-3-yl)methyl methanesulfonothioate (MTSL) (General procedure):** The crude peptide (one-letter sequences are shown in Table 2.1 and Table 2.2) was dissolved in trifluoroacetic acid (TFA) (1mg/10  $\mu$ L), incubated for at least 10min at room temperature, and TFA was removed by N<sub>2</sub> flow. This treatment makes TMHs completely soluble in trifluoroethanol (TFE).<sup>33</sup> To neutralize the residuals of TFA, the pH of the peptide solution was adjusted to approx. pH = 8.0 with triethylamine (TEA). MTSL in acetonitrile (1.3 equiv) was added, and the reaction mixture was incubated at 37 °C for 24 h. The resulting solution of the spin-labeled peptide was used for peptide reconstitution to the lipid vesicles.

The MTSL-labeled TMH samples were prepared for ESI-MS analysis as follows.

After TFA was removed with N<sub>2</sub> flow, a peptide was freeze-dried in a lyophilizer for 3 more hours to completely remove residual TFA; neutralization with TEA is unwelcome because formation of the salt (as well as the residuals of TFA) seems to interfere with the ionization process. Dried peptide was dissolved in TFE at the concentration of 1.5 mM and 1 molar equiv of MTSL was added. The reaction mixture was incubated at 37 °C for 24 h. The resulting solution was diluted with methanol in 1:1 ratio and syringe-injected to the mass spectrometer at a flow rate of 15–20 µL/min. HR-ESI mass spectra in positive ion mode were measured with Thermo Fisher Scientific Exactive Plus MS Orbitrap mass spectrometer using Heated Electrospray Ionization (HESI).

The SL-labeled TMH samples were prepared for MALDI-TOF/TOF –MS (AB Sciex 5800 system) analysis in a similar way as described above. The peptide in (TFE) solution was spotted onto the MALDI plate along with the matrix ( $\alpha$ -cyano-4-hydroxycinnamic acid in 50% methanol/50% H<sub>2</sub>O 0.1% TFA). The method is reflector positive.

**2.3 Reconstitution of MTSL-labeled TMH peptides into the lipid vesicles** (*General procedure*): A solution of crude MTSL-labeled CesA TMH peptide in TFE was mixed in a conical glass vial with chloroform solution of lipids at 1:100 molar ratio. Solvents were removed by N<sub>2</sub> flow and the residue was incubated in a vacuum desiccator overnight to remove residual organic solvents. Dried lipids containing TMH peptide were rehydrated with 50 mM phosphate buffer at desired pH, through ten consecutive freeze-thaw cycles between liquid nitrogen and a water bath set for 37 °C to prepare ~20% (w/v) multilamellar vesicles (MLV). A lipid suspension was vortexed for 10-15 s between the freeze-thaw cycles. Access of the free spin label was removed as follows. A sample containing MLV was

diluted with 20 volume times of 50 mM phosphate buffer at desired pH, vesicles were spun down by centrifugation, clear supernatant solution was carefully decanted and discarded, 20 volume times of fresh buffer, was added, the sample was vortexed briefly, and subjected to 2-3 freeze-thaw cycles. This procedure was repeated until the EPR spectrum from the supernatant solution showed no spin label signal.

**2.4 Purification and lipid reconstitution of MTSL-labeled WALP23 peptides:** Peptide purification was performed on a Shimadzu SCL-10A HPLC system equipped with two LC10AC pumps and a SPD10AV UV detector. WALP23 peptides (the one-letter sequences are shown in Table 2.3) were spin-labeled with MTSL similar to the published procedure<sup>28</sup> and purified by HPLC on a C4 10 $\mu$  300A 250 $\times$ 10 mm reversed-phase column (Phoenix) at 4 mL/min flow rate using 0.1% TFA in H<sub>2</sub>O (solvent A) and 0.1% TFA in CH<sub>3</sub>CN (solvent B) and gradient conditions 80% B in A to 95% B in over 30 min. All purified spin labeled WALP23 peptides were analyzed by MALDI-TOF/TOF mass spectrometry (AB Sciex 5800 system). The peptide in tetrafluoroethanol (TFE) solution was spotted onto the MALDI plate along with the matrix ( $\alpha$ -cyano-4-hydroxycinnamic acid in 50% methanol/50% H<sub>2</sub>O 0.1% TFA). The method is reflector positive.

A solution of HPLC-purified MTSL-labeled WALP peptide in TFE was mixed in a conical vial with a chloroform solution of lipids at 1:100 molar ratio. The concentration of WALP peptides was calculated based on the absorbance at 280 nm ( $\epsilon = 22400 \text{ M}^{-1}\text{cm}^{-1}$ )<sup>34</sup>. Solvents were removed by N<sub>2</sub> flow and the residue was incubated in a vacuum desiccator overnight to remove residual organic solvents. To prepare ~20% (w/v) multilamellar vesicles (MLV), dried lipids containing WALP peptide were rehydrated with 50 mM phosphate buffer

at desired pH, through ten consecutive freeze-thaw cycles between liquid nitrogen and a water bath set for 37 °C. A lipid suspension was vortexed for 10-15 sec between the freeze-thaw cycles.

### **2.5 Sucrose differential centrifugation of TMH peptides embedded in lipid bilayers:**

DOPC vesicles containing reconstituted TMH peptide were suspended in 3% (w/v) solution of sucrose in 50 mM phosphate buffer, at desired pH. The sample was centrifuged for 30 min (7 °C, 18000 g). The separate bands were carefully collected and washed with 50 mM phosphate buffer (5 × sample volume mL) to remove excess sucrose.

### **2.5 Reconstitution of native Cesa TMHs to DOPC vesicles doped with 1 mol% of n-**

**doxyl-PC lipid:** Chloroform solutions of spin-labeled 12-*doxyl*-PC or 16-*doxyl*-PC lipids and DOPC were mixed at 1:100 molar ratio in a conic vial, and the native Cesa TMH5 from (1.5 mM) stock solution in TFE containing trace amount of TFA was added to reach a final peptide to lipid ratio of 1:25. The mixture was dried and re-hydrated as described above.

### **2.6 Preparation of nickel(II)-EDDA complex (NiEDDA):**

Synthesis of NiEDDA was followed as published<sup>32</sup>. Ni(OH)<sub>2</sub> (464mg) and EDDA (881mg) (molar ratio 1:1) were mixed in 100 mL methanol/water (1:1 v/v). The mixture was stirred for 24 hours at room temperature and an additional 24 hours at 60 °C. Any undissolved material was filtered out, clear solution was collected and water was removed under vacuum.

**Table 2.1 One-letter sequence and mass spectroscopy data for spin labeled CesATMH4 peptides**

Peptide name/label position	Peptide name/label position	Calculated isotropic MW	Observed isotropic MW
TMH4 C2	SC(MTSL)NLASVLFLGLFLSIIVTAVLEL	2718.52290	2742.53089, <sup>a</sup> [M+Na] <sup>+</sup>
TMH4 L3C	SNC(MTSL)ASVLFLGLFLSIIVTAVLEL	2605.43884	1315.22080, <sup>a</sup> [M+H+Na] <sup>2+</sup>
TMH4 L7C	SNLASVC(MTSL)FLGLFLSIIVTAVLEL	2605.43884	1314.71685, <sup>a</sup> [M+H+Na] <sup>2+</sup>
TMH4 L11C	SNLASVLFLGC(MTSL)FLSIIVTAVLEL	2605.43884	1315.22283, <sup>a</sup> [M+H+Na] <sup>2+</sup>
TMH4C I15C	SNLASVLFLGLFLSC(MTSL)IVTAVLEL	2605.43884	1315.22082, <sup>a</sup> [M+H+Na] <sup>2+</sup>
TMH4 C23	SNLASVLFLGLFLSIIVTAVLEL(MTSL)L	2605.43884	1371.75735, <sup>a</sup> [M+H+Na] <sup>2+</sup>
Native TMH4	SNLASVLFLGLFLSIIVTAVLEL	2431.43411	2454, <sup>b</sup> [M+Na] <sup>+</sup>

a. Accurate mass acquired by ESI-MS. b. Mass result obtained by MALDI-TOF/TOF spectrometry.

**Table 2.2. One-letter sequence and mass spectroscopy data for spin labeled Cesa TMH5 peptides**

Peptide name/label position	Sequence	Calculated isotropic MW	Observed isotropic MW
TMH5 C2	EC(MTSL)QFWVIGGVSAHLFAVFQGFLLKM	2897.43444	1450.22568, [M+2H] <sup>2+</sup>
TMH5 V9C	EQFWVIGGC(MTSL)SAHLFAVFQGFLLKML	2911.45009	1457.24259, [M+2H] <sup>2+</sup>
TMH5 L13C	EQFWVIGGVSAHC(MTSL)FAVFQGFLLKML	2897.43444	1450.22912, [M+2H] <sup>2+</sup>
TMH5 V16C	EQFWVIGGVSAHLFAC(MTSL)FQGFLLKML	2911.45009	1457.24151, [M+2H] <sup>2+</sup>
TMH5 F20C	ECQFWVIGGVSAHLFAVFQGC(MTSL)LKML	2863.45009	1433.236951, [M+2H] <sup>2+</sup>
TMH5 C23	EQFWVIGGVSAHLFAVFQGFLLKC(MTSL)M	2897.43444	1450.22600, [M+2H] <sup>2+</sup>
Native TMH5	EQFWVIGGVSAHLFAVFQGFLLKML	2723.42971	1362.72742, [M+2H] <sup>2+</sup>

**Table 2.3. One-letter sequence and mass spectrometry data for spin-labeled WALP23 peptides**

Peptide name/label position	Sequence	Calculated MW	Observed MW
WALP23 C1	Ac-C(MTSL)WWLALALALALALALALALWWA-NH <sub>2</sub>	2752	2775, [M+Na] <sup>+</sup>
WALP23 C2	Ac-GC(MTSL)WLALALALALALALALALWWA-NH <sub>2</sub>	2622	2645, [M+Na] <sup>+</sup>
WALP23 C4	Ac-GWWC(MTSL)ALALALALALALALALWWA-NH <sub>2</sub>	2695	2718, [M+Na] <sup>+</sup>
WALP23 C6	Ac-GWWLAC(MTSL)ALALALALALALALWWA-NH <sub>2</sub>	2695	2718, [M+Na] <sup>+</sup>
WALP23 C8	Ac-GWWLALAC(MTSL)ALALALALALALWWA-NH <sub>2</sub>	2695	2718, [M+Na] <sup>+</sup>
WALP23 C10	Ac-GWWLALALAC(MTSL)ALALALALALWWA-NH <sub>2</sub>	2695	2718, [M+Na] <sup>+</sup>
WALP23 C12	Ac-GWWLALALALAC(MTSL)ALALALALWWA-NH <sub>2</sub>	2695	2718, [M+Na] <sup>+</sup>
WALP23 C14	Ac-GWWLALALALALAC(MTSL)ALALALWWA-NH <sub>2</sub>	2695	2718, [M+Na] <sup>+</sup>
WALP23 C16	Ac-GWWLALALALALALAC(MTSL)ALALWWA-NH <sub>2</sub>	2695	2718, [M+Na] <sup>+</sup>
WALP23 C18	Ac-GWWLALALALALALALAC(MTSL)ALWWA-NH <sub>2</sub>	2695	2718, [M+Na] <sup>+</sup>
WALP23 C20	Ac-GWWLALALALALALALALAC(MTSL)WWA-NH <sub>2</sub>	2695	2718, [M+Na] <sup>+</sup>
WALP23 C23	Ac-GWWLALALALALALALALALWWC(MTSL)-NH <sub>2</sub>	2737	2760, [M+Na] <sup>+</sup>
WALP23 L8S	Ac-GWWLALASALALALALALALWWA-NH <sub>2</sub>	2493	2516, [M+Na] <sup>+</sup>

**2.7 Circular Dichroism Spectroscopy of MTSL labeled CesA TMH peptides:** CD spectra were acquired with a Jasco J-815 spectropolarimeter.

a) TFE peptide solutions were prepared at concentration of 0.5mM. No other special preparations were used.

b) DOPC MLV with TMH peptide reconstituted at the peptide to lipids ratio = 1:50 or 1:100 were diluted to the total peptide concentration at about 0.1-0.2 mM and extruded through a polycarbonate membrane with 100 nm pores size (Whatman, LLC) using a syringe extruder (Avanti Polar lipids, Inc) through 11 consecutive passes. The resulted transparent solutions were used to measure room temperature CD spectra in a 0.1 mm path cell. Typical spectrometer settings were: scan range: 195-259 nm; data pitch, 1.0 nm; scanning speed, 50 nm/min; continuous scanning mode.

**2.8 Attenuated total reflectance (ATR) FT-IR spectroscopy:** ATR FT-IR spectra were recorded on a Bruker Vertex 80V infrared spectrometer equipped with a Platinum™ diamond ATR attachment. The lipid vesicles (1.5–2  $\mu$ L) were spread over the diamond surface and excess water was removed under nitrogen flow. Spectra were recorded at room temperature with a resolution of 4  $\text{cm}^{-1}$ .

**2.9 X-band (9.5 GHz) CW EPR spectroscopy:** CW X-band EPR spectra were collected using a Varian Century Series EPR spectrometer (Palo Alto, California, USA) or Bruker Biospin (Billerica, MA) E500 spectrometer from aqueous samples placed into polytetrafluoroethylene tubes. The rigid-limit spectra (77 K) were collected using a finger Dewar (Wilmad). Typical spectrometer settings were: microwave power, 2 mW (20 dB attenuation); field modulation frequency, 100 KHz; modulation amplitude, 1 G or less. For

77 K measurements the microwave power was reduced to  $6.3246 \times 10^{-3}$  mW (45 dB), and the modulation amplitude was 2 G. The spectra were digitized to 2048 data points. The temperature-controlled measurements were carried out using a variable temperature accessory previously described by A. M. Alaouie and A. I. Smirnov.<sup>35</sup>

**2.10 Pulsed saturation recovery (pSR):** Saturation-recovery measurements employed a Bruker Biospin E580 X-band pulse/CW spectrometer with a dielectric split ring resonator. The operating frequency was approximately 9.5 GHz (X-band). A typical pSR experiment used a 300-4000 ns pulse with 20 dbm of microwave power. The dead time was 120 ns, and the microwave power during the observer period was 10 dbm. Each spectrum was an average of 10 scans. 1024 point spectra were obtained for each of experimental conditions. All pSR measurements were acquired with the pump and observed microwave frequencies corresponding to the central  $^{14}\text{N}$  manifold of the nitroxide where the EPR signal is at its maximum.

**2.11 EPR spectral line width broadening induced by molecular oxygen as measured by CW X-band EPR spectroscopy:** The EPR spectral line width broadening was measured as a function of oxygen pressure. The lipid sample was drawn into a gas permeable PTFE tube, folded twice, inserted into a quartz capillary (ID 2mm), and placed into a quick pressure valve (QPV) 5 mm OD EPR tube (Wilmad LabGlass). First, the sample was equilibrated with  $\text{N}_2$  under normal pressure, then with  $\text{O}_2$  under normal pressure as well, and then the  $\text{O}_2$  pressure was gradually increased in 20 psi increments until it reached 100 psi. The sample was equilibrated for 10 min at each pressure value. A method that allows one to accurately measure the relative oxygen-induced line broadening (or relative  $\Delta(1/T_2)$ ) extracted by a

computer simulations from CW EPR spectra acquired at varied oxygen pressure was described by Smirnov et al.<sup>36</sup> For EPR spectra of nitroxides over broad range of motional narrowing (i.e., from fast to intermediate and then slow motion) the oxygen broadening is homogeneous within tumbling nitroxides, within experimental accuracy and can be described as;

$$F(B) = \int_{-\infty}^{+\infty} F_0(B')m(B - B')dB' \quad \text{Equation 2.1}$$

where  $F_0(B)$  serves as a fixed envelope function and represents the spectrum taken in the absence of oxygen.  $F(B)$  is the spectrum acquired in the presence of oxygen.  $m(B)$  is a homogeneous (Lorentzian) line broadening. The only adjustable line width parameter in this fitting model is homogeneous line broadening  $\Delta\Delta B_{p-p}^L$  introduced by the presence of molecular oxygen. Other additional contributions to the line shape such as rotational motion, unresolved proton hyperfine structure and satellite lines are automatically accounted for in the function  $F_0(B)$ . If solubility of oxygen in solution and lipid bilayers follows the Henry's law,  $\Delta\Delta B_{p-p}^L$  linearly depends on the partial pressure of oxygen and, calculating the slope of  $\Delta\Delta B_{p-p}^L$  vs. various oxygen concentrations for different labeled positions along the peptide backbone, the peptide membrane arrangement could be determined.

**2.12 Modeling the membrane hydrophobicity profile:** The relationship between the  $\alpha$ -helical peptide residue number and the distance from the center of the bilayer was calculated according to Nielsen *et al*<sup>28</sup> who carried out systematic EPR accessibility studies for WALP in lipid bilayers. Assuming an idealized  $\alpha$ -helix consisting of 23 amino acid residues the helix rise per turn is 1.537 Å. The center of the helix is taken to be at residue 12 since the

tryptophans at residues 2 and 22 anchored the peptide. Then the linear position  $x$  (in nm) of the residue along the symmetry axis of the  $\alpha$ -helix is related to the residue number,  $n$ , as:

$$x = 1.537(n - 12) \quad \text{Equation 2.2}$$

The hydrophobicity profile of a membrane was modeled by a continuous, symmetric, smooth sigmoidal Boltzmann function according to Marsh *et al* <sup>37-38</sup>

$$Y = (Y_1 - Y_2) \left( \frac{1}{1 + \exp\left(\frac{n - n_0 - d}{\lambda}\right)} - \frac{1}{1 + \exp\left(\frac{n + n_0 - d}{\lambda}\right)} \right) + Y_2 \quad \text{Equation 2.3}$$

where  $Y_1$ ,  $Y_2$  are the limiting values of  $^{14}\text{N}$  hyperfine coupling constants or electronic relaxation rate measured in the experiment. In this work,  $Y_1$  and  $Y_2$  are relaxation rates that are directly proportional to homogeneous linewidth extracted from simulations according to Equation 1.14 and Equation 1.15.  $Y_1$  is the value at the polar headgroup region and  $Y_2$  is the value at the terminal methyl group of the lipid chain.  $n$  is the spin label position and  $n_0$  is the value of the  $n$  at the point of maximum gradient, which is given by  $Y_{n_0} = \frac{1}{2} (Y_1 + Y_2)$ .  $\lambda$  characterizes the width of the transition region.  $d$  is the thickness of one lipid leaflet of the membrane. This function is discussed in detail in Ref 38. The units of  $n_0$ ,  $d$ , and  $\lambda$  are all residue numbers and can be calculated in the unit of nm using Equation 2.2.

## Chapter 3 Membrane insertion, orientation, and inter-helical oligomerization

### 3.1 Introduction

Cellulose, the most abundant of all naturally occurring biopolymers and the major structural component of plant cell walls, consists of linear chains of D-glucose monomers connected through of  $\beta$ -(1,4)-glycosidic linkage. In higher plants, cellulose is synthesized by cellulose synthase - a plasma membrane-bound multimeric complex of CesA proteins that catalyzes the elongation of the polymer chain using uridine diphosphate glucose (UDP-glucose) as a substrate.<sup>18, 39</sup> While no crystal structure of the plant cellulose synthase or its individual components is known to these authors, recently, x-ray structure of the bacterial cellulose synthase from *Rhodobacter sphaeroides* (complex BcsA-BcsB), containing an entrapped UDP-glucose molecule and a translocating glucan chain, has been solved.<sup>19</sup> The structure of the membrane-integrated catalytic BcsA subunit shows that the transmembrane domain, consisting of eight transmembrane helices (TMHs) is not only anchoring the protein to the plasma membrane, but is also involved in translocation of the formed polysaccharide chain. A 3D structure of the cytosolic domain of one of the plant cellulose synthase (GhCesA1 from cotton, *Gossypium hirsutum*) was recently predicted *in silico* using a molecular modeling approach.<sup>23</sup> However, experimental data on the spatial arrangement of the  $\alpha$ -helices in the transmembrane domain of GhCesA1 is still missing.<sup>21</sup> Obtaining the latter data has proven to be an uneasy task because of difficulties of high-yield expression and then crystallization of CesA. This is a common problem for structural biology of membrane proteins containing both transmembrane and bulky intra-/extracellular domains

such as CesA.<sup>40</sup> While the number of solved crystal structures of membrane proteins from x-ray of high quality 3D crystals is rapidly growing, still, only ~2% of all the structures deposited in the PDB are those of membrane proteins (According to the inquiry of PDB and accessed on July 25, 2014).

Nowadays the arsenal of biophysical methods for structural studies of membrane protein is not limited to x-ray crystallography.<sup>12</sup> Recently, a substantial progress has been made in both computational<sup>41-45</sup> and experimental methods, such as multidimensional solution and solid-state NMR spectroscopy.<sup>46-47</sup> Membrane proteins having a natural tendency of forming 2D arrays<sup>48</sup> could be studied using cryo-electron microscopy (cryo-EM)<sup>49</sup> and atomic force microscopy (AFM) albeit at lower spatial resolution.<sup>50</sup> The latter two methods as well as solid-state NMR have the advantage of yielding the protein structure in a more native-like lipid bilayer environment – the condition typically missing in the crystals used for x-ray analysis. Sparse distance constrains of *ca.* 4-10 nm range for domain arrangements of membrane proteins could also be obtained from Förster resonance energy transfer (FRET) experiments<sup>51-53</sup>. The method is based on the analysis of dipole-dipole energy transfer<sup>54</sup> between a donor and an acceptor fluorophores tethered to specific protein residues. One can also take advantage of the intrinsically fluorescent natural amino acids such as Trp and Tyr instead of chemical modification of proteins with artificial fluorescent tags.<sup>55-56</sup>

Electron paramagnetic resonance (EPR) spectroscopy in combination with site-directed spin-labeling (SDSL) is yet another molecular probe-based spectroscopic technique that has also been proven to be informative for probing structure and dynamics protein

systems in a site-specific manner. SDSL EPR is especially useful for structure-function studies of membrane proteins that are difficult to study otherwise<sup>57-58</sup>. The method is based on the analysis of EPR spectra from a paramagnetic tag covalently attached to a specific site of a peptide or a protein, typically, to SH-group of cysteine that is introduced either during the solid phase peptide synthesis (SPPS) or through the site-directed mutagenesis.<sup>15, 28-29, 31</sup> Such unnatural side chains have molecular volume similar to that of phenylalanine and, typically, cause little or no perturbation to the protein structure.<sup>16</sup> SDSL EPR-based methods require only a few mg of spin-labeled protein, are not limited by the protein size, and do not require protein crystallization. Another principal advantage of SDSL EPR is in providing unique structural information on membrane-associated proteins and/or peptides under native-like lipid bilayer conditions at low (< 1-2 mol%) protein-to-lipid ratio even for the structures that interconvert on millisecond time scale.<sup>32, 59</sup>

Here we describe the application of SDSL-EPR methods to elucidate the elements of the transmembrane structure of the plant cellulose synthase. In absence of reliable protocols for protein expression that would yield CesA on a mg scale, we had to constrain ourselves to a set of transmembrane  $\alpha$ -helices (TMHs) that were chemically synthesized through SPPS. Homology modeling and structure predictions identified CesA TMH4 and TMH5 (residues 781-803 and 817-840, respectively) as the likely transmembrane helices to interact in the lipid bilayer<sup>20</sup>. Such helix-to-helix interactions could play essential role in folding and membrane assembly of CesA. Specifically, we aimed at investigating two questions: (i) whether the cytoplasmic loop connecting TMHs 4 and 5 (Figure 1.4) plays a role in the TMHs insertion and transmembrane assembly and dictates the relative orientation of these

TMHs and (ii) whether the individual TMH4 and TMH5 inter-helically cross-oligomerize in the membrane. To answer these questions, the cytoplasmic loop was truncated and the library consisting of only 23-mer TMH4 and 24-mer TMH5 model peptides was synthesized. For site-specific labeling of these TMHs with methanethiosulfonate spin label methanethiosulfonic acid S-(1-oxyl-2,2,5,5-tetramethyl-2,5-dihydro-1*H*-pyrrol-3-ylmethyl) ester (MTSL, spin label III in Figure 1.1), the selected amino acids in the hydrophobic patches of the peptides were single point-mutated to Cys.

Analysis of the predicted structure of CesA and the crystal structure of BcsA revealed a good protein sequences alignment between TMH5 in CesA and the interfacial helix 3 (IF3) in BcsA<sup>20</sup>. Thus, this TMH is expected to insert in lipid bilayers in similar ways and we have aimed to investigate the membrane structure of TMH5 experimentally. Although the individual  $\alpha$ -helical peptides may not behave as when being a part of the native transmembrane domain, this simplified model would expect to shed some light on the role of helix-helix interactions in the CesA membrane assembly.

Thus, in this report we describe experimental protocols for spin-labeling and a phospholipid bilayer insertion of hydrophobic TMH4 and 5 from the transmembrane domain of GhCesA1 from cotton, *Gossypium hirsutum*. Effects of the lipid composition and the bilayer hydrophobic match on the TMHs' insertion into multilamellar vesicles (MLVs) have been studied. Molecular accessibility and diamagnetic dilution X-band (9.5 GHz) EPR experiments were employed to determine the arrangement of the THMs within the lipid membrane and their relative orientation. To the best of authors' knowledge, this is the first report of employing spin-labeling EPR for studying structural arrangements of  $\alpha$ -helices

from the transmembrane domain of the plant cellulose synthase.

## **3.2 Results and discussions**

### **3.2.1 The choice and characterization of spin-labeled CesA TMH peptides**

According to the two-stage model of membrane protein folding and oligomerization proposed by Popot and Engelman<sup>2</sup> the individual CesA transmembrane helices should (a) insert into lipid bilayer and (b) oligomerize even without the connecting loops being present even though the full correct assembly and function of the protein may require the presence of at least some of the loops.<sup>2</sup> In order to test the validity of this hypothesis for CesA, two transmembrane helices TMH4 and TMH5 identified by computational modeling<sup>23</sup> and hydrophobicity considerations<sup>60</sup> have been chosen. These TMHs were expected to interact according to the predicted CesA structure<sup>20, 23, 39</sup>.

In order to simplify solid state peptide synthesis and increase its yield, it was chosen to synthesize 23-mer TMH4 and 24-mer TMH5 model peptides without the connecting cytoplasmic loop (Table 2.1 and Table 2.2). The model peptides were chosen to contain 1-2 native amino acid residues from the loop regions to flank the intrinsically hydrophobic core. It was expected that these flanking residues would improve the solubility of the hydrophobic TMHs in more polar solvents and to promote peptides' transmembrane insertion. Site-directed EPR studies were enabled by synthesizing a library of TMH4 and TMH5 variants with the selected amino acids in the hydrophobic core of the peptide that were single point mutated to cysteine (Table 2.1 and Table 2.2). Consequently, the cysteine thiol group was

covalently modified by a reaction with methanethiosulfonate spin label methanethiosulfonic acid S-(1-oxyl-2,2,5,5-tetramethyl-2,5-dihydro-1H-pyrrol-3-ylmethyl) ester (MTSL). Spin-labeling of the terminal positions of TMHs was accomplished by inserting a Cys just before the last residue at each terminus rather than mutating the native residue.

All the synthesized TMHs revealed a very strong tendency to oligomerize in a number of common peptide solvents. Specifically, it was found either native or mutated TMH4 and TMH5 peptides, after being HPLC-purified and lyophilized, became insoluble in such common organic solvents used for spin-labeling as methanol, chloroform, TFE, DMF, and DMSO. We have also failed to solubilize the peptides in solutions of common membrane peptide/protein detergents including OG, DDM, and SDS.

The literature data suggested that in many instances the peptide agglomerates could be disaggregated by using trifluoroacetic acid (TFA) as a solvent/co-solvent.<sup>33, 61-62</sup> While the role of TFA in solubilizing of peptide aggregates is not yet fully understood, it was suggested that this non-nucleophilic strong acid is capable of effectively disrupting both hydrophobic and hydrogen bonding interactions.<sup>63-64</sup> Indeed, a treatment of Cesa TMHs with TFA (see the Experimental Part in Chapter 2) followed by TFA removal made these peptides soluble in TFE. Unfortunately, the residual TFA left in the peptide solution causes the nitroxide (MTSL) disproportionation<sup>65</sup> to the EPR-silent hydroxylamine and oxoammonium salt and this drastically reduced the yield of the spin-labeled peptide. Because of this disproportionation we have initially observed no detectable EPR signal after incorporating TFA treatment into the experimental protocol (Figure 3.1(A)). This problem was solved by neutralization of the solution with triethylamine (TEA) that restored the EPR

signal after *ca.* 24 hr (Figure 3.1(B)). Thus, the spin-labeling protocol has been modified to include a neutralization of a peptide TFE solution with TEA prior to the labeling reaction with MTSL. Elemental compositions of the spin-labeled (SL-) TMHs were confirmed by ESI-MS or MALDI-MS analysis.

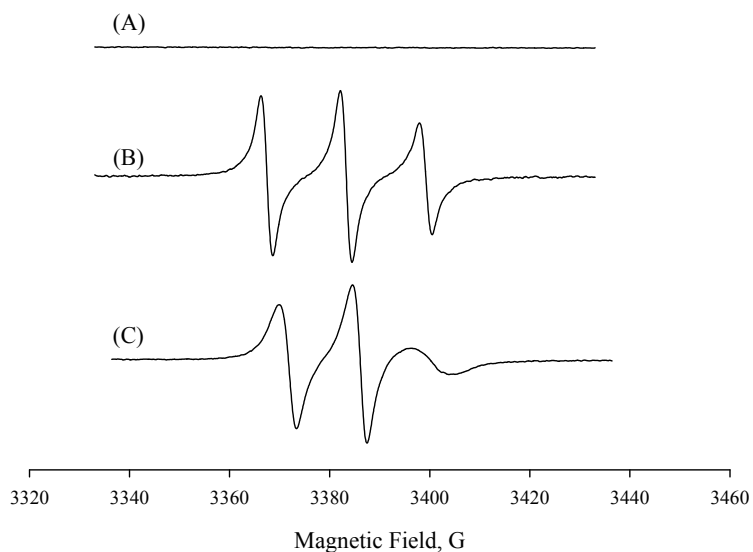


**Figure 3.1** Room temperature X-band (9.5 GHz) EPR spectra of: (A) TFE solution of SL-TMH5 L13C containing residuals of TFA revealed no detectable nitroxide signals; (B) from the same solution after 24 hrs. neutralization with TEA; (C) Non-aggregating WALP23 C12 with MTSL and incorporated into DOPC multilamellar vesicles (MLVs) at pH = 7.0.

Secondary structure of the spin-labeled peptides was examined by far-UV circular dichroism spectroscopy (CD) in TFE solution and small unilamellar DOPC vesicles. Figure 3.2 (A) shows CD spectra of unlabeled and spin labeled L7C variant of the TMH4 peptides

and V9C variant of the TMH5 measured in TFE solution. Typically,  $\alpha$ -helical peptides exhibit two negative absorptions at approximately 208 nm ( $\pi$ - $\pi^*$  transition) and 222 nm ( $n$ - $\pi^*$  transition) with ratio of molar ellipticities  $R = \theta_{222}/\theta_{208}$  of about  $R \approx 0.9$  and accompanied by a positive band at approximately 192 nm (not shown in Figure 3.2)<sup>66</sup>. In the helix-inducing solvent TFE<sup>67</sup> both the unlabeled and the SL-TMH5 V9C and TMH4 L7C peptides show a rather close  $\theta_{222}/\theta_{208}$  of  $\approx 0.9$  and  $\approx 0.75$ , respectively, confirming peptide's  $\alpha$ -helical character. The CD traces of the labeled and unlabeled peptides practically overlap, thus demonstrating that spin labeling renders no significant perturbation to the  $\alpha$ -helical structure. Room-temperature EPR spectra of TFE solutions of SL-TMH5 peptides were all similar to that of WALP23 C12 shown in Figure 3.1. As expected, these spectra consist of three nitrogen hyperfine lines with unequal peak-to-peak amplitude due to incomplete averaging of anisotropic magnetic interactions by these freely tumbling  $\alpha$ -helical peptides.

The CD spectra of MTSL-labeled TMH5 (SL-TMH5) V9C and TMH4 L7C in DOPC lipid bilayers are shown in Figure 3.2 (B). In the CD spectra, the  $n$ - $\pi^*$  transition ( $\sim 220$  nm band) is responsive for the  $\alpha$ -helical content, and  $\pi$ - $\pi^*$  transition ( $\sim 208$  nm band) that involves a charge transfer from the nitrogen atom of amide group to the oxygen atom is sensitive to distortion of geometry of the amide group caused, for example, by peptide aggregation<sup>68</sup> or coiled-coil structure formation.<sup>69</sup> Since the intensities of these transitions depend on the angle between the transition dipoles of the amide group, the  $\theta_{222}/\theta_{208}$  ratio is a good indicator of the conformational stress the individual  $\alpha$ -helices are subjected to. For the TMH5 V9C peptide in DOPC the  $\alpha$ -helical content significantly decreased (to 11.6%), which could be attributed to oligomerization of the peptide. On the contrary, the TMH4 L7C shows

a rather high  $\alpha$ -helical content of 96.4%. Note that  $\theta_{222}/\theta_{208}=1.2$  calculated from CD spectra of SL-TMH4 L7C in DOPC vesicles might indicate a significant contribution of coiled-coil structures.<sup>68</sup>

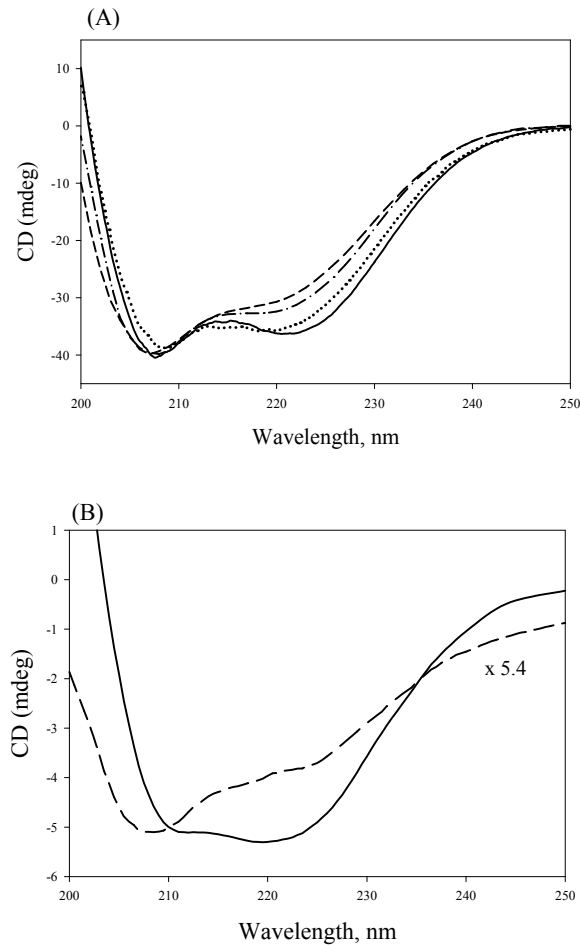


**Figure 3.2** Circular dichroism spectra: (A) TMH5 V9C (solid line), SL-TMH5 V9C peptides (dotted line), TMH4 L7C (dash-dotted line), SL- TMH4 L7C (dashed line) in TFE solution; (B) CD spectra of SL-TMH5 V9C peptide (dashed line) and SL- TMH4 L7C (solid line) in 100 nm unilamellar DOPC vesicles.

### 3.2.2 Effect of hydrophobic mismatch and bilayer lipid composition

Plasma membranes of plant cells have complex compositions including PE, PC, PI, PA lipids and sphingolipids and sterols<sup>70</sup> The length of the lipid acyl chains is also varied from 16 to 24 units. Thus, one may hypothesize that some specific lipids may be required for proper insertion and folding of CesA TMHs. The hydrophobic thickness of the lipid bilayer should also match the length of the folded hydrophobic transmembrane segment of a membrane protein or a peptide; otherwise, a hydrophobic mismatch effect would take place. Typically, when the hydrophobic segment of the protein is longer than the hydrophobic bilayer thickness, the protein could experience an inter-helical oligomerization (*i.e.*, aggregation), a change in the membrane tilt angle, or a conformation that would shorten its backbone to reduce the hydrophobic area exposed to an aqueous phase. If the hydrophobic part is shorter compared to the hydrophobic thickness of the bilayer, the  $\alpha$ -helix could be stretched by hydrophobic forces or the protein could aggregate to minimize the mismatch effect. Alternatively, the lipid acyl chains may undergo conformational changes to match the hydrophobic part of a peptide.<sup>71</sup> An even shorter hydrophobic peptide could partition into the lipid bilayer interface instead of being inserted in a transmembrane manner.

As the first step towards determination of an optimal lipid composition for membrane insertion of the CesA TMHs, one of the transmembrane helices, SL-TMH5 L13C, was studied upon insertion into multilamellar vesicles composed of a series of lipids with different length and chemical structure of the acyl chains. Since zwitterionic phosphatidylcholine (PC) and phosphatidylethanolamine (PE) lipids are the major constituents of the cotton plasma membrane,<sup>72</sup> saturated 1,2-dilauroyl-*sn*-glycero-3-

phosphocholine (DLPC, 12:0/12:0 PC), 1,2-dimyristoyl-*sn*-glycero-3-phosphocholine (DMPC, 14:0/14:0 PC), 1,2-dipalmitoyl-*sn*-glycero-3-phosphocholine (DPPC, 16:0/16:0 PC), and unsaturated 1,2-dioleoyl-*sn*-glycero-3-phosphocholine (DOPC, 18:1(9Z)/18:1(9Z) PC) PC phospholipids were chosen as the primary components for model bilayers.

Sensitivity of X-band (9 GHz) EPR spectra to rotational dynamics of nitroxides especially at rotational correlation times  $\tau_c = 1-3$  ns that correspond to a transition from fast to intermediate motion EPR regime is well documented in the literature.<sup>16,73</sup> For example, Figure 3.1(C) shows a spectrum of a SL-WALP23 C12 peptide that is known to insert as a non-aggregating helix into DOPC bilayer.<sup>28,74</sup> Rotational motion of the WALP peptide in the lipid environment is slower than for a similarly-sized  $\alpha$ -helical TMH5 L13C in less viscous TFE. This slower motion is still fast on the X-band EPR time scale as it yields three well-resolved nitrogen hyperfine components but with visible differences in the peak-to-peak amplitudes (compare Figure 3.1(B) and (C)). Further restrictions in the rotational mobility of spin-labeled nitroxide side chains give rise to significant spectral changes, including unequal splitting between the nitrogen hyperfine coupling components, asymmetric lineshapes, appearance of additional spectral features, and the overall spectral broadening.<sup>16, 29</sup> Typically, the presence of broad components in EPR spectra of spin-labeled peptides/proteins is indicative of aggregated species that exhibit slower rotational diffusion in lipid bilayers *vs.* the unaggregated ones.<sup>75-76</sup> Magnetic spin-spin magnetic interactions (spin exchange and/or dipole-dipole) between adjacent nitroxides with the interspin distances up to 15 Å in the aggregate may also contribute to the spectral broadening.<sup>16</sup> As an example, Figure 3.3 (A) shows an experimental EPR spectrum of MTSL-labeled TMH5 L13C incorporated into

DOPC MLVs at pH = 7.0. The spectrum contains additional broad features that were further revealed by least-squares computer simulations designed to separate sharp and broad components as described by Smirnov.<sup>77</sup> The spectrum in sharp component extracted by such a filtered fitting procedure is very similar to that of unaggregating WALP peptide in DOPC MLVs under the same conditions. The broad component which obtained by spectral subtraction of sharp component from experiment spectrum is typical for aggregated peptides and accounts for  $\approx 94\%$  of all the spin-labeled peptides in the sample based on calculated values of double-integrated EPR intensities.

Thus, the presence of the lowest amount of broadened component in the EPR spectrum of SL-TMH was chosen as a criterion of selection of a proper lipid composition for TMH reconstitution. EPR measurements were carried out at temperatures above the main phase transition temperatures,  $T_m$ , of the corresponding lipids. As we have found, all the tested lipid compositions showed the contribution of the broadened spectral component (spectra is not shown). However, DMPC lipid in the fluid phase<sup>78</sup> showed the highest content of the broadened component as about  $\approx 99.6\%$  (Figure 3.3 (C)). The aggregated peptides contents in DPPC membrane was estimated to be about 96% at 48 °C (fluid phase,  $T_m = 41$  °C) (Figure 3.3 (D)). Interestingly, DLPC lipids showed lower aggregated peptide contents and calculated to be *ca.* 95% (Figure 3.3 (B)) compared to other two longer saturated lipids, DPPC and DMPC. Thus, DOPC lipid was chosen as a model environment for the reconstitution of the Cesa TMH peptides and EPR study of their membrane arrangement.

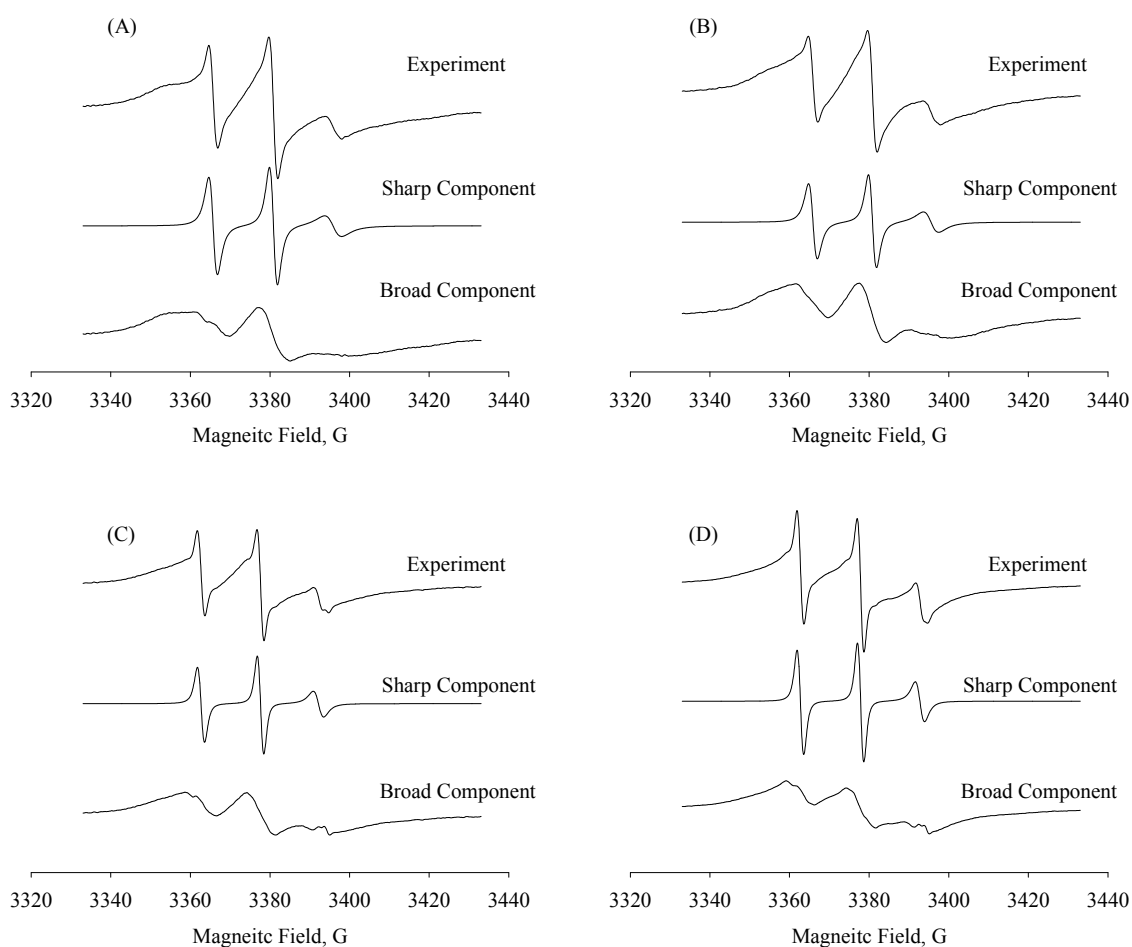


**Figure 3.3** Decomposition of X-band (9.5 GHz) EPR spectra acquired from MTSL-labeled TMH5 L13C in the fluid phase bilayers of different lipid composition: (A) DOPC (room temperature); (B) DLPC (room temperature); (C) DMPC (34 °C); (D) DPPC (48 °C).

Spin-labeled variants of the TMH4 and 5 peptide other than L13C (Table 2.1 and Table 2.2) were also reconstituted to the DOPC vesicles and studied by X-band EPR spectroscopy (Figure 3.4 (A) for TMH4 peptide and Figure 3.4 (B) for TMH5 peptide). It is

clearly seen that all the variants contain the aggregated peptide; however, the content of the aggregated fraction varies with the position of labeling. In general, the fraction of aggregated peptide<sup>16</sup> (the broad component at low field) for TMH4 in DOPC membrane is less compared to that for TMH5 peptide in the same lipid bilayer.

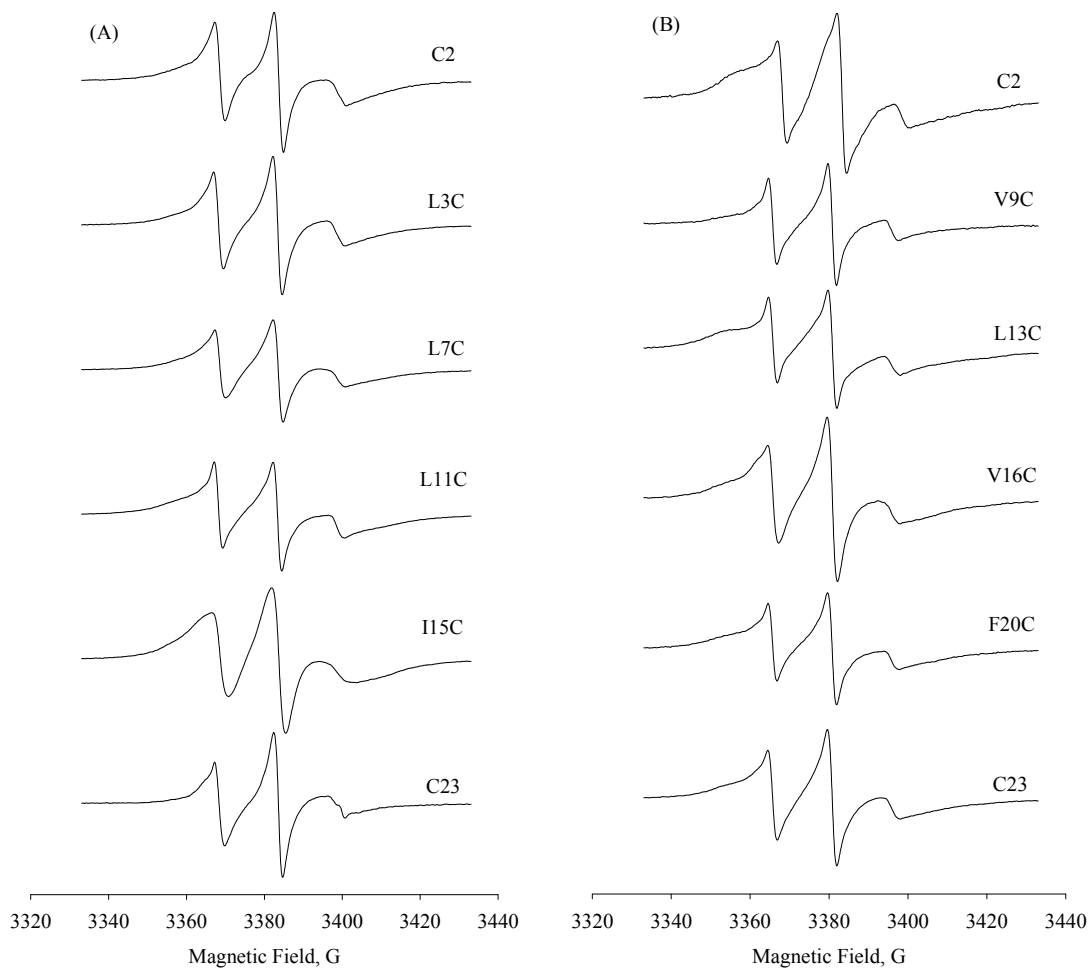


**Figure 3.4** Room temperature X-band (9.5 GHz) EPR spectra acquired from series of SL-TMH4 (A) and SL-TMH5 (B) variants reconstituted to the DOPC bilayer. Labeling sites are shown next to the corresponding spectrum.

Interestingly, the spin label tethered to the N- terminus of SL-TMH5 C2 peptide is experiencing the most restricting environment.<sup>16</sup> We speculate that the most likely reason for this is that in TMH5 C2 the spin-labeled site is flanked by the two polar amino acid residues – glutamic acid (Glu) and glutamine (Gln) (Table 2.2). Indeed, it is well-documented that the hydrogen-bonding amino acid residues,<sup>79</sup> especially Gln,<sup>62, 80</sup> cause strong inter-helical aggregation of peptides. On the other hand, the terminal Glu residue is likely to reside near the PC polar head group region and could electrostatically interact with the positively charged phosphocholine group. A combination of these two factors seems to be the reason for a significantly restricted motion of the nitroxide side chain in SL-TMH5 C2.

The lipid preparations containing reconstituted SL-TMH5 peptides were further separated using sucrose differential centrifugation protocol. Figure 3.5 (A) shows a digital photograph of the two well-distinguished bands acquired after centrifugation of the bilayer-embedded SL-TMH5 L13C in 3% sucrose solution at 18,000 g as described in the Experimental Section (in Chapter 2). Surprisingly, reconstituted SL-TMH4 peptides did not separate under these conditions; only the top band was collected back after the centrifugation. We speculate that TMH4 does not form aggregates with the structure corresponding to that in the bottom layer from TMH5 samples. Each individual layer was then characterized by Attenuated Total Reflectance FT-IR (ATR FT-IR), <sup>31</sup>P NMR, and X-band EPR spectroscopies and confirmed the CesA TMHs oligomerization in the lipid bilayer.

ATR FT-IR spectra acquired from the individual layers from TMH5 and membrane-embedded TMH4 are shown in Figure 3.5(B). The spectrum of spin-labeled  $\alpha$ -helical non-aggregating transmembrane WALP23 C10 peptide is also shown as a reference. Typically,

the ATR FT-IR absorption band at about  $1655\text{ cm}^{-1}$  is assigned to an  $\alpha$ -helical structure, and the one at  $1625\text{ cm}^{-1}$  to an extended  $\beta$ -structure.<sup>81-84</sup> The spectrum from the bottom layer of TMH5 (dash-dotted line) shows a strong absorption band at  $1629\text{ cm}^{-1}$  which is an evidence of a predominantly  $\beta$ -sheet structure<sup>84</sup> and a small shoulder at  $1656\text{ cm}^{-1}$  which is typically ascribed to an  $\alpha$ -helical structure. The spectrum of the top layer for TMH5 (dotted line) shows absorption maxima at  $1630$ ,  $1640$ , and  $1648\text{ cm}^{-1}$ . The first two frequencies serve as an evidence for a significant contribution from the  $\beta$ -sheet structure.<sup>84</sup> The absorption band at  $1648\text{ cm}^{-1}$  could be attributed to a random coil.<sup>84</sup> There is also a absorption maximum at  $1654\text{ cm}^{-1}$  corresponding to the  $\alpha$ -helical structure ( $1655\text{ cm}^{-1}$  for spin-labeled WALP23 C10 peptide, Figure 3.5). The membrane-embedded TMH4 (dashed line) shows a small  $\beta$ -sheet contribution ( $1640\text{ cm}^{-1}$ ) and the absorption peak centered at  $1656\text{ cm}^{-1}$  corresponding to an  $\alpha$ -helical structure. Note that the absorption band of the reference WALP23 C10 peptide also shows a weak high-frequency shoulder that presumably originates from small contributions of the  $\beta$ -strands. Thus, based on ATR FT-IR data we came to a conclusion that the top layer of TMH5 is enriched with a higher  $\alpha$ -helical content and the bottom, more tightly packed layer, contains, basically, the extended  $\beta$ -strands. TMH4 shows a noticeably higher, compared to the top layer of TMH5,  $\alpha$ -helical content.

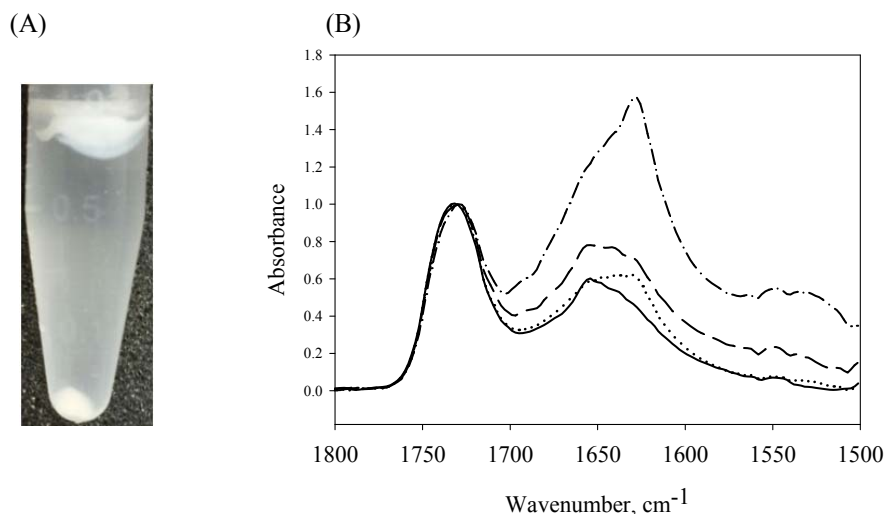


**Figure 3.5** (A) A photograph of the centrifuge tube taken after the 3% sucrose separation of SL-TMH5 L13C peptide reconstituted to DOPC lipids. (B) ATR FT-IR spectra from the individual layers obtained after the sucrose separation of the native TMH5 peptide reconstituted to DOPC lipids (top layer, dotted line; bottom layer, dash-dotted line). FT-IR spectrum of the DOPC-embedded native TMH4 is shown in dashed line. The spectrum of the reference MTSL-labeled WALP23 C10 is shown in solid line. The intensities were normalized by the absorbance of the lipid  $\nu$  (C=O) vibration around  $1736\text{ cm}^{-1}$ .

We have further examined the fractions obtained after the sucrose centrifugation, with  $^{31}\text{P}$  solid state NMR that is a highly sensitive to changes in lipid phase behavior.<sup>85</sup> The  $^{31}\text{P}$  NMR spectra from the membrane-embedded TMH4 showed a powder-pattern with axially symmetric anisotropic peaks that is typical for a bilayer organization ((A))<sup>86-87</sup>. The top layer obtained after sucrose centrifugation of the lipid-reconstituted TMH5 exhibits a similar spectrum corresponding to the normal bilayer structure with a small isotropic peak centered

near 0 ppm which represents an isotropic phase induced by TMH5 peptide (Figure 3.6 (B))<sup>33</sup>. The bottom layer from TMH5 sample showed a similar powder-pattern spectrum with a small isotropic peak but much smaller intensity (Figure 3.6 (C)). Thus, we speculate that the bottom layer represents an unstructured aggregate of TMH5 peptide doped with small amount of disordered lipid phase<sup>88</sup> and a minor impurity of the bilayer phase picked up from the top layer.

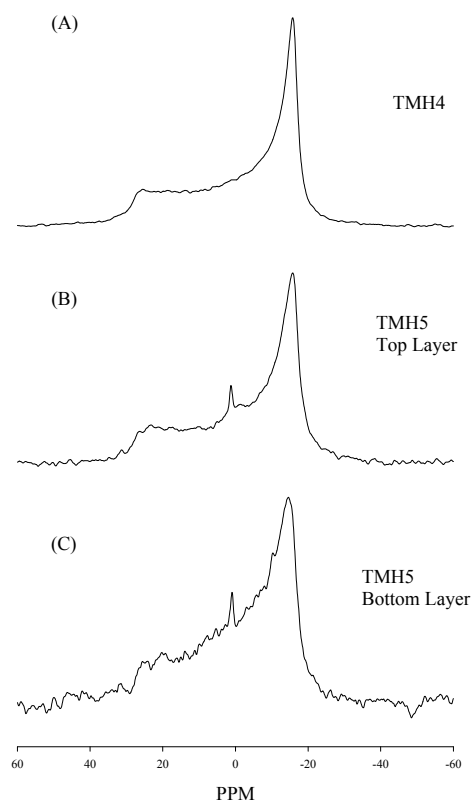


**Figure 3.6** Room temperature <sup>31</sup>P solid NMR spectra from the membrane-embedded TMH4 (A) and the top layer (B) and bottom layer (C) obtained after sucrose centrifugation of TMH5 reconstituted in DOPC bilayers.

A series of X-band EPR spectra from the top and the bottom layers obtained using the sucrose centrifugation of SL-TMH5 variants reconstituted to DOPC lipids are shown in Figure 3.7. However, the samples containing SL-TMH5 C2 and L13C still exhibit the highest content of the aggregated component.

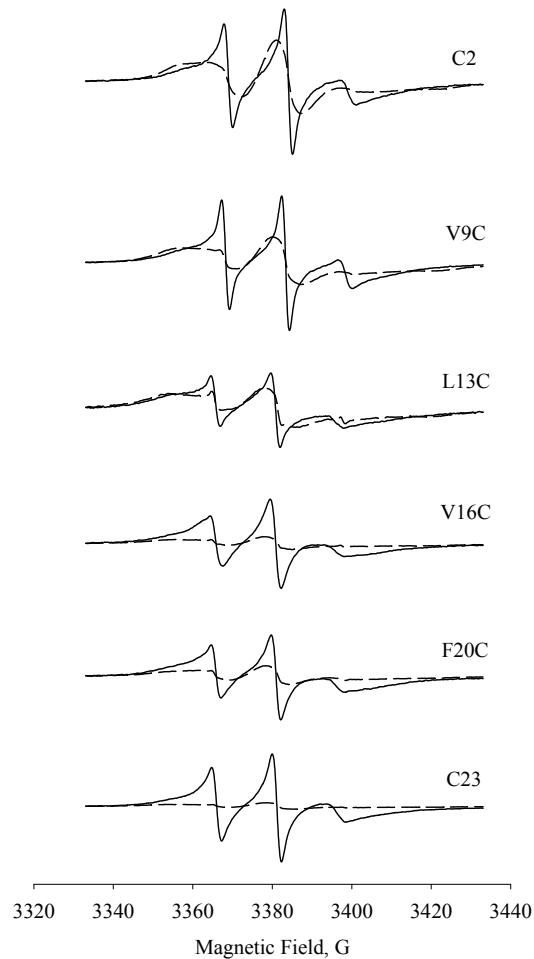


**Figure 3.7** X-band EPR spectra from the individual layers obtained after sucrose differential centrifugation of SL-TMH5 variants reconstituted to DOPC lipids: top layer (solid line), bottom layer (dashed line). Labeling sites are shown next to the corresponding spectra.

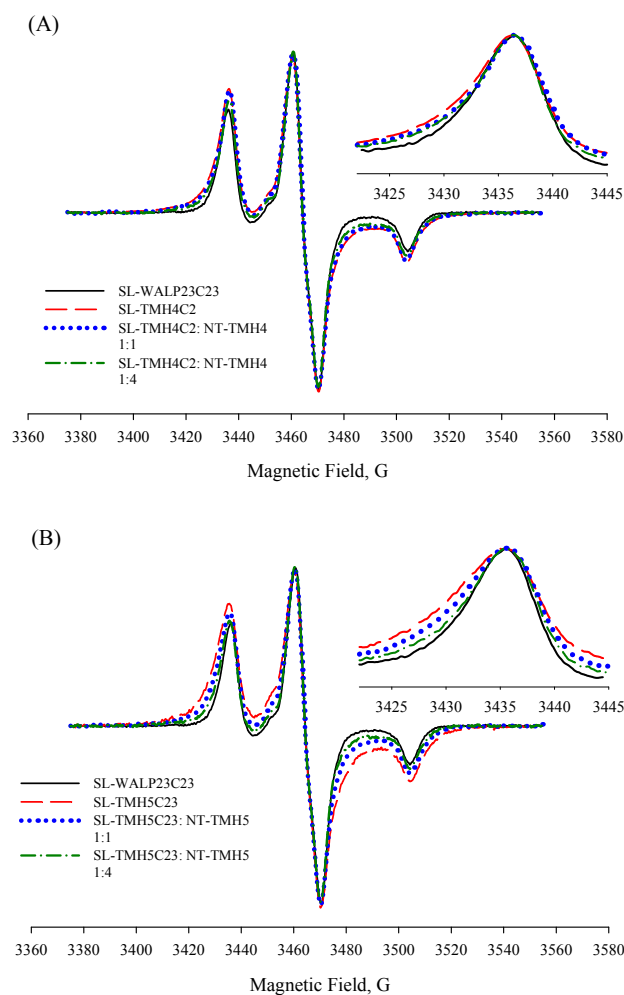


**Figure 3.8** X-band (9.5 GHz) EPR spectra acquired from SL-TMH4 C2 (A) and SL-TMH5 C23 (top layer collected after sucrose separation) (B) magnetically diluted with corresponding native TMH peptides in 1:1, and 1:4 ratios (see text inset) at 140K. The high field spectral components are shown enlarged in the inserts. The rigid-limit EPR spectrum of non-aggregated SL-WALP23 C23 in DOPC bilayers is shown as a reference. For the presentation purpose, because of the difference in  $A_{zz}$  of SL-WALP23 and SL-TMHs, the positions of the spectral components of the former were adjusted for -0.4 G for the low field component (A) and for 0.5 G for the high field component (B), respectively.

To ascertain whether SL-TMH4 and SL-TMH5 in the top layer exist as individual helices or partially oligomerized, we carried out the magnetic dilution EPR experiments by gradually increasing the fraction of a native, unlabeled peptide, over the SL-TMH peptide, but keeping the total peptide-to-lipid ratio constant. The EPR experiments we carried out at 140K; at this temperature the EPR spectra fall into extremely slow motion regime, so all the dynamic effects changing the EPR line width can be excluded and only static effects from the peptide association should be considered. Co-insertion of SL-TMH with native TMH peptides (NT-TMHs) will result in replacement of some of the SL-TMHs in the magnetically interacting spin-labeled pairs with native peptide, thus decreasing the number of inter-helical dipole-dipole interactions and, as a result, increasing the amplitude of the EPR signal (decreasing the line width). The SL-TMH4 C2 and SL-TMH5 C23 variants mixed with corresponding native TMH4 and TMH5 peptides (Sequence see Table 2.2 and Table 2.3) in 1:1 and 1:4 ratios were reconstituted to DOPC lipids. The SL-TMH5 samples were separated by sucrose centrifugation and only the top layers were subjected to analysis. The EPR peak-to-peak line broadening effect (most pronounced for the low field spectral component) is gradually decreasing with increasing of the SL-TMH:NT-TMH ratio indicating that both TMH4 (Figure 3.8 (A)) and TMH5 (Figure 3.8 (B)) exist in the top layers in somewhat oligomerized form. In general, the EPR spectra of SL-TMH5 C23 (top layer) are more broadened than those of SL-TMH4 C2. Therefore, the spectral line narrowing induced by a magnetic dilution is more pronounced for SL-TMH5 C23 samples. The narrowing effects were calculated according to Smirnov et al<sup>36</sup> using the spectra collected for 1:4 magnetically diluted samples as a reference (see Table 3.1). We chose the 1:4 magnetically diluted TMH5

sample as the reference because this sample revealed only negligible line broadening compared to the spectrum of non-aggregating SL-WALP23 C23 peptide incorporated into DOPC lipids measured at 140K (Figure 3.8, A and B, solid line). The spectrum of 100% spin labeled TMH4 C2 was calculated to be 1.26 G broadened compared to the spectrum collected from its 1:4 magnetically diluted sample; the broadening effect decreases to 0.82 G for 1:1 diluted TMH4 C2 sample. The spectrum from the bottom layer of SL-TMH5 C23 collected from sucrose separation was calculated to be 4.08 G broader compared to the reference spectrum (Table 3.1); only 1.94 G broadening effect was observed for the spectrum of the top layer. The broadening was further reduced to 1.06 G for 1:1 magnetically diluted TMH5 C23 sample.

**Table 3.1 Calculated broadening of SL-TMHs relative to the 1:4 magnetic diluted spectra at 140K.**

<b>Sample</b>	<b>Broadening, G</b>	<b>Reference spectrum</b>
SL-TMH4 C2	1.26	SL-TMH4C02: NT-TMH4, 1:4
SL-TMH4 C2: NT-TMH4, 1:1	0.82	
SL-TMH5 C23, Bottom Layer	4.08	SL-TMH5 C23: NT- TMH5, 1:4
SL-TMH5 C23, Top Layer	1.94	
SL-TMH5 C23: NT-TMH5, 1:1	1.06	
SL-TMH5 C23: NT-TMH4, 1:1	1.77	
SL-TMH5 C23: NT-TMH4, 1:4	1.08	
SL-TMH 5C23: NT-TMH4, 1:9	0.45	

### 3.2.3 Organization of CesA TMHs in lipid bilayers

A series of spin-labeling EPR experiments has been carried out to derive bilayer arrangement of the individual CesA TMH helices. Specific experiments included:

*(i) Oxygen accessibility and polarity profiles of the spin-labeled side chains in CesA TMHs*

Profiling the local environment based on molecular accessibility of nitroxide-labeled side chains systematically attached along the peptide backbone is another EPR-based experimental approach that allows one to determine the membrane organization of a peptide.

One way to measure molecular accessibility parameter is by quantifying EPR line width broadening caused by paramagnetic molecular oxygen as a result of Heisenberg spin exchange interaction with the nitroxide. The broadening is proportional to rates of molecular collisions between the nitroxide and oxygen. As discussed in Chapter 1, translational diffusion of the nitroxide-labeled peptide chain in the membrane is slower than that of oxygen, and, therefore, collision rate and the broadening effect is proportional to the product of the molecular oxygen diffusion coefficient and local oxygen concentration (that is given by the product of oxygen partial pressure and the solubility coefficient).<sup>89</sup> In general, oxygen permeability profile across the lipid bilayer in the fluid phase is inverse of that of the transmembrane polarity; however, it could be significantly affected by water penetration into the hydrophobic interior<sup>90</sup> as well as by the presence of transmembrane protein residues.<sup>37</sup> One would expect a larger effect on local oxygen accessibility if the adjacent amino acid residues are polar.

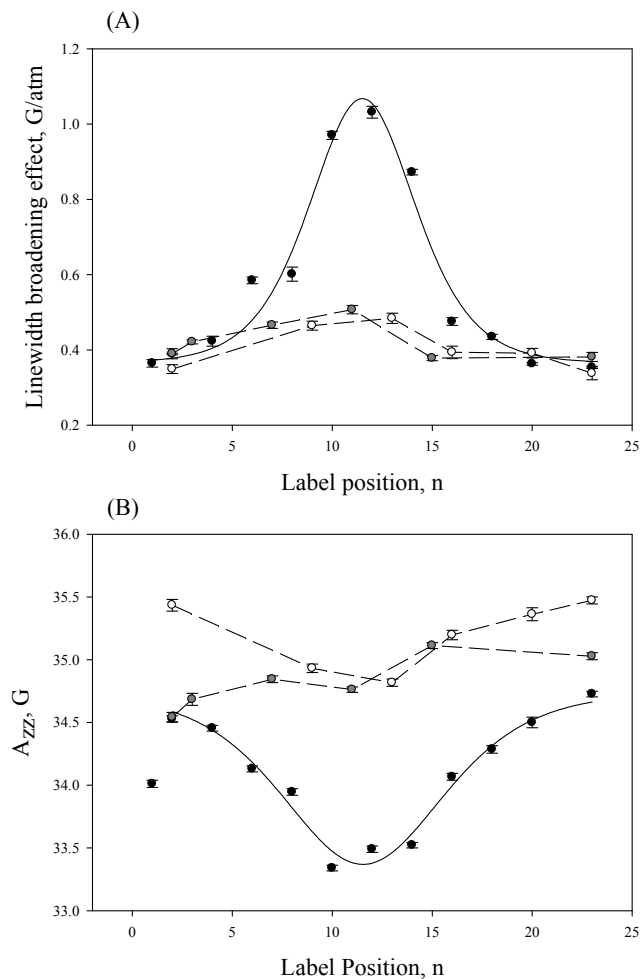


**Figure 3.9** Oxygen line width and polarity profile of TMH4 and 5 in DOPC membrane. (A): Oxygen induced EPR spectral line width broadening of SL-WALP23 (●), TMH4 (●), and TMH5 (○) peptides reconstituted to DOPC vesicles shown as a function of the spin-labeling position. (B): Anisotropic nitrogen hyperfine splitting constant  $A_{zz}$  of MTSL-labeled WALP23 (●), TMH4 (●), and TMH5 (○) peptides reconstituted to DOPC vesicles shown as a function of the spin-labeling position. Solid lines are the least-squares fits of the experimental data to the Equation 2.3. The dashed lines connect the data points acquired for the SL-TMH5 samples and serve as guides for an eye.

Both room-temperature EPR line width broadening caused by molecular oxygen and anisotropic nitrogen hyperfine coupling constant  $A_{zz}$  from the rigid-limit CW EPR spectra were measured for a series of spin-labeled Cesa TMH4 and 5 peptides reconstituted into DOPC bilayers. The oxygen accessibility and  $A_{zz}$  data for the two Cesa TMHs were compared with the corresponding data for the membrane-spanning non-aggregating WALP23 peptide<sup>38</sup> in the vesicles composed of the same DOPC lipid. In the past WALP23 peptide has been employed as a ruler for studying the depth-dependent properties of the lipid bilayers<sup>28</sup>. For the lipid-reconstituted TMH5 samples only the top, enriched with  $\alpha$ -helical content layers, obtained after sucrose centrifugation (*vide supra*) were used for these measurements.

The EPR line width broadening and  $A_{zz}$  data for TMH4 and 5, along with the corresponding data for the SL-WALP23 peptides, are plotted as a function of the spin-labeled position in Figure 3.9. Both the line width broadening and  $A_{zz}$  profiles obtained for TMHs show the trends similar to that for WALP23 peptide, although the TMH profiles are significantly shallower. Thus, spin labels in positions 2, 20 and 23 of TMH5 and positions 2, 3 and 23 of TMH4 (see Table 2.1 and Table 2.2) that are supposedly located within the polar head group region of DOPC<sup>28</sup> are experiencing the EPR line width broadening effect similar to that for close positions in WALP23 ( $\approx 0.4$  G/atm  $O_2$ , Figure 3.9, (A)).

However, the nitroxides in the position 11 of TMH4 and position 13 of TMH5 that practically coincide with the center of the bilayer show only a slight increase in the line broadening ( $\approx 0.5$  G/atm  $O_2$  vs.  $\approx 1.0$  G/atm  $O_2$  for a similar position in WALP23). The nitrogen hyperfine coupling constant profile shows  $A_{zz}$  for positions 2 and 23 in TMH5 of about  $A_{zz} \approx 35.5$  G; the corresponding spin-labeled positions in the WALP23 experience less

polar environment characterized by  $A_{zz}$  value of approximately 1.0 G lower ( $A_{zz} \approx 34.5$  G). The  $A_{zz}$  values for terminal position 2 ( $A_{zz} \approx 34.5$  G), 3 ( $A_{zz} \approx 34.7$  G) and 23 ( $A_{zz} \approx 35.0$  G) of TMH4 are shifted to a less polar region and are close to  $A_{zz}$  for the corresponding positions of WALP23. Similarly, the positions of the TMH4 and 5 corresponding to the center of the lipid bilayer yield much more polar  $A_{zz} \approx 34.8$  G vs.  $A_{zz} \approx 33.3$  G for WALP23 (Figure 3.9, (B)). We speculate that unexpectedly low oxygen accessibility and a high local polarity of the environment as determined from the magnitude of  $A_{zz}$  could be rationalized accepting the fact that in the lipid membrane CesA TMHs basically exist in an oligomerized state. If this is true, the oxygen effect on the spin-labeled residues in the positions 2, 20 and 23 of TMH5 and positions 2, 3 and 23 of TMH4 is most likely to be determined by oxygen solubility in the polar head group region of the lipid bilayer, which produces a similar effect for both TMHs and WALP23 peptides. In the aggregated state, a significant fraction of nitroxides is expected to be buried amongst the peptide chains and is not exposed towards the lipid phase. If such buried nitroxides fall into the hydrophobic region of the bilayer, oxygen solubility in the polar phase of the aggregate, but not in the lipid phase, will be dictating the EPR line broadening. Even if the observed ranges of  $A_{zz}$  variations for TMH4 (34.5 – 35.1 G) and TMH5 (34.8 – 35.5 G) fall into an  $A_{zz}$  range that is significantly more polar compared to that of WALP23 (33.3 – 34.8 G), it is still less polar than  $A_{zz}$  of MTSL in frozen aqueous solution, which has been reported to be  $A_{zz} = 36.5$  G.<sup>91</sup> The latter fact indicates that the nitroxide moieties in SL-TMH peptides are far from being exposed to the bulk aqueous phase. Furthermore, such high  $A_{zz}$  values for MTSL-labeled buried sites in membrane proteins have already been reported in the literature. For example, in bacteriorhodopsin, the

MTSL spin labels attached to the residues T170C (terminus of helix F, oriented towards helix G) and L100C (terminus of helix C) located in the interior of the protein, yielded rather high  $A_{zz}$  values of about  $A_{zz} \approx 35.9$  G and  $A_{zz} \approx 35.5$  G, respectively. Such high magnitudes of  $A_{zz}$  were interpreted in terms of polar interaction with the proximal  $\alpha$ -helices<sup>91</sup>. The polarity within the aggregate could also increase owing to water molecules drawn by TMH to the hydrophobic interior of the bilayer.<sup>92-96</sup> Thus, we speculate that the anisotropic  $A_{zz}$  parameter from the rigid-limit EPR spectra most likely reports on the polarity of hydrated interior of the aggregate.

***(ii) Motion of the spin-labeled acyl chain in n-doxyl-PC as an indicator of lipid-peptide interactions***

As discussed above, the EPR spectra are exceptionally sensitive to molecular motions of the spin probes<sup>16,73</sup> and one could take advantage of such sensitivity to study peptide-lipid interactions.<sup>97</sup> If exchange between the bulk spin-labeled lipids (SL-lipids) in the membrane and those interacting/closely associated with the membrane peptide or proteins is slow on the EPR time scale, then the two fractions could be observed and resolved from EPR spectra. When the lipid bilayer is in a fluid phase the EPR lines of the lipids spin-labeled at the position close to the terminus of the acyl chain are approaching the fast motional limit and are relatively narrow, due to effective averaging of magnetic anisotropies fast motion and small order parameter. This makes the lipids with terminally spin-labeled acyl chain especially suitable for detecting the restricted motions arising from the interaction of SL-lipids with transmembrane regions of peptides/proteins. Thus, in this study we employed the

spin-labeled 12-*doxyl*-PC and 16-*doxyl*-PC lipids (Figure 3.10). If a peptide embedded into the lipid bilayer acquires a transmembrane arrangement, the EPR spectrum of *n*-*doxyl*-PC is expected to show the two populations<sup>73</sup> corresponding to SL-lipids in the bulk lipid phase and those interacting with the transmembrane fragment of the peptide. If a peptide is not spanning the membrane but bound to or partitioned into the bilayer interface, the EPR spectra of the lipid with terminally spin-labeled acyl chains are not expected to have any changes. In order to increase the fraction of SL-lipids interacting with peptides, peptide-to-lipid ratio was increased to 1:25. Also, the spectral resolution was improved by equilibrating the sample with N<sub>2</sub> to eliminate EPR line broadening caused by Heisenberg spin exchange between oxygen dissolved in the sample and the nitroxide.

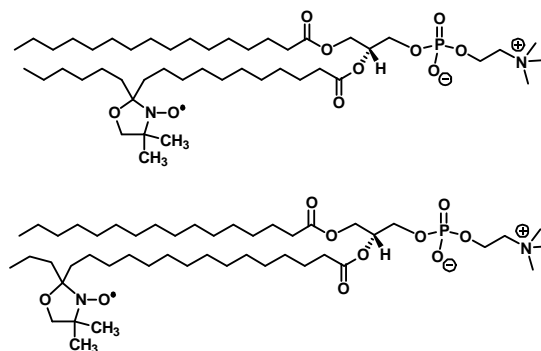


**Figure 3.10** Chemical structures of spin-labeled phospholipids 12-*doxyl*-PC and 16-*doxyl*-PC.

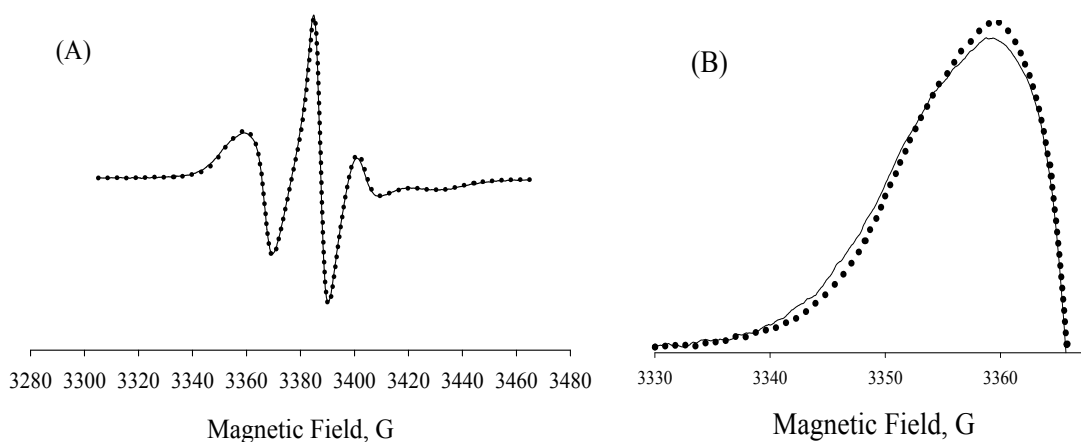


**Figure 3.11** (A) X-band (9.5 GHz) EPR spectra of  $N_2$ -equilibrated DOPC vesicles doped with 1 mol% of 12-doxyl-PC measured in the absence (dotted line) and presence (solid line) of CesA TMH5. The spectra were measured at 11 °C and pH = 7.0 for the peptide-to-lipid ratio of 1:25. The spectra are normalized by spectral intensities. (B) Zoom-in low field components of the same spectra.

For experiments at room temperature no changes in EPR spectra were detected. This could be due to the exchange rate between the two populations of SL-lipids being too fast on the EPR time scale. At 11 °C, in the presence of CesA TMH5 peptide the spectrum of 12-doxyl-PC appeared somewhat broader although the two components were not resolved (Figure 3.11 (A)). This broadening was more readily detected in the low-field region of the spectrum (low-field spectral component is shown enlarged in Figure 3.11 (B)).

Empirical order parameter  $S$  (Equation 3.1) of the spin probe was calculated from the inner and outer apparent nitrogen hyperfine splittings of the experimental intermediate motion EPR spectra (Figure 3.11) as:<sup>98-100</sup>

$$S = \frac{A_{\parallel} - A_{\perp}}{(A_{\parallel} + A_{\perp})/3} \times 0.5407 \quad \text{Equation 3.1}$$

where  $A_{\parallel}$  and  $A_{\perp}$  are a one half of the outer and inner hyperfine splittings, respectively.

$A_{\parallel}$  and  $A_{\perp}$  were measured to be 35.4 and 15.8 G for lipids without TMH5 and 36.2 and 15.7 G for TMH5-containing sample. The calculated lipid order parameter for TMH5-containing sample was slightly larger (0.492) than that of the control one (0.475). Although the trend in the order parameter indicates the presence of boundary lipids, the change is only moderate, likely because of still fast spin-exchange between the two lipid compartments.

We also tried to detect motion-restricting effects of Cesa TMHs on the EPR spectra of a more freely moving nitroxide in 16-*doxyl*-PC lipid. However, the tumbling rate of the nitroxide in the latter appeared to be too fast and no line broadening effect has been observed even at 0 °C.

Effect of Cesa TMHs membrane insertion on local polarity in the center of the lipid bilayer was assessed by measuring anisotropic nitrogen hyperfine coupling constant  $A_{zz}$  from the rigid-limit ( $T = 77$  K) EPR spectra of DOPC vesicles doped within 1 mol% of 16-*doxyl*-PC in the absence and presence of native TMH5. The  $A_{zz}$  measurement allows to characterize the local environment of the spin probe in the absence of dynamic effects; an exquisite dependence of the nitrogen hyperfine coupling constant of nitroxides on the local polarity and formation of hydrogen bonds with nitroxide moiety is well documented in the literature.<sup>101</sup> The magnitude of  $A_{zz}$  for the sample containing TMH5 was found to be slightly higher (33.3 G vs. 33.0 G) than that in the absence of TMH. This observation was attributed to a more polar environment of the nitroxide in 16-*doxyl*-PC bound to a membrane-spanning

peptide backbone, and, perhaps, some additional water penetration into the lipid bilayer along the peptide-lipid interface.

Finally, oligomerization of TMH 4 and 5 in DOPC bilayers would also explain negligible effects of the TMH5 on lipid dynamics and local polarity as probed by 12- and 16-doxyl-PC lipids. Indeed, formation of an oligomer would drastically decrease the fraction of the lipids in the immediate contact with the peptides and decrease the magnitude of the observed effects.

***(iii) Interaction of TMH4 and TMH5 co-inserted into lipid bilayer***

Interactions between transmembrane helices are important for membrane protein stability, its folding into correct secondary structure, and formation of supramolecular protein assemblies<sup>2, 7, 102</sup>. It is especially vital for polytopic membrane proteins that contain several transmembrane  $\alpha$ -helices, connected by relatively hydrophilic loops and spanning the membrane in a zigzag fashion. In the living cells, the  $\alpha$ -helices are inserted into the lipid membrane by a translocon that is responsible for correct folding and inserting the proteins into the heterogeneous environment of the membrane. In the latter process the directionality of insertion and association of the loop-separated  $\alpha$ -helices are commanded by the overall structure of the transmembrane domain. It is a quite different story when the loops connecting  $\alpha$ -helices are removed. If this happens, will the individual interacting  $\alpha$ -helices, such as Cesa TMH4 and TMH5, be interacting when inserted into the lipid bilayer and form a pair with the same relative orientation? From the biophysical perspective, will TMH4 and TMH5 be mixed in the lipid bilayer or each will form an individual domain?

To answer this question, we tested the miscibility of the SL-TMH5 C23 variant and native TMH4 peptide (NT-TMH4) carrying out the magnetic dilution experiment. If TMH4 and TMH5 would associate in the same manner as in the native protein, a spectral line narrowing similar to that for SL-TMH5 C23 magnetic diluted with native TMH5 (NT-TMH5) (Figure 3.8 (B)), is supposed to be observed.

To ensure that TNH5 and TMH4 peptides were mixed in exactly the same ratios as required we needed to determine the concentration of the inserted TMH5 fraction after the non-inserted aggregated peptide was removed by sucrose separation. Thus, we compared the double integrals of the EPR spectra of SL-TMH5 C23 in DOPC vesicles measured before sucrose separation and from the top layer obtained after the separation. According to the <sup>31</sup>P SS-NMR, the aggregated peptide (bottom layer) contains only negligible amount of lipids, so we assumed that amount of lipids in the top layer was the same as before the sucrose separation. Thus, according to our estimate, the top layer obtained after sucrose separation contains about 90% of the amount of the SL-TMH5 C23 peptide in the sample before separation.

Thus, taking this estimate into consideration we mixed SL-TMH5 C23 and NT-TMH4 peptide (Sequence see Table 2.2 and Table 2.3) in 1:1, 1:4 and 1:9 final ratios and reconstituted them to DOPC bilayers. The broadening effects were calculated using spectra collected for SL-TMH5 1:4 magnetically diluted with NT-TNH5 as a reference (see Table 3.1). The spectrum of non-diluted SL-TMH5 C23 variant was calculated to be 1.94 G broadened compared to the spectrum collected from its 1:4 magnetically diluted sample; the broadening effect remained the same when SL-TMH5 C23 was diluted with equimolar

amount of NT-TMH4. 1:4 dilution of SL-TMH5 C23 with NT-TMH4 yielded the spectrum that was about 1G broadened compared to the reference. The spectrum of SL-TMH5 C23 diluted with NT-TMH4 at 1:9 ratio, the broadening effect was calculated to be 0.45 G compared to the reference spectrum (Table 3.1). Thus, these magnetic dilution EPR experiments showed that in the absence of the connecting cytoplasmic loop, the individual  $\alpha$ -helices of Cesa TMH4 and TMH5 peptides inserted into the lipid bilayers associate in the fashion different from that in native protein<sup>20</sup>. Cesa TMH5 peptide inserted into the lipid bilayers was found to have a higher than TMH4 tendency to self-association.

### 3.3 Conclusion

In the present report the site-directed spin-labeling EPR technique was employed for the first time to analyzing the membrane arrangement of transmembrane  $\alpha$ -helices TMH4 and TMH5 from the transmembrane domain of cellulose synthase GhCesA1 from cotton, *Gossypium hirsutum*. The cytoplasmic loop connecting TMHs 4 and 5 in the protein was removed to elucidate the role it plays in the TMHs insertion, transmembrane assembly, and relative orientation of TMHs. Circular dichroism measurements show that both in TFE solution and a lipid membrane native and spin-labeled TMHs (SL-TMHs) acquire an  $\alpha$ -helical structure. However, the X-band EPR spectra revealed a significant contribution of broadened spectral component suggesting that TMHs are largely aggregated in the membrane. Oligomerization of the Cesa TMHs in the lipid bilayer was also confirmed by Attenuated Total Reflectance FT-IR spectroscopy. A series of lipids containing both

saturated and unsaturated acyl chains of various lengths was tested and 1,2-dioleoyl-*sn*-glycero-3-phosphocholine (DOPC) was found to show the best hydrophobic match for TMHs with the least aggregation formed. The fractions of aggregated TMHs were found could be separated using sucrose centrifugation. The top layer of TMH5 was found to be enriched with a higher  $\alpha$ -helical content and the bottom, more tightly packed layer, contains, basically, the extended  $\beta$ -strands. TMH4 shows a noticeably higher, compared to the top layer of TMH5, an  $\alpha$ -helical content. However, the magnetic dilution EPR experiments demonstrated that TMH5 helices are largely aggregated even in the top fraction. This intrinsic ability of TMH5 to self-associate in the membrane might indicate its implication to formation of higher order assemblies from GhCesA1. From profiling oxygen accessibility and polarity of the spin-labeled side chains in Cesa TMHs, we concluded that oligomerized TMHs acquire a transmembrane arrangement. Spin-labeling EPR experiments with SL-TMH5 C23 reconstituted in pair-wise manner with various molar ratios of native TMH4 shows less broadening effect compared to that magnetic diluted with native TMH5 at the same molar ratio. This observation demonstrates that without the connecting inter-helical loop, the co-inserted  $\alpha$ -helices is not able to retain the original association manner and is another proof of strong interhelical association between TMH5 peptide in the membrane.

## Chapter 4 Ionization state of amino acid residues and inter-helical oligomerization

### 4.1 Introduction

Membrane proteins are typically featured with an extended transmembrane domain that not only anchors protein to the lipid membrane but is also involved into protein activity. For example, a polytopic transmembrane domain of the bacterial cellulose synthase from *Rhodobacter sphaeroids* (complex BcsA-BcsB) has recently been shown to be actively participating in translocation of growing glucan chain<sup>19</sup>. Membrane-spanning  $\alpha$ -helices are basically built of hydrophobic amino acids, with polar and ionizable residues rarely found in their structures<sup>103-105</sup>. Although scarcely represented, polar amino acid residues are rather conserved in the structure of transmembrane helices (TMH), which is likely because of their importance for the protein function<sup>106-107</sup>, folding, and stability<sup>6</sup>. Evidences collected so far strongly indicate that polar residues promote oligomerization of hydrophobic transmembrane segments through intermolecular hydrogen bonding<sup>108-109</sup>. Changes in the ionization state of the amino acid residues residing within the hydrophobic core of TMHs or in the flanking positions have been reported to influence stability and membrane topology of TMHs and could also cause their oligomerization.<sup>110-114</sup> The latter phenomenon could present certain challenges during biophysical studies of individual TMHs.

During our ongoing spin-labeling EPR studies on membrane arrangement of the individual transmembrane helices TMH4 and TMH5 from transmembrane domain of the plant cellulose synthase GhCesA1 from cotton, *Gossypium hirsutum*, we encountered a strong aggregation behavior of TMH5 when it is inserted into the lipid membrane at neutral

pH (Chapter 3). CesA TMH5 peptide (EQFWVIGGVSAHLFAVFQGFLKML, residues 817-840) contains several polar amino acid residues – the ionizable His in the center of the  $\alpha$ -helix and Glu and Lys in the flanking position as well as the hydrogen bonding Gln and Ser residues. The aggregation most likely originates from the electrostatic interactions between Glu and Lys residues. In the lipid bilayer, these residues are expected to reside near the interfacial region. If so, Glu and Lys will be exposed to aqueous phase and  $pK_a$ 's of side chain groups in these residues will be close to that in aqueous solution ( $pK_a=4.25$  and  $10.79$ , respectively) and they will be oppositely charged at neutral pH. Thus, packing of individual  $\alpha$ -helices in an anti-parallel fashion<sup>102, 115-117</sup> will benefit from the electrostatic stabilization. Within the native transmembrane domain of the CesA these charged residues could also be involved into interaction with the neighboring helices or formation of supramolecular CesA assemblies. The  $pK_a$  of His residue buried within the low dielectric bilayer core is supposed to be significantly diminished<sup>118</sup>; as a result, it is expected to exist in its neutral form and contributes to the helix-helix interaction only through hydrogen bonding interactions. This particular His residue seems to be highly conserved within the family of CesA proteins<sup>20</sup> and might be involved into the protein function.

Using individual synthetic  $\alpha$ -helices in biophysical studies is highly advantageous because creates a unique opportunity to interrogate them under a broad range of physicochemical conditions to understand fundamental aspects of membrane protein structure, such as configuration of transmembrane helices and helix-helix interactions. If the oligomerization of TMH5 is in fact primarily dominated by the presence of charged residues at the ends of the helix, a proper pH adjustment is assumed to cause at least partial TMH5

disaggregation. Herein we report on our site-directed spin-labeling (SDSL) EPR studies aimed to elucidate the effect of pH (i.e., presence of charged residues) on the oligomerization state of Cesa TMH5 peptide. In this study, we were using a library of 24-mer TMH5 model peptides chemically synthesized through SPPS. To site-specifically label these TMHs with methanethiosulfonate spin label methanethiosulfonic acid S-(1-oxy-2,2,5,5-tetramethyl-2,5-dihydro-1H-pyrrol-3-ylmethyl) ester (MTSL, spin label III in Figure 1.1), selected amino acids in the hydrophobic patches of the peptides were single point-mutated to cysteine.

## 4.2 Results and discussions

EPR spectra of nitroxides are exceptionally sensitive to the rotational dynamics of the protein side chain<sup>16, 73</sup>. Restriction of rotational mobility of the nitroxide manifests itself in significant spectral changes, e.g., spectral broadening.<sup>16, 29</sup> Thus, the event of aggregation of spin-labeled peptides/proteins could be deduced from appearance of broad components in the EPR spectra<sup>75-76</sup>.

The native transmembrane helix TMH5 from the transmembrane domain of the plant cellulose synthase GhCesA1 from cotton, *Gossypium hirsutum*, as well as its variants with the selected amino acids in the hydrophobic face of the peptide single point-mutated to cysteines, were synthesized through solid phase peptide synthesis (SPPS) ((Table 2.2)). Cysteines were strategically positioned within the hydrophobic patches along the peptide backbone to (i) continuously probe the environment along the peptide backbone and (ii) not to interfere with the polar residues that are expected to participate in the inter-helical

association. The side chain of cysteine was used to covalently attach a thiol-specific methanethiosulfonate nitroxide MTSL. The one-letter sequences of the peptides used in this study and corresponding codes are given in (Table 2.2).

As it has already been reported in Chapter 3, reconstitution of Cesa TMH5 to the lipid bilayer induces formation of the two phases that could be separated through sucrose differential centrifugation – a strongly aggregated peptide with practically no lipids bound, and somewhat oligomerized TMH inserted into a lipid bilayer. In this work, we used only the top, containing the bilayer phase, fraction obtained after the sucrose centrifugation. We hypothesize that if the lipid-reconstituted TMH5 will be acidified, the side chains of the surface-exposed Glu ( $pK_a = 4.25$ ) will become electrically neutral, and Lys ( $pK_a = 10.79$ ) will remain positively charged. As a result, the electrostatic interaction between TMH5 helices will be abolished, which is assumed to affect the peptides' aggregation state and its secondary structure. The lipid-reconstituted TMH5 samples were pH-equilibrated in two different ways. The samples rehydrated with a buffer at pH = 7.0 were sucrose separated first, and then the top layer was rehydrated with a buffer at pH = 3.3 through several consecutive freeze-thaw cycles; or, the sample was rehydrated with a buffer at pH = 3.3, and only after this it was sucrose separated. Both methods gave essentially the same result.

Circular Dichroism (CD) Spectroscopy. First, we examined the secondary structure of the reconstituted TMH5 with circular dichroism spectroscopy. Figure 4.1 shows the CD spectra of the spin-labeled Cesa TMH5 V9C peptide reconstituted to 100 nm unilamellar DOPC vesicles and equilibrated at neutral (pH = 7.0) and acidic (pH = 3.3) pH. Despite that

the peptide concentrations were the same, the amplitude of the spectrum acquired from the sample equilibrated at pH = 3.3 was almost 4-fold higher. This sample showed the CD spectrum typical for  $\alpha$ -helices with two negative peaks at 208 and 223 nm and helical content of 76 %. The spectrum from the sample equilibrated at pH = 7.0 showed a significantly decreased molar ellipticity at 223 nm with a much lower helical content of 12 %. The helical content was calculated using the method published in.<sup>119</sup>

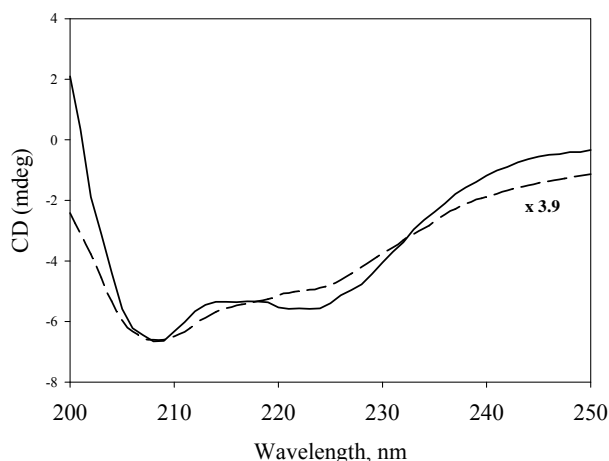


**Figure 4.1.** Circular dichroism spectra of MTSL-labeled Cesa TMH5 V9C peptide in 100 nm unilamellar DOPC vesicles equilibrated with buffers at pH = 7.0 (dashed line) and pH = 3.3 (solid line). Peptide concentration was the same for both samples. For convenience of presentation, the amplitude of the dashed trace was increased 3.9-fold to match the absorption of the solid trace at 208 nm.

Attenuated Total Reflectance FT-IR (ATR FT-IR). Then, we examined the secondary structure of inserted TMH5 with by ATR FT-IR spectroscopy. Figure 4.2 shows FT-IR

spectra in the amide I region of inserted native TMH5 equilibrated at pH = 7.0 and pH = 3.3.

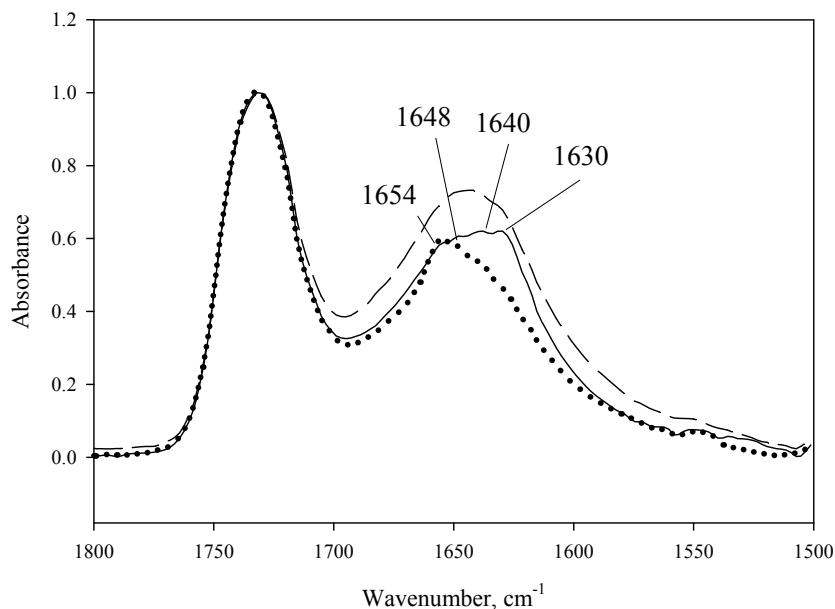


**Figure 4.2** ATR FT-IR spectra from the top layers obtained after the sucrose centrifugation of native TMH5 in 100 nm unilamellar DOPC vesicles equilibrated at pH = 7.0 (solid line) and pH = 3.3 (dashed line), respectively. For reference, the ATR FT-IR spectrum of the MTSL-labeled  $\alpha$ -helical non-aggregating transmembrane WALP23 C10 peptide is shown as a dotted line. The intensities were normalized by the absorbance of the lipid  $\nu$  (C=O) vibration around 1736 cm<sup>-1</sup>.

ATR FT-IR spectrum of the MTSL-labeled  $\alpha$ -helical non-aggregating transmembrane WALP23 C10 peptide is also shown as a reference. Typically, the FT-IR absorption band at about 1655 cm<sup>-1</sup> is assigned to  $\alpha$ -helical structure, and the ones in the range 1625-1642 cm<sup>-1</sup>

– to the extended  $\beta$ -strands.<sup>81-84</sup> The spectrum of the sample equilibrated at pH = 7.0 shows absorption maxima at 1630, 1640, and 1648  $\text{cm}^{-1}$ . The first two frequencies are evidences of predominantly  $\beta$ -sheet structure.<sup>84</sup> The absorption band at 1648  $\text{cm}^{-1}$  could be attributed to a random coil.<sup>84</sup> There is also the absorption maximum at 1654  $\text{cm}^{-1}$ , which is typically ascribed to  $\alpha$ -helical structure (1655  $\text{cm}^{-1}$  for spin-labeled WALP23 C10 peptide, Figure 4.2). Re-equilibration of this sample at pH = 3.3 causes significant changes to the FT-IR spectrum. Thus, the intensities of absorptions responsible for  $\beta$ -sheets reduced, and the resulting absorption peak centered at 1645  $\text{cm}^{-1}$  appears to be mainly contributed by a random coil structure and increased  $\alpha$ -helical content. Note that the absorption band of the reference WALP23 C10 peptide also shows a weak high-frequency shoulder that presumably originates from small contributions of  $\beta$ -strands. Thus, both CD and FT-IR data indicate that abrogation of electrostatic interaction between TMH helices indeed affects their secondary structure.

Spin-labeling EPR. The effect of the ionization state of TMH5 helices on their secondary structure and the bilayer insertion was further elucidated by carrying out a series of spin-labeling EPR experiments. EPR spectra of SL-TMH5 L13C incorporated in DOPC under various pH conditions confirmed a larger aggregated fraction formed under neutral pH environment (Figure 4.3). The spectrum in sharp component extracted by such a filtered fitting procedure<sup>77</sup> is very similar to that of unaggregating peptide in membrane under room temperature. The broad component which obtained by spectral subtraction of sharp component from experiment spectrum is typical for aggregated peptides. The broad

component accounts for *ca.* 94% at pH 7.0, *ca.* 93 % at pH 5.6 and *ca.* 86 % at pH 3.3 of all the spin-labeled peptides in the sample based on calculated values of double-integrated EPR intensities. The trend of decreasing amount of aggregated peptide content at acidic condition is in line with results from CD and FI-IR. Figure 4.4 shows series EPR spectra of SL-TMH5 at various positions embedded in DOPC membrane.

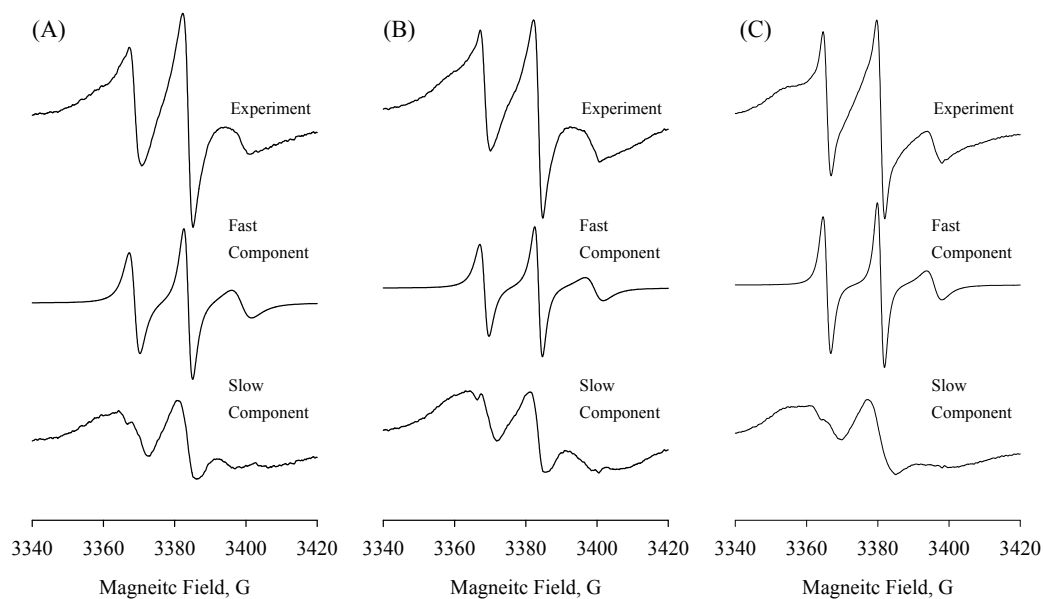


**Figure 4.3** Decompositions of series of X-band (9.5 GHz) EPR spectra acquired from a spin-labeled TMH5 L13C mutant in DOPC lipids hydrated with buffer solutions at pH = 3.3 (A), pH =5.6 (B) and pH = 7.0 (C). Top spectra are experimental spectra. Middle and bottom ones are decomposed two components.

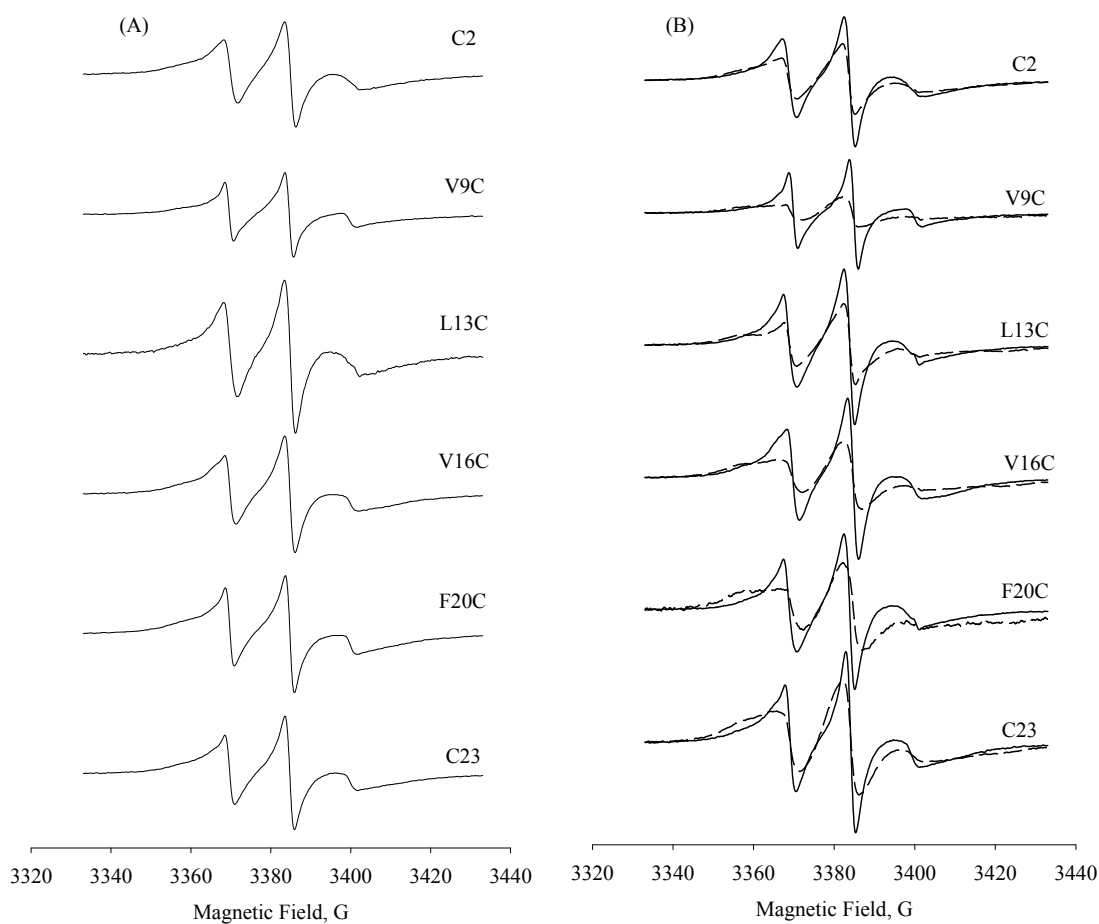


**Figure 4.4** Room temperature X-band (9.5 GHz) EPR spectra acquired from serious MTSL-CesA TMH5 mutant in DOPC bilayer at pH = 3.3. Labeled positions are indicated in the figure. Samples were purified by 3% (w/v) sucrose centrifugation as described in the Experiment. Spectra taken from samples without purification are shown in (A). Spectra acquired from two different layers, top (solid line) and bottom (dashed line) after separation are shown in (B).

EPR of doxyl-labeled phospholipids and stearic acids has long been used for studying the lipid-protein interface<sup>73, 120-121</sup> and dynamics of boundary lipids.<sup>122-123</sup> The boundary lipids are considered as a fraction of lipids immobilized by the protein; these lipids should fall into a slow motion, on the EPR time scale, regime and manifest themselves through appearance of broad components in the EPR spectra.<sup>120, 124-126</sup> In this study we employed 12-doxyl-PC (Figure 3.10) – a lipid spin-labeled at the position of acyl chain that is located within a 6 Å range from the center of the hydrophobic core of the lipid bilayer.<sup>127-128</sup> If the peptide acquires a transmembrane arrangement in the lipid bilayer, the EPR spectrum of a doxyl-PC lipid is expected to show the two populations corresponding to SL-lipids in the bulk lipid phase and the ones immobilized by the transmembrane fragment of the peptide, respectively.<sup>73</sup> If the peptide is not spanning the membrane but bound to or partitioned into the bilayer interface, the EPR spectra of the lipid with terminally spin-labeled acyl chains will show no changes. To increase the probability of the interaction of SL-lipids and the peptide, a total peptide-to-lipid ratio was brought to 1:25. Also, the sample was equilibrated with N<sub>2</sub> to eliminate the EPR line broadening caused by Heisenberg spin exchange between oxygen dissolved in the sample and the nitroxide. At room temperature in the presence of TMH5 there were no changes detected in the spectrum, most likely because the exchange rate between the two populations was too fast on the EPR time scale. At 11 °C a second, motionally restricted spectral component attributed to the fraction of the boundary lipids appeared in the EPR spectrum in the presence of TMH5 (Figure 4.5, (A)). This second component, although a rather weak, was more readily detected in the low-field region of the spectrum (low-field spectral component is shown enlarged in Figure 4.5, (B)).

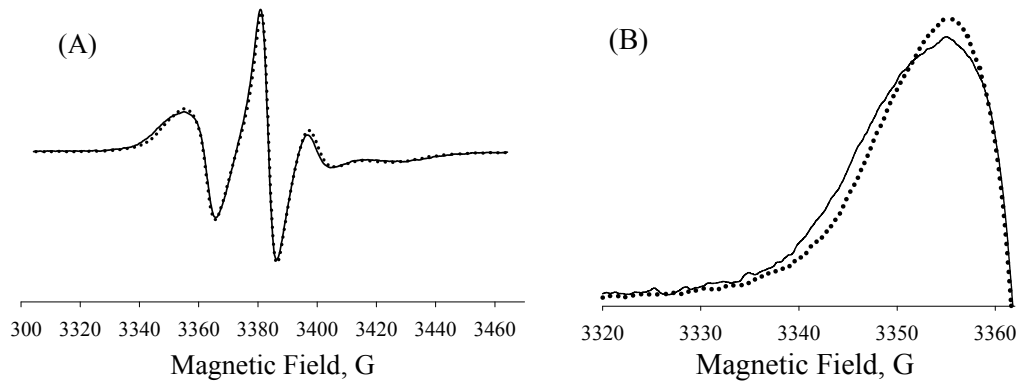


**Figure 4.5** (A) X-band (9.5 GHz) EPR spectra of  $N_2$ -equilibrated DOPC vesicles doped with 1 mol% of 12-doxyl-PC measured in the absence (dotted line) and presence (solid line) of CesA TMH5. (B) Zoom-in low field components of the same spectra. The spectra were taken at 11 °C. A total peptide-to-lipid ratio was 1:25. The samples were equilibrated at pH = 3.3. The spectra are normalized by spectral intensities.

The order parameter  $S$  (Equation 3.1) of the spin probe was calculated from the inner and outer hyperfine splittings of the experimental slow motion EPR spectra (Figure 4.5).<sup>98-100</sup>  $A_{\parallel}$  and  $A_{\perp}$  are a one half of the outer and inner hyperfine splittings, respectively.  $A_{\parallel}$  and  $A_{\perp}$  were measured to be 35.2 and 15.8 G for lipids without TMH5 and 35.7 and 15.7 G for immobilized lipids, respectively. The calculated order parameter for immobilized lipid component was slightly larger (0.491) than that for lipids without TMH5 (0.470). Although the trend how the order parameter changes indicates the presence of boundary lipids, it changes only little, which could be because 12-doxyl-PC in the pure lipid bilayer phase is already approached a slow motion regime and the spectral changes induced by TMH5 are not that pronounced. Thus, this experiment demonstrates that the acidic pH did not alter the

transmembrane arrangement of TMH5.

The membrane organization of a peptide could be ascertained by measuring the oxygen-induced EPR line width broadening of the nitroxides periodically attached along the peptide backbone. This broadening is caused by Heisenberg spin exchange interaction between the nitroxide and paramagnetic molecular oxygen. The relaxation rate of the nitroxide, and hence, the EPR line broadening, increase directly proportionally to oxygen concentration and oxygen diffusion coefficient.<sup>89</sup> In general, the permeation of oxygen into fluid lipid bilayer exhibits a profile inverse of that of the transmembrane polarity; however, it could be significantly affected by water penetration into the hydrophobic interior<sup>90</sup> as well as by the presence of transmembrane protein residues.<sup>37</sup> The latter is expected to be more important for the transmembrane helices containing polar amino acid residues.

We compared the EPR line width broadening caused by oxygen for different spin-labeled positions in CesaA TMH5 equilibrated at pH = 3.3 with that of TMH5 equilibrated at pH = 7.0. The oxygen accessibility experiments were also complemented with measurements of anisotropic nitrogen hyperfine coupling constant  $A_{zz}$  from the rigid-limit CW EPR spectra of SL-TMH5 reconstituted to DOPC bilayers. As it has already been pointed out, the magnitude of  $A_{zz}$  of the nitroxides could be a measure of the local polarity.<sup>101</sup> The oxygen accessibility and  $A_{zz}$  data for SL-TMH5 in different ionization states were compared with the corresponding data for the membrane-spanning non-aggregating WAPL23 peptide<sup>38</sup> in the vesicles of the same lipid composition. WAPL23 peptide has been recently introduced as a molecular ruler for studying the depth-dependent properties of the lipid bilayers.<sup>28</sup> The lipid-reconstituted TMH5 samples were separated by sucrose centrifugation

and only the top, enriched with  $\alpha$ -helical content layers, were used for these measurements.

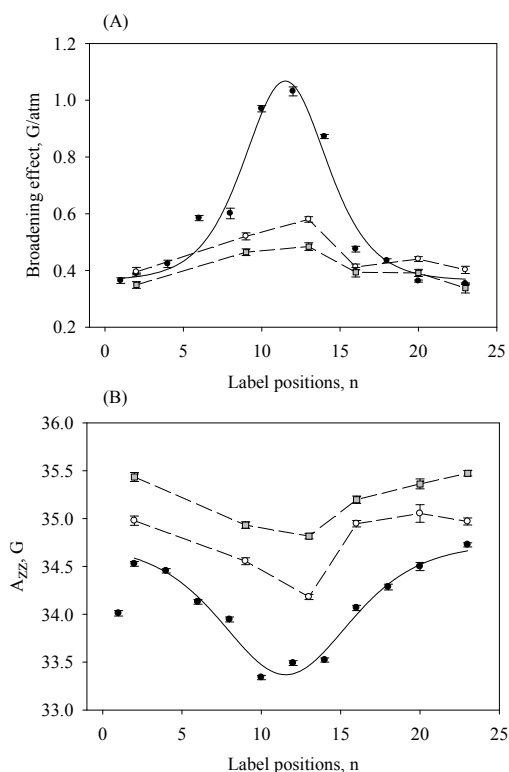


**Figure 4.6.** Line width broadening induced by oxygen and polarity profiles of TMH5 in DOPC vesicles at pH = 7.0 and pH = 3.0. (A): Oxygen induced EPR spectral line width broadening of MTSL-labeled WALP23 ( $\bullet$ ), TMH5 at pH = 7.0 ( $\blacksquare$ ), and TMH5 at pH = 3.3 ( $\circ$ ) reconstituted to DOPC vesicles shown as a function of the spin-labeling position. (B): Anisotropic nitrogen hyperfine splitting constant  $A_{zz}$  of MTSL-labeled WALP23 ( $\bullet$ ), TMH5 at pH = 7.0 ( $\bullet$ ), and TMH5 at pH = 3.3 ( $\circ$ ) reconstituted to DOPC vesicles shown as a function of the spin-labeling position. Solid lines are the least-squares fits of the experimental data to the Equation 2.3. The dashed lines connect the data points acquired for the SL-TMH5 samples and serve as guides for an eye.

The results of these measurements are summarized in Figure 4.6. For convenience, we will call TMH5 equilibrated at pH = 7.0 the “zwitterionic” and the one equilibrated at pH = 3.3 – the “positively charged”. Both the line width broadening ( $\Delta\Delta B_{pp}$ ) and  $A_{zz}$  data of the positively charged TMH5 showed the profiles similar to that of the zwitterionic one, although both profiles were significantly shallower than that of WALP23 peptide (Figure 4.6, (A)). However, the profiles of positively charged TMH5 were found to be more “hydrophobic”, with the magnitudes of the EPR line width broadening and  $A_{zz}$  moving towards that of WALP23 peptide. Thus, practically all labeled positions within the positively charged TMH5 variants showed increased EPR line width broadening effect (Figure 4.6, (B)) caused by oxygen with the largest effect observed for 13<sup>th</sup> position ( $\Delta\Delta B_{pp} = 0.58$  G/atm vs.  $\Delta\Delta B_{pp} = 0.484$  G/atm measured for the same position in the zwitterionic TMH5).  $\Delta\Delta B_{pp} = 0.58$  G is essentially the same line width broadening effect that is experienced by the spin labels in the 6<sup>th</sup> and 8<sup>th</sup> position of the reference WALP23 peptide ( $\Delta\Delta B_{pp} = 0.58$  and  $0.60$  G/atm, respectively, Figure 4.6, (A)). The membrane depth of this position corresponds to the region of C=C bonds of the DOPC lipids.<sup>28</sup> The exception is the position 16 – for this position only negligible  $\Delta\Delta B_{pp} = 0.019$  G was measured. The oxygen accessibility data are in line with the measurements of the anisotropic nitrogen hyperfine coupling constant  $A_{zz}$  from the rigid-limit CW EPR spectra. Thus, the positively charged TMH5 showed a significant ( $\approx 0.5$  G) decrease in the magnitude of  $A_{zz}$  that is an indication of more hydrophobic environment (Figure 4.6, (B)). The nitroxides in terminal positions still report on the more polar, compared to the corresponding positions in the WALP23 peptide, environment. However, the central 13<sup>th</sup> position ( $A_{zz} = 34.18$  G) is experiencing the local polarity similar to that

experienced by the nitroxides in the 6<sup>th</sup>, 16<sup>th</sup>, and 18<sup>th</sup> positions of the WALP23 peptide ( $A_{zz}$  = 34.13, 34.07, and 34.29 G, respectively). As we have already pointed out, the nitroxides in these positions are located within the region of C=C bonds of the DOPC lipid.<sup>28</sup> Interestingly, according to the  $A_{zz}$  data the effect of the pH was found to be the least, again, for the 16<sup>th</sup> position. Overall, the oxygen accessibility and  $A_{zz}$  data indicate that the spin-labeled sites in the positively charged TMH5 are located in more hydrophobic, than in the zwitterionic TMH5, environment. This could be interpreted as loosening of the TMH5 packing (partial disaggregation) induced by change in the peptides' ionization state; as a result, the spin-labeled sites are better exposed to the hydrophobic lipid phase enriched with oxygen. A most plausible explanation for the observed effect of the pH on the inter-helical interactions is as follows (Figure 4.7).

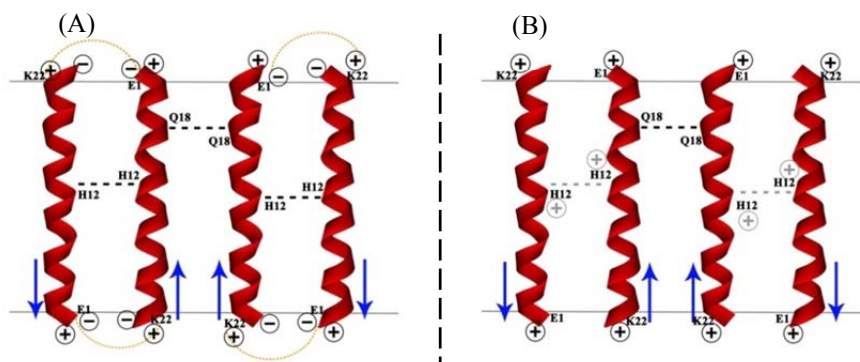


**Figure 4.7.** A cartoon illustrating the effect of pH (of the ionization state of the TMH5 helices) on the interhelical association. (A): pH = 7.0 (zwitterionic form); (B): pH = 3.3 (positively charged form). Blue arrows show the direction of the helical dipole (from C to N terminus). Orange dashed curves show the salt bridge between charged amino acids.

At pH = 7.0, in its zwitterionic form, the helix dipole-induced antiparallel oligomerization of the two TMH peptides is most likely assisted by a concurring strong electrostatic interaction between the negatively charged (Glu) N-terminus and positively charged (Lys) C-terminus. Additional stabilization of the helix oligomer could be provided by His residues located exactly in the center of the helix. As this residue is buried within the low dielectric bilayer core, its pK<sub>a</sub> is significantly diminished<sup>118</sup>, as a result, it is expected to exist in its neutral form and contributes to the interhelical interaction through hydrogen bonding. The patches of hydrophobic amino acid residues running along the peptide helix are most likely involved into Van der Waals packing interactions that further stabilize the helix oligomer. In theory, Ser side chain could also provide additional oligomer stabilization by making hydrogen bond to the backbone carbonyl of the complementary helix.<sup>129</sup> The amide group in the side chain of Gln18 is supposed to be involved into hydrogen bonding interaction with the Gln residue of the another pair of the TMH helices.<sup>79, 130</sup> We do not expect that the interfacial Gln2, which is obviously hydrogen-bond networked to bulk water, is participating in helix-to-helix interaction. We speculate, that a combination of these aforesaid forces puts considerable conformational strain on the  $\alpha$ -helix that is reflected in the relatively low  $\alpha$ -helical structure of the zwitterionic TMH5 as deduced from the CD spectra (Figure 4.1, dashed line). At acidic pH Glu is protonated and uncharged, so the electrostatic interaction in the antiparallel pair will be disrupted, that could also cause rearrangement/attenuation of hydrogen bonding and Van der Waals interactions, the conformational strain will be relieved, and the helices will regain their  $\alpha$ -helical content (Figure 4.1, solid line). No matter what the ionization state of TMH5 is, the Gln18 residue is

still involved into strong hydrogen-bonding interaction, which might explain why oxygen accessibility and anisotropic  $A_{zz}$  parameters for the nitroxide in the nearby 16<sup>th</sup> position would not change much at acidic pH (Figure 4.6). Unlike the 16<sup>th</sup> position, the 13<sup>th</sup> position, which is proximal to His12, is experiencing significant, both oxygen accessibility and local polarity, changes with the change of the ionization state. There could be at least two reasons for that. Firstly, the His side chain could be at least partial protonated at pH = 3.3 that would cause an electrostatic repulsion of like-charged species. Although it is unusual to assume that protons could be easily dragged into low-dielectric core of the lipid bilayer, it might be possible if the membrane integrity is compromised by the peptide aggregate (membrane is leaking).<sup>131-132</sup> Secondly, it could be a secondary effect, a rearrangement of His hydrogen bonding caused by loosening of the aggregate packing.

### 4.3 Conclusion

Our experiments clearly demonstrate that for the aggregated transmembrane helices such as TMH5 from the transmembrane domain of the plant cellulose synthase GhCesA1 from cotton, *Gossypium hirsutum*, the extent of aggregation, as well as the TMHs' secondary structure, could be changed by altering the peptides' ionization state, which implies at least partial involvement of the ionizable residues into the mechanism underlying the aggregation. Both CD and FTIR spectra of the membrane-embedded TMH5 showed a significant increase in the  $\alpha$ -helical content of TMH5 upon changing the pH from pH = 7.0 (zwitterionic state) to pH = 3.3 (positively charged state). EPR experiments with an acyl chain-spin labeled

phospholipid 12-doxyl-PC showed that the change in the ionization state would not alter the transmembrane arrangement of TMH5. EPR experiments with a series of TMH5 peptides systematically spin-labeled along the backbone demonstrated a significant change in the local environment of the labeled sites upon changing pH from pH = 7.0 to pH = 3.3. Thus, the oxygen accessibility and anisotropic nitrogen hyperfine coupling constant  $A_{zz}$  measurements showed that while positively charged TMH5 still remains partially aggregated, its local environment becomes more hydrophobic, which was attributed to a better exposure of the spin-labeled sites to a lipid interior. A residual aggregation of the positively charged TMH5 is supposed to be the result of Van der Waals packing interactions and strong hydrogen bonding interactions that involve His12, Glu1, Gln2 and Gln18. It cannot be excluded that the pH responsiveness of TMH5 (and of the other TMHs containing ionizable residues) also has a biological implication. For example, the change in the membrane arrangement and interaction with the neighboring  $\alpha$ -helices of TMH5 within the transmembrane domain of the plant cellulose synthase could be triggered by a local pH change (e.g., contact between ionizable site and a lumen of acidic organelle).

## Chapter 5 Helices disaggregation mediated by an extrinsic membrane-spanning non-aggregating $\alpha$ -helical peptide

### 5.1 Introduction

Membrane proteins are typically anchored to the lipid membrane by means of a transmembrane domain (TD) assembled as a result of lateral interactions between transmembrane helices. In many instances, TD is an essential part of a protein function. One of the examples is a polytopic transmembrane domain of the bacterial cellulose synthase from *Rhodobacter sphaeroids* (complex BcsA-BcsB). Recently solved crystal structure of this protein clearly showed that its TD is actively involved in translocation of growing glucan chain.<sup>19</sup> Membrane-spanning  $\alpha$ -helices are basically consist of hydrophobic amino acids, with polar and ionizable residues rarely found in their structures.<sup>103-105</sup> Although scarcely represented, polar amino acid residues are rather conserved in the structure of transmembrane helices (TMH), which is likely because of their importance for protein function,<sup>106-107</sup> folding, and stability.<sup>6</sup> The forces responsible for TD assembly and stabilization include interactions between helix dipoles<sup>115</sup> and ionizable residues<sup>111-112</sup>, hydrogen bonding<sup>108-109, 133</sup>, interhelical salt bridges<sup>134</sup>, and Van der Waals packing interactions.<sup>135-136</sup> Evidences collected so far strongly indicate that in the hydrophobic environment of the lipid bilayer intermolecular hydrogen bonding<sup>137</sup> between polar amino acid residues is particularly important for helix-to-helix association.<sup>108-109, 130, 138-140</sup> Thus, the ability of transmembrane helices to associate within the lipid bilayer is their intrinsic property. However, in some instances a combination of foresaid forces results in a strong aggregation of the helices,

which makes biophysical study of the individual TMHs rather challenging.

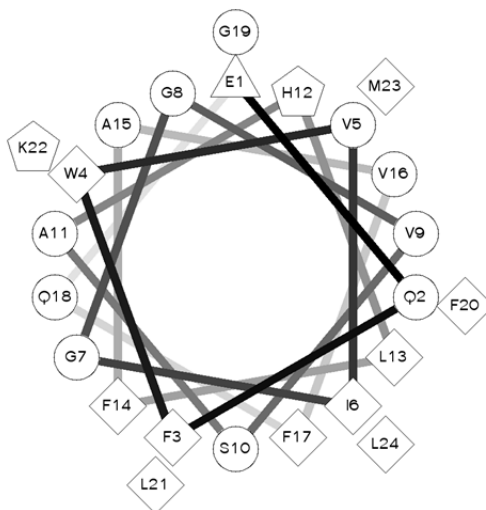


**Figure 5.1** Helical wheel of diagram of TMH5. Hydrophilic residues are shown as circles; hydrophobic residues are shown as diamonds; potentially negatively charged are shown as triangles, and potentially positively charged are shown as pentagons. The diagram is prepared using website by Don Armstrong and Raphael Zidovetzki<sup>141</sup>.

During our ongoing spin-labeling EPR studies on membrane arrangement of the individual transmembrane helices TMH4 and TMH5 from transmembrane domain of the plant cellulose synthase GhCesA1 from cotton, *Gossypium hirsutum*, we encountered a strong aggregation behavior of TMH5 inserted into the lipid bilayer (Chapter 3). CesA TMH5 peptide (EQFWVIGGVSAHLFAVFQGLKML, residues 817-840) contains, in addition to rather large patches of hydrophobic amino acids, several polar amino acid residues – the ionizable His in the center of the  $\alpha$ -helix and Glu and Lys in the flanking

position, as well as the hydrogen bonding Gln and Ser residues. Analysis of the helical wheel diagram of TMH5 (Figure 5.1) reveals a very interesting feature – it does not have clearly defined hydrophilic surface – the polar residues are point-embedded into the hydrophobic face of the peptide. We speculate that this is what makes TMH5 so prone to oligomerization. Typically, when incorporated into the lipid bilayer, the  $\alpha$ -helices assemble into aggregates with the hydrophobic residues facing the lipid phase and the polar residues buried in the interior of the aggregate so they are shielded from the hydrophobic environment.<sup>6</sup> Due to such an arrangement a hydrogen-bonding potential of the polar side chains is satisfied by hydrogen-bonding interaction with polar residues or backbones of other helices.<sup>142-144</sup> Moreover, the side chains of hydrogen-bonded polar residues have been shown to occupy smaller, than that of not hydrogen-bonded residues, volumes; this results in increased packing density and stronger van der Waals interactions.<sup>145</sup> For TMH5, practically three quarters of the peptide's surface has to be shielded from the hydrophobic environment of the bilayer by interaction with polar residues/backbone of the partner helix. Since the chance that all polar side chains of TMH5 will be facing the polar residues of other helices is rather small (for sterical reasons), in the peptide oligomer there always will be exposed polar residues waiting to be shielded.

As we recently found, an electrostatic interactions involving charged (at neutral pH) Glu and Lys side chains also seem to significantly contribute to the aggregation of TMH5. As we demonstrated, these interactions could be partially abolished by changing the ionization state of the Glu residue to neutral (Chapter 4).

We hypothesize that interhelical oligomerization of TMH5 could be attenuated, at

least partially, by separating TMH5 helices with a disaggregant – a membrane-spanning  $\alpha$ -helical non-aggregating peptide. In such an arrangement the TMH5-TMH5 hydrogen-bonding and electrostatic interactions are expected to be attenuated with weaker Van der Waals interactions between TMH5 and a disaggregant. We believe that this practical biophysical strategy would allow the aggregating peptides to be studied in their individual form and fundamentally contribute to our understanding of the mechanisms governing the helices insertion, arrangement of membrane-inserted helices, and interhelical interactions.

To probe the TMH-disaggregant interactions we employed spin-labeling EPR spectroscopy, which is one of the most powerful techniques allowing for interrogating the structure and dynamics of peptide and protein systems; this molecular probe-based technique has proven to be especially useful in determination of membrane proteins structure.<sup>57-58</sup> The technique is based on the analysis of a spectrum from the paramagnetic tag covalently attached to artificially created site within the structure of peptide or protein, typically, the SH-group of cysteine, introduced either during the solid phase peptide synthesis (SPPS) or through the site-directed mutagenesis.<sup>15, 28-29, 31</sup> The method allows for probing the molecular dynamics of the spin-labeled sites in membrane-associated proteins or peptides under native conditions over a wide range of motions (generally, from ps to ms).<sup>32, 59</sup>

As a disaggregant, we used a variant of an  $\alpha$ -helical membrane-spanning non-aggregating WALP23-C8 peptide (GWWLALAMALALALALALWWA) that was available to us. WALP23 peptide has been recently introduced as a molecular ruler for studying the depth-dependent properties of the lipid bilayers.<sup>28</sup>

Herein we report on our site-directed spin-labeling (SDSL) EPR studies aimed to

reveal the effect of a disaggregant – a membrane-spanning  $\alpha$ -helical non-aggregating WALP23 peptide, on the oligomerization of TMH5 from the transmembrane domain of GhCesA1 from cotton, *Gossypium hirsutum*. In this study, we were using a library of 24-mer TMH5 model peptides chemically synthesized through SPPS. We employed a methanethiosulfonate chemistry to tether a paramagnetic tag – a nitroxide – to the thiol groups of cysteines strategically positioned within the hydrophobic patches of TMH5. These cysteines were introduced into a TMH sequence through replacement of selected amino acids in the hydrophobic patches of the peptides during the SPPS synthesis. A thiol-specific nitroxide methanethiosulfonic acid S-(1-oxyl-2,2,5,5-tetramethyl-2,5-dihydro-1*H*-pyrrol-3-ylmethyl) ester (MTSL) was used as a spin label. We carried out the molecular accessibility and the rigid-limit X-band (9.5 GHz) EPR measurements to determine the effect of WALP23 peptide on the arrangement of WALP23-diluted spin-labeled TMH5 (SL-TMH5) within the lipid bilayer. In order to find out whether TMH5-WALP23 assembly alters the lipid bilayer permeability, we carried out a kinetic study on the nitroxide reduction with ascorbic acid/ascorbate. X-band spin-labeling EPR experiments were followed with Rosetta prediction of contacts and packing of SL-labeled TMH5 and WALP23-C8 peptides.

## **5.2 Results and discussion**

EPR spectra of nitroxides are exceptionally sensitive to the rotational dynamics of the protein side chain.<sup>16, 73</sup> Restriction of rotational mobility of the nitroxide manifests itself in significant spectral changes, e.g., spectral broadening.<sup>16, 29</sup> Thus, the event of aggregation of

spin-labeled peptides/proteins could be deduced from appearance of additional broad components in the EPR spectra.<sup>75-76</sup> Typically, the aggregated component appears as a broad shoulder in the low-field part of the EPR spectrum. Fitting of multicomponent EPR spectra allows to obtain the dynamic parameters describing the motion of each component as well as the relative population of each component.<sup>146</sup> The association of the spin-labeled helices could also be followed by measuring the inverse linewidth of the central resonance component from the spectrum of a nitroxide – this method is conventionally used to qualitatively describe the mobility of the labeled site.<sup>16</sup> Another approach that allows for obtaining the structural information about the peptide side chains even without knowing peptide's structure at atomic level involves measuring of the molecular accessibility of the spin-labeled site ( $T_2$  method).<sup>15, 28-29, 32, 36</sup> In the accessibility measurement the EPR line broadening reagents such as paramagnetic metal ion complexes, molecular oxygen, or another nitroxide, are typically employed.<sup>32</sup> The line broadening is caused by Heisenberg spin exchange interaction between the nitroxide and paramagnetic broadening agent. The relaxation rate of the nitroxide, and hence, the EPR line broadening, increase directly proportionally to concentration and diffusion coefficient of the paramagnetic broadening agent, e.g., molecular oxygen.<sup>89</sup> Thus, the solvent-exposed spin-labeled sites would demonstrate the highest molecular accessibility.<sup>32</sup> Measuring oxygen permeability in lipid bilayers allows to assess the relative insertion depth of the labeled site in the membrane.<sup>36</sup>

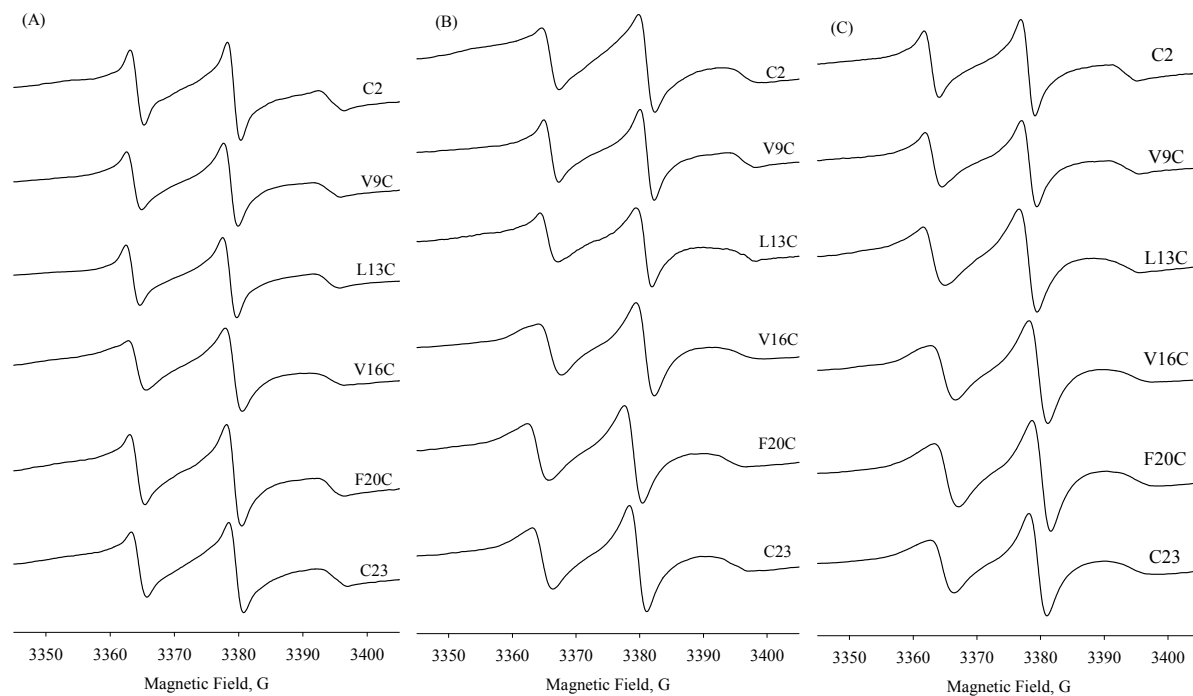
The native transmembrane helix TMH5 from the transmembrane domain of the plant cellulose synthase GhCesA1 from cotton, *Gossypium hirsutum*, as well as its variants with the selected amino acids in the hydrophobic face of the peptide single point-mutated to

cysteines, were synthesized through solid phase peptide synthesis (SPPS) (Table 2.2). Cysteines were strategically positioned within the hydrophobic patches along the peptide backbone to (i) continuously probe the environment along the peptide backbone and (ii) not to interfere with the polar residues that are expected to participate in the inter-helical association. The side chain of cysteine was used to covalently attach a thiol-specific methanethiosulfonate nitroxide methanethiosulfonic acid S-(1-oxy-2,2,5,5-tetramethyl-2,5-dihydro-1*H*-pyrrol-3-ylmethyl) ester (MTSL, Figure 1.1 spin label III). The one-letter sequences of the peptides used in this study and corresponding codes are given in Table 2.2.

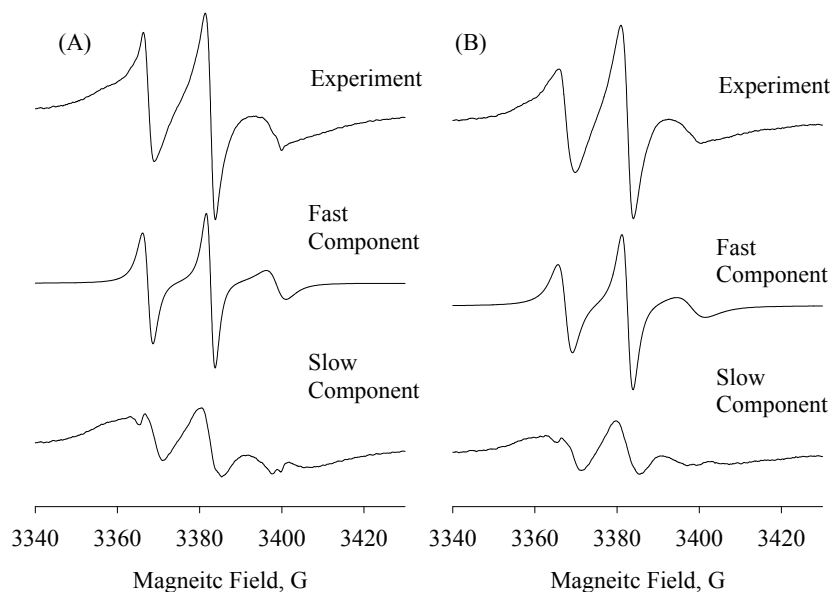
Spin-labeled TMH5 (SL-TMH5) variants were membrane co-inserted with WALP23 L8S peptide in 1:3 molar ratio by mixing TFE solution of TMH5 and WALP23 L8S with a chloroform solution of DOPC lipids, removing the solvents, and rehydrating the residue with a buffer solution through several consecutive freeze-thaw cycles. To use the advantage of our recent finding of the pH effect (peptide's ionization state) on the aggregation state of TMH5, we rehydrated lipids with buffer solutions both at pH = 7.0 and pH = 3.3. We subjected the TMH5-WALP samples to sucrose centrifugation, similar to described in the Chapter 3. However, the separation yielded only a negligible amount of the aggregated peptide, which allowed us to conclude that using WALP23 as a disaggregant improves TMH5 insertion.

Figure 5.2 shows a series of X-band (9.5 GHz) EPR spectra of SL-labeled TMH5 variants and WALP23 L8S peptide co-inserted in DOPC membrane at 1:3 molar ratio and, for comparison, the spectra of SL-TMH5 in DOPC vesicles. Although the spectra from homonymous peptides rehydrated under different condition (with or without disaggregant, at

pH = 7.0 or pH = 3.3) look essentially the same, it is seen that the spectra from the column C exhibit the lowest content of the broad low-field component. Spectral decomposition<sup>77</sup> of SL-TMH5 L13C mutant in DOPC without or with co-insertion with WALP23 L8S peptide into DOPC membrane demonstrates that the population of the aggregated composition decreased from 94% to 90% at pH = 7.0 (Figure 5.3 (A)), and 87% to 73 at pH = 3.3 (Figure 5.3 (B)) at central position of TMH5. It is worthy of noticing that the spectra collected from the variants L13C and C2 equilibrated at pH = 7.0 seem to stand out of line. Thus, the spectrum of TMH C2 shows a significant population of the broad (aggregated) component. We attribute this aggregation to electrostatic interaction between the Glu and Lys side chains that are ionized at neutral pH. When helices are oligomerized in an antiparallel fashion, the electrostatic attraction of these residues could significantly restrict the mobility of C2 spin-labeled site even in the presence of WALP23 peptide. The spin labels in other positions seem to be less sensitive to the electrostatic interaction of the terminal residues. Interestingly, the spin label at C23 site did not show a similar broadening; or, at least, the population of the aggregated form was significantly lower. We are speculating that this is because in TMH5 C23 sequence, unlike in TMH5 C2, the Glu and Lys residues are moved further away from each other, thus decreasing the electrostatic attraction between the charged side chains. The sharp peak appeared in the spectrum of L13C variant at pH = 7.0 could be from the unreacted spin label that was not completely washed out from the sample. Most likely, that at pH = 3.3 this component was masked by overlapping with a much stronger spectrum of the labeled peptide.



**Figure 5.2** Series of X-band (9.5 GHz) EPR spectra acquired from nitrogen-equilibrated TMH5 spin-labeled at various positions (A) in DOPC vesicles equilibrated at pH = 7.0 (top layer obtained after sucrose separation); (B) in DOPC vesicles co-inserted with WALPL23 L8S peptide at pH = 7.0; (C) in DOPC vesicles co-inserted with WALP23 L8S peptide at pH = 3.3. The samples and the cavity of the EPR spectrometer were equilibrated at 21.5 °C.



**Figure 5.3** Decompositions of series of X-band (9.5 GHz) EPR spectra acquired from a spin-labeled TMH5 L13C mutant co-inserted with WALPL8S peptide in DOPC lipids hydrated with buffer solutions at pH = 3.3 (A), and pH = 7.0 (B). Top spectra are experimental spectra. Middle and bottom ones are decomposed two components.

To characterize the effect of the co-insertion with WALP23 L8S on mobility of the spin-labeled side chains in SL-TMH5, we measured a peak-to-peak line width of the central spectral component from the experimental X-band EPR spectra and plotted its reciprocal ( $\Delta H(0)_{p-p}^{-1}$ ) vs. labeling position (Figure 5.4, (A)). For comparison, the corresponding data for TMH5 without co-inserted WALP23 are also shown. The lower  $\Delta H(0)_{p-p}^{-1}$  values correspond to the higher  $\Delta H(0)_{p-p}$  and, hence, report on a more restricted motion. The calculated  $\Delta H(0)_{p-p}^{-1}$  values of for TMH5 change between 0.33 and 0.5  $G^{-1}$ , thus falling into

the mobility range characteristic for labels residing at the helix surface and in the loop region of proteins, i.e., all the labeled sites are somewhat restricted in motion.<sup>16</sup> The following general trends can be drawn from these data. (i) *The N-termini were found generally to be more mobile than the corresponding C-termini; this is true both for neutral and acidic pH.* This is most likely because the spin label at N-terminus (C2 sequence, Table 1) is located slightly above the bilayer interface<sup>20</sup> and exposed to bulk aqueous phase. (ii) *At acidic pH the N-terminus, both with and without WALP peptide co-inserted, is more restricted in motion than that at neutral pH without WALP23. However, co-insertion with WALP peptide at neutral pH significantly restricts N-terminus of SL-TMH5 in motion.* A possible explanation for this is as follows. At neutral pH without WALP co-inserted TMH5 exhibits very low (11.6% see Chapter 3)  $\alpha$ -helical content and its terminus exposed to bulk aqueous phase could behave as a relatively unrestricted fragment of a disordered peptide. When co-inserted with WALP peptide, N-terminus of TMH might experience sterical hindrance from the terminals of the former that are motionally restricted in the DOPC membrane.<sup>28</sup> Moreover, although a rather speculative, there is a possibility that terminal carboxylate of TMH5 is involved into hydrogen bonding with the Trp residues of the proximal WALP helices.<sup>147-151</sup> Lastly, but not leastly, the interaction with WALP23 might induce the  $\alpha$ -helical structure formation in TMH5 so the helix's rigidity imposed additional motional restrictions on the N-terminus. At acidic pH without WALP co-inserted, the terminal carboxylic group could be hydrogen-bonded to the carboxylic group of other helix; this interaction is expected to be less effective when TMH5 is co-inserted with WALP23. (iii) *At acidic pH the C-terminus is slightly less mobile than that at neutral pH, no matter was or was not WALP23 present.* The

most reasonable explanation is that in the oligomer at acidic pH the free carboxylic group of uncapped C-terminus is hydrogen-bonded to the carboxylic group of the Glu side chain of antiparallely packed partner helix. (iv) *C-terminus of the TMH5 co-inserted with WALP is less mobile than that without WALP peptide at both pH values.* When co-inserted with WALP peptide, C-terminus of TMH5 might experience sterical hindrance from the motionally restricted in the DOPC membrane terminals of the former.<sup>28</sup> Moreover, the interaction with WALP23 might increase the  $\alpha$ -helical content in TMH5 so the helix's rigidity imposed additional motional restrictions on the C-terminus.

Since the dipolar interactions induced between adjacent spin-labeled sites in the aggregate result in spectral broadening that reduces intensities of the EPR spectral lines, the change in the amplitude of the central spectral component is a good illustration on how the pH effects the peptide's aggregation state (Figure 5.4(B)).<sup>29</sup> A parameter Amp. (0)% is a ratio of the amplitudes of the central spectral components of the normalized spectra taken at pH = 7.0 and pH = 3.3, respectively, for the same labeling position. As it is shown in Figure 5.4 (B), Amp. (0)% values are all smaller than unity, indicating a lower level of peptide oligomerization at pH = 3.3. Note that for the C-terminus the Amp. (0)% is reduced much stronger than that for the N-terminus, thus illustrating that C-terminus is tighter packed, and, hence, more restricted in motion at neutral pH. This is in line with the peak-to-peak central line width measurements (Figure 5.4 (A), and discussion above).

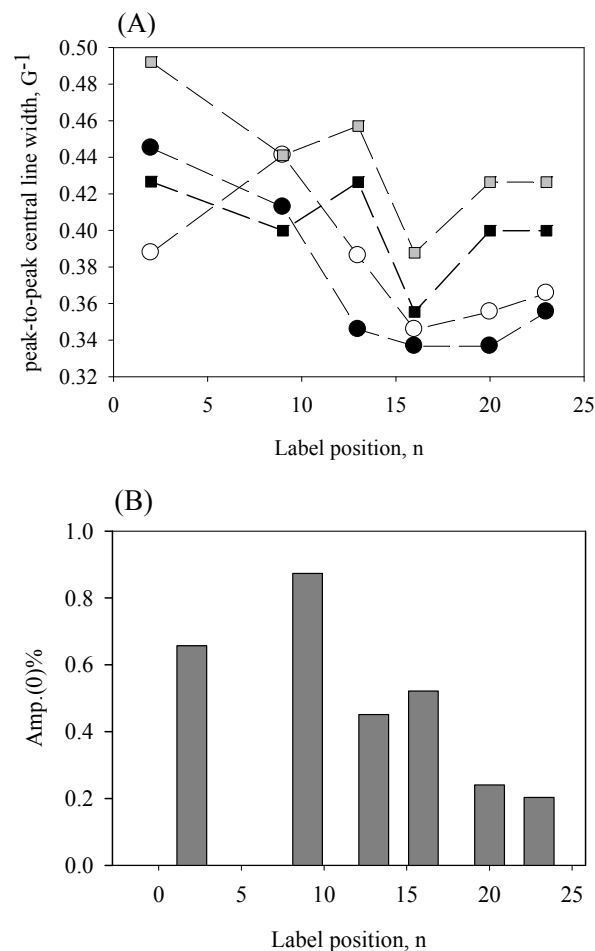


**Figure 5.4** (A):  $\Delta H(0)_{p-p}^{-1}$  versus the label position in TMH5 co-inserted with WALP23 L8S peptide at pH = 7.0 (○) and pH = 3.3 (●) in DOPC vesicles. A comparison of SL-TMH5 embedded into DOPC bilayer without WALP23 L8S co-insertion pH = 7.0 (□) and pH = 3.3 (■) is shown. (B): Amplitude of central component versus the label position in TMH5 co-inserted with WALP23 L8S peptide in DOPC vesicles. The spectra were taken at 21.5 °C and equilibrated with  $N_2$ . Amp (0) % is the ratio between the amplitude of central component measured from spectra taken at pH = 7.0 and pH = 3.3 for the same labeling position. Original EPR spectra were normalized to the same concentration of spins.

Oxygen permeability to the spin-labeled sites in SL-TMH5 peptides co-inserted with WALP23 L8S into DOPC bilayers - a  $T_2$  method.

To characterize the effect of TMH5 co-insertion with WALP23 peptide, we also measured oxygen permeability to the spin-labeled sites of the TMH ( $T_2$  method). To do so, we measured a homogeneous (Lorentzian) EPR line width broadening as a function of oxygen pressure.<sup>36</sup> The homogeneous line width broadening  $\Delta\Delta B_{p-p}^L$  for SL- TMH5 L13C co-inserted with WALPL8S in DOPC vesicles shows a broadening effect of 0.54 G/atm at pH = 7.0, and under the same conditions the homogeneous line width broadening effect measured for TMH5 L13C without present of WALP23 L8S (top layer separated from sucrose purification as described in Chapter 2) decreased to 0.48 G/atm at pH = 7.0. Although the effect is not quite pronounced (about 13% line width increase), but the co-insertion with WALP23 causes a rather noticeable line broadening effect, which could be interpreted as a partial disaggregation of TMH5 peptide.

The homogeneous line width broadening  $\Delta\Delta B_{p-p}^L$  for SL-TMHs co-inserted with WALP23 L8S in DOPC lipids plotted against the labeling position,  $n$ , along with the corresponding data for SL-WALP23 variants in the vesicles of the same lipid composition, is shown in Figure 5.5.

A  $\Delta\Delta B_{p-p}^L$  vs. labeling position plot for membrane-spanning non-aggregating SL-WALP23 peptide in DOPC bilayer<sup>28</sup> has a bell-like shape that fits rather well to the Equation 2.3 (Figure 5.5). When WALP23 is embedded in shorter DLPC lipids, under the hydrophobic mismatch condition, the peptide loses its ideal  $\alpha$ -helical structure and oligomerize as it has been proven by fluorescence measurements, although the

oligomerization is not extensive.<sup>115</sup> As it could be seen from Figure 5.5, the event of oligomerization is explicitly demonstrated by the change in the  $\Delta\Delta B_{p-p}^L$  vs.  $n$  plot. Note that  $\Delta\Delta B_{p-p}^L$  data for SL-WALP23 in DLPC could be fit to Equation 2.3 only if the line width broadening data for the spin labels in positions 1, 4, 8, and 23 were omitted. Thus,  $T_2$  method is a sensitive tool to follow the peptide oligomerization. The oxygen accessibility of SL- TMH5 peptide co-inserted with three-fold excess of WALP23 L8S in the DOPC bilayer both at pH = 3.3 and pH = 7.0 somewhat follows the trend shown by SL-WALP23 peptide; however, the line broadening effect is much less pronounced (Figure 5.5). Two features are worthy of mentioning. Firstly, the oxygen accessibility to the nitroxide at neutral pH in general is slightly lower compared to that at acidic condition, which indicates a more tight packing of the TMH helices at neutral pH. Secondly, the line width broadening for the nitroxide at 16<sup>th</sup> position is abnormally low and essentially the same at both pH values. This observation indicates that the helices packing at this position is much tighter than that in the nearby positions and independent on the ionization state of the side chain groups. The most likely reason for that is the proximity of the Gln18 residue; the amide group of the Gln side chain is not ionizable, but is capable for strong interhelical hydrogen-bonding interactions<sup>79, 130</sup>. These results are in line with that obtained from the measuring the mobility of the spin-labeled sites (see the discussion above).

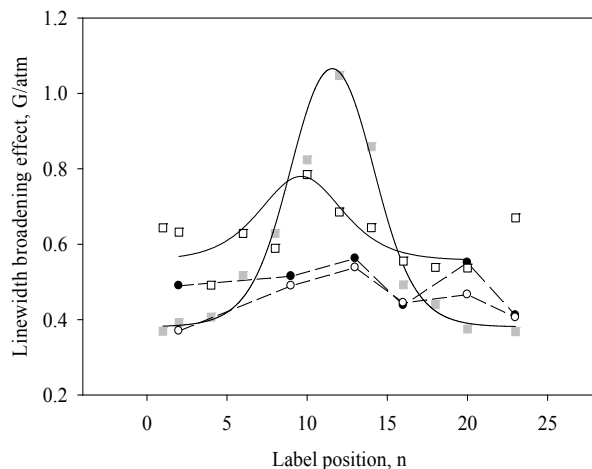


**Figure 5.5** Overlapped  $\Delta\Delta B^L_{p-p}$  vs. labeling position plots for SL-TMH5 co-inserted with 3 fold molar excess of WALP23 L8S in DOPC vesicles at pH = 3.3 (●) and pH = 7.0 (○), SL-WALP23 in DOPC (■) and DLPC (□) vesicles. Solid lines are the least-squares fits of the experimental data to the Equation 2.3. The dashed lines connect the data points acquired for the SL-TMH5 samples and serve as guides for an eye.

Local polarity along the backbone of the Cesa TMH peptides co-inserted with WALP23 L8S peptide in DOPC bilayers: measuring anisotropic nitrogen hyperfine coupling constant  $A_{zz}$  from the rigid-limit (77K) X-band EPR spectra.

The information on the insertion pattern of transmembrane helices could be gathered by measuring anisotropic nitrogen hyperfine coupling constant  $A_{zz}$  from the rigid-limit (77K) EPR spectra for individual spin-labeled positions along the peptide; the  $A_{zz}$  parameter has been shown to be very sensitive to the polarity of the local environment.<sup>101</sup> The z component of the anisotropic hyperfine coupling constant was measured from the least-squares simulation of the high- and low-field components of the rigid-limit X-band EPR spectra

obtained from the lipid-embedded TMH samples freeze-quenched in liquid nitrogen (77K). The rigid-limit spectra obtained from the spin-labeled TMH5 L13C co-inserted with three-fold excess of WALP23 L8S in DOPC bilayers at pH = 3.3 and 7.0, respectively, are shown in Figure 5.6. The amplitude of the spectrum taken at neutral pH is significantly smaller due to the stronger dipolar interactions between the proximate spin-labeled sites caused by tighter peptide packing in the aggregation.

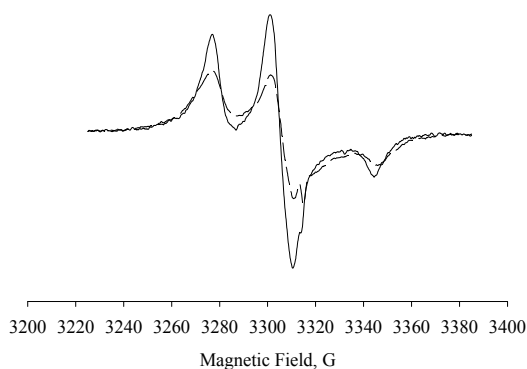


**Figure 5.6** Rigid-limit (77K) CW X-band EPR spectra of SL-TMH5 L13C co-inserted with three-fold excess of WALP23 L8S peptide in DOPC bilayers at pH = 3.3 (solid line) and pH = 7.0 (dashed line). Spectra were normalized by double integration to the same spin concentration.

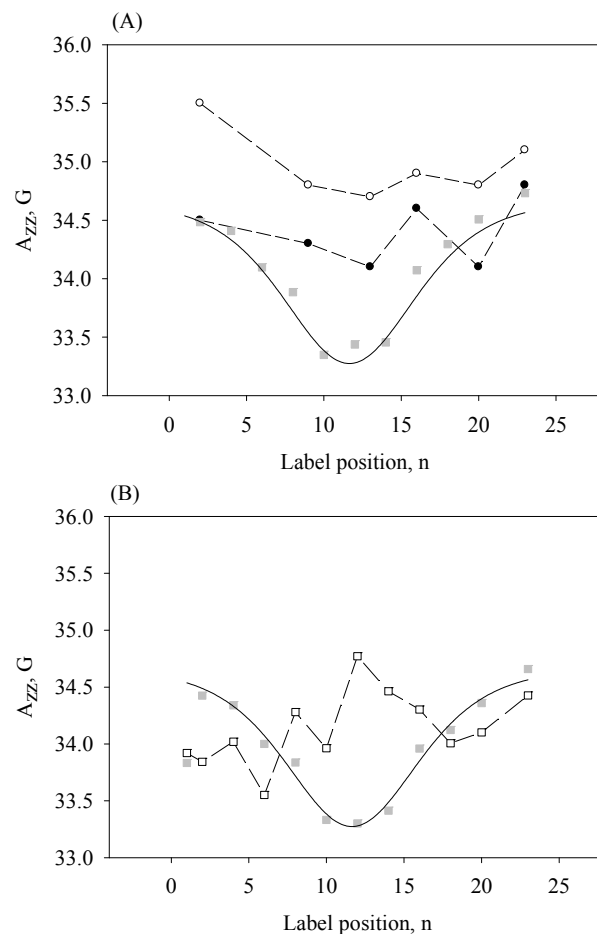


**Figure 5.7** (A): Anisotropic nitrogen hyperfine coupling constants  $A_{zz}$  acquired from X-band CW EPR of MTSL-labeled TMH5 peptides co-inserted with three-fold excess of WALP23 L8S peptide in DOPC bilayers at pH = 3.3 (●) and pH = 7.0 (○) and MTSL-labeled WALP23 peptides in DOPC (■) vesicles (pH = 7.0). (B): Anisotropic  $A_{zz}$  coupling constants for MTSL-labeled WALP23 in DOPC (■) and DLPC (□) bilayers. Solid lines are the least-squares fits of the experimental data to the Equation 2.3. The dashed lines connecting the data points serve as guides for an eye.

$A_{zz}$  profiles for SL-TMH5 co-inserted with WALP23 L8S in DOPC bilayers at pH = 3.3 and pH = 7.0 (A) as well as for SL-WALP23 in DLPC bilayers at pH = 7.0 (B) is shown in Figure 5.7. The SL-WALP23 embedded in DOPC membrane is shown as a reference and its polarity profile exhibits a characteristic bell-like profile with the residues at the water-lipid bilayer interface showing large  $A_{zz}$  splittings of about 34.5 G (polar environment) that are gradually decreasing towards the center of the bilayer hydrophobic core (apolar environment). However, the same peptide in shorter DLPC bilayer did not show a distinctive  $A_{zz}$  profile thus indicating a distortion of the  $\alpha$ -helix and/or peptide oligomerization caused by the hydrophobic mismatch<sup>71, 115, 152</sup>.

The SL-TMH5/WALP23 L8S samples in DOPC rehydrated at neutral and acidic pH demonstrate similar  $A_{zz}$  profiles; however, the acidic profile is more “hydrophobic”. The nitrogen hyperfine coupling constant profile shows  $A_{zz}$  for the terminal positions 2 and 23 in SL-TMH5/WALP23 L8S at pH = 7.0 of about  $A_{zz} \approx 35.5$  and 35.1 G, respectively; the corresponding spin-labeled positions in the SL-WALP23 peptide experience less polar environment characterized by  $A_{zz}$  value of approximately 1.0 G lower ( $A_{zz} \approx 34.5$  G). The  $A_{zz}$  parameters for the same positions at pH = 3.3 are shifted to a less polar region and are close to  $A_{zz}$  for the corresponding positions of SL-WALP23 ( $A_{zz} \approx 34.5$  G for the 2<sup>nd</sup> position and  $A_{zz} \approx 34.8$  G for the 23<sup>rd</sup> position). The positions of the SL-TMH5/WALP23 L8S corresponding to the center of the lipid bilayer yield much polar  $A_{zz} \approx 34.1$  G (pH = 3.3) and  $A_{zz} \approx 34.7$  G (pH = 7.0) vs.  $A_{zz} \approx 33.3$  G for the SL-WALP23 (Figure 5.7 (A)). These data clearly demonstrate that co-insertion with WALP23 L8S at pH = 3.3 cause a rather noticeable disaggregation of the TMH5 peptide. In the aggregated state, a significant fraction of the

nitroxides is supposed to be buried amongst the tightly packed peptide chains and is not exposed towards the lipid phase. For such buried nitroxides at pH = 7.0,  $A_{zz}$  values report basically on the polar environment of the peptide backbone. For TMH5 co-inserted with WALP23 L8S peptide at pH = 3.3, the probability of the spin-labeled sites to face the lipid phase is increasing, which is reflected in lower  $A_{zz}$  values. Even if the observed ranges of  $A_{zz}$  variations for TMH5 (34.7–35.5 G, pH = 7.0 and 34.1–34.8 G, pH = 3.3) fall into the  $A_{zz}$  range that is significantly more polar compared to that of the SL-WALP23 (33.3–34.8 G), it is still less polar than  $A_{zz}$  of MTSL label in frozen aqueous solution, which has been reported to be  $A_{zz} = 36.5$  G.<sup>91</sup> The latter fact indicates that the nitroxide moieties in SL-TMH5/WALP23 L8S are far from being exposed to the bulk aqueous phase. Furthermore, such high  $A_{zz}$  values for MTSL-labeled buried sites in membrane proteins have already been reported in the literature. For example, in bacteriorhodopsin, the MTSL-labeled residues T170C (terminus of helix F, oriented towards helix G) and L100C (terminus of helix C) located in the interior of the protein, yielded a rather high  $A_{zz}$  values of about  $A_{zz} \approx 35.9$  G and  $A_{zz} \approx 35.5$  G, respectively. Such high magnitudes of  $A_{zz}$  were interpreted in terms of polar interaction with the proximal  $\alpha$ -helices.<sup>91</sup> The polarity within the aggregate could also increase owing to water molecules drawn by TMH to the hydrophobic interior of the bilayer.<sup>92-96</sup> Thus, we believe that the anisotropic  $A_{zz}$  parameters from the rigid-limit EPR spectra of SL-TMH5/WALP23 L8S most likely report on the polarity of hydrated interior of the aggregate peptide. An abnormally high  $A_{zz}$  splitting observed for the nitroxide at position 16 is consistent with the results of oxygen accessibility experiments and the measurements of the mobility of the spin-labeled sites (see the discussion above).

### Solvent Accessibility of Spin Label in SL-TMH: Reduction with Ascorbic Acid

One of the methods that allow determining the location of protein's spin-labeled sites and protein topography in the lipid membrane is the nitroxide reaction with ascorbic acid. As a result, a nitroxide is reduced into EPR-silent hydroxylamine and the EPR signal amplitude gradually decreases<sup>153</sup>. The rate of the nitroxide reduction is determined by conditions near the labeled site; therefore, measurement of the reduction kinetics allows differentiating the spin-labeled sites with different solvent accessibility or environment. For the labeled sites in the transmembrane location the reduction rate depends on the depth at which the label is located in the bilayer<sup>154</sup>. Reduction of the nitroxide buried in the lipid membrane was shown to obey the first order rate law at physiological pH<sup>153</sup>. The order of this reaction is complicated by several other factors, such as chemical composition of the membrane, pH, and temperature. In its electrically neutral form (at pH below the  $pK_{a1} = 4.1$ ), ascorbic acid diffuses into membrane much faster than its charged, anionic form. Thus, we employed the nitroxide reduction kinetics measurements to elucidate the location of the spin-labeled sites of SL-TMH5 within the membrane and extent of its aggregation. All the reduction experiments were carried out on 100 nm unilamellar vesicles (ULV) at the same controlled temperature under continuous  $N_2$  flow (see Chapter 2).

First, we measured the kinetics of the nitroxide reduction using MTSL-labeled  $\alpha$ -helical membrane-spanning non-aggregating WALP23 peptide as a reference. The reduction was carried out at  $pH \approx 7.0$  and  $pH \approx 3.3$ , which is above (anionic form) and below (electrically neutral form) of the  $pK_a$  of ascorbic acid ( $pK_{a1} = 4.1$ ), respectively.

Figure 5.8 (A) shows the two overlaid EPR spectra of MTSL-labeled WALP-C23

variant incorporated into DOPC bilayers at pH = 7.0 immediately after addition of ascorbic acid (solid line) and after 3 h incubation at 21.5 °C under continuous N<sub>2</sub> flow (dashed line). Since there is no dipolar interaction (broadening) for membrane spanning WALP23 embedded in DOPC membrane<sup>28</sup>, the EPR signal intensity is directly proportional to the concentration of the nitroxide. Figure 5.8 (B) shows the intensities of the central EPR component plotted against reaction time for the reduction of MTSL-labeled WALP-C23 (SL-WALP23) and WALP-C16 variants, respectively. The kinetic decay curves were fitted with a single exponential equation (shown as solid lines)<sup>154</sup>:

$$Y = Y_0 + Ae^{-kt} \quad \text{Equation 5.1}$$

where  $I_{p-p}(0)$  is the peak to peak intensity of the central component,  $I_0$  is the maximum intensity of the center field peak when time  $t$  starts,  $A$  is the coefficients, and  $k$  represent the corresponding reduction rate constant.

The kinetic data for reduction of the nitroxides attached at positions 23, 16 or 12 of WALP23 peptide embedded in DOPC bilayers at neutral pH (Figure 5.8) are summarized in Table 3. The immersion depth of the labeled site in the membrane changes in the order 23 < 16 < 12, with the nitroxide at the 23<sup>rd</sup> position residing at the bilayer interface (exposed to bulk water) and the nitroxide at the 12<sup>th</sup> position located in the center of the hydrophobic core of the lipid bilayer<sup>28</sup>. The reduction rate of SL-WALP-C23 is more than two-fold higher compared to SL-WALP-C16 (see Table 5.1), and the nitroxide at 12<sup>th</sup> position is practically inaccessible to the reducing agent. The reduction of SL-WALP-C12 is only about 5%, and reduction rate was not calculated.

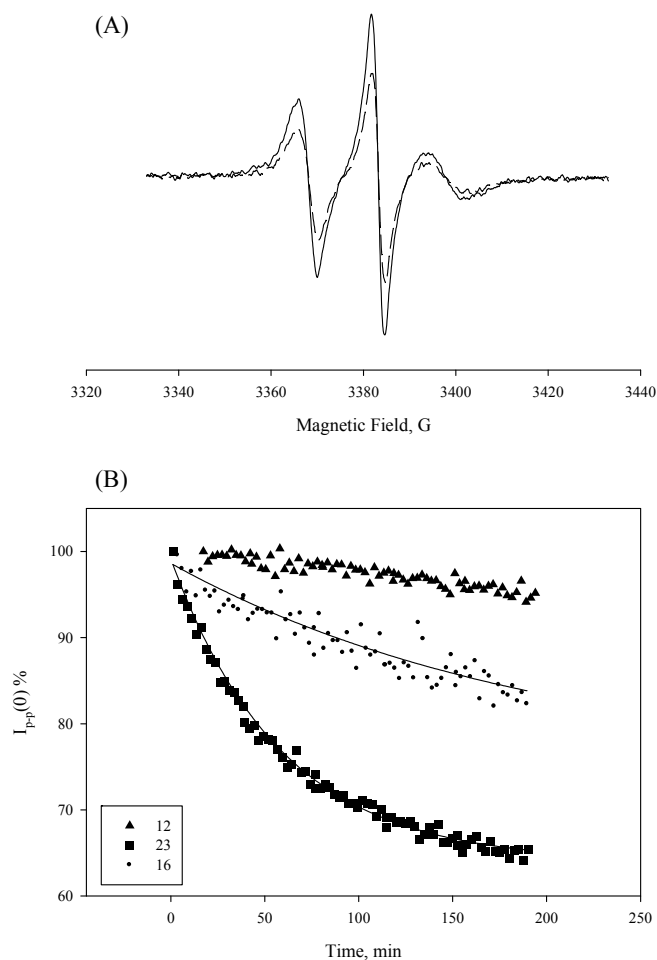


**Figure 5.8.** Spin label reduction with ascorbic acid experiment with continuous  $N_2$  flow. (A): an overlap of X-band (9.5 GHz) EPR spectra acquired from MTSL-labeled WALP-C12 in DOPC vesicles at pH = 6.8 (21.5 °C) treated with ascorbic acid: solid line - 1 min after addition of ascorbic acid; dashed line - in 190 min. (B): Central EPR spectral component intensity decay for MTSL-labeled WALP23 peptides in DOPC induced by five-fold molar excess of ascorbic acid at pH = 7.0 and under continuous  $N_2$  flow ( $T = 21.5$  °C). Positions of the labeled sites are indicated in the inset. The kinetic decays were fitted via a single exponential equation (solid lines).

When the pH was lowered below the  $pK_1$  of ascorbic acid to pH = 3.3, a completely different redox behavior of SL-WALP23 was observed (Figure 5.9). First, the reduction kinetic curve of SL-WALP-C23 was found not to follow the single exponential decay. The EPR signal intensity abruptly drops within first 10 min and then the reduction rate slows down. Secondly, the extent of reduction of SL-WALP-C12 increased from 5% to 20%. Thirdly, the reduction rate of SL-WALP-C16 at acidic conditions was found to be higher than that at neutral pH; this observation indicates that ascorbic acid in its neutral form effectively penetrates into membrane. Fourthly, the extent of reduction of SL-WALP-C16 was found to be even higher than that of SL-WALP-C23 with a spin-labeled site exposed to the lipid bilayer interface. The latter observation could be rationalized if we assume that the WALP insertion into the membrane is bidirectional. If it is so, the fraction of the nitroxide belonging to SL-WALP-C23 peptide will be residing at the interface of the inner leaflet, and its reduction requires ascorbic acid to diffuse through the whole thickness of the bilayer. At a similar transmembrane arrangement, the spin label in SL-WALP-C16 will be positioned closer to the outer interface and will be reached by diffusing ascorbic acid faster. Since we cannot distinguish between the nitroxides in the inner and outer leaflets, the overall apparent reduction rate for SL-WALP-C16 seems to be higher than that for SL-WALP-C23. This might explain why kinetic curve for the reduction of SL-WALP-C16 at pH = 3.3 although could be fitted to a single exponential equation, but not ideally (Figure 5.9).

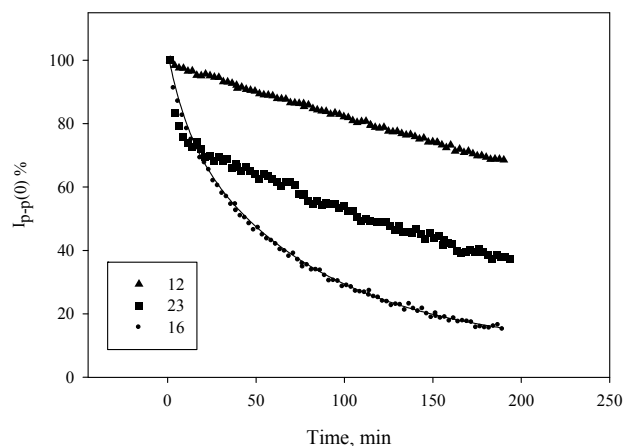


**Figure 5.9.** Central EPR spectral component intensity decay for MTSL-labeled WALP23 peptides in DOPC induced by five-fold molar excess of ascorbic acid at pH = 3.3 and under continuous N<sub>2</sub> flow (21.5 °C). Positions of the labeled sites are indicated in the inset. The kinetic decays were fitted via a single exponential equation (solid lines).

**Table 5.1 Reduction rate constants of SL-WALP23 peptides in DOPC membrane by ascorbic acid at 21.5 °C.**

Peptide Name	pH	$k, \text{min}^{-1}$
SL-WLAP23C23	7.0 ± 0.3	$1.7 \times 10^{-2} \pm 0.0 \times 10^{-2}$
SL-WALP23 C16		$5.1 \times 10^{-3} \pm 1.7 \times 10^{-3}$
SL-WALP23 C12		- <sup>a</sup>
SL-WALP23 C23	3.3 ± 0.3	- <sup>a</sup>
SL-WALP23 C16		$1.7 \times 10^{-2} \pm 0.0 \times 10^{-2}$
SL-WALP23 C12		- <sup>a</sup>

<sup>a</sup> Single exponential curve fitting is not applicable.

The reduction conditions used for SL-WALP23 peptides were also applied to MTSL-labeled Cesa TMH5 peptides. Kinetic decay curves of SL-TMH5 peptides co-inserted with three-fold excess of WALP8S in DOPC bilayers and the corresponding kinetic parameters are shown in Figure 5.10 and Table 5.2, respectively. Note that the EPR signal intensity for TMH5 L13C variants significantly drops at acidic pH, although it stays essentially unchanged at neutral pH. We speculate that under acidic conditions there could be at least two factors contributing to the observed intensity change. Firstly, an effective diffusion of the neutral form of ascorbic acid to the center of the bilayer and secondly, a partial disaggregation of the TMHs that makes the spin-labeled sites more accessible to ascorbic acid. A higher reduction rate of the nitroxide in the terminal position (C2) compared to that of the nitroxide in the middle of the peptide (L13C) supports our conclusion on the transmembrane arrangement of CesaTMH5 peptides. Since the association of the TMH5 helices and resulted dipolar interactions of the adjacent nitroxides cause EPR spectral broadening, using a peak-to-peak intensity of the central EPR spectral line is not quite accurate to determine the concentration of spins. For this reason, we also used double integration of the spectra to follow the course of reduction (Figure 5.10 (C) and (D)). Because only 5 scans were averaged for each data point, the spectra were too noisy to accurately calculate double integrals. However, the trends similar to that plotted in Figure 5.10, (A) and (B) were observed. It is interesting to note that in the experiments carried out with SL-TMH5 C2 at pH = 7.0 the intensity of the central spectral line  $I_{p-p}(0)$  slightly increases (Figure 5.10 (E)) while the corresponding double integrals (Figure 5.10 (F)) slightly reduce (by  $\approx 20\%$ ). This is most likely because in the aggregated peptide the “outer”

nitroxides are more accessible to ascorbic acid and more readily reduced; as a result, the dipolar interactions with the “buried” nitroxides was reduced to some extent that caused an increase of  $I_{p-p}(0)$ .

For SL-TMH5 L13C at pH = 7.0 the  $I_{p-p}(0)$  also slightly increases (Figure 5.10 (E)), although to lower extent and only within first 125 min. After this period the spectral line intensity stays essentially without change. Within the same period the corresponding double integrals also decrease (Figure 5.10 (F)) and then remain unchanged. Since at pH = 7.0 the diffusion of ascorbate through the membrane is highly unlikely, we suppose that this observation could be explained by formation of a pore in the lipid bilayer. Indeed, the aggregated peptide could disturb the nearby lipids and increase a permeability of the lipid bilayer. As a result, the “outer” nitroxides are being reduced within first 125 min, but steric hindrance of the “buried” nitroxides protects them from oxidation.

**Table 5.2 Reduction rate constants of SL-TMH5 co-inserted with 3 fold WALPL8S in DOPC membrane by ascorbic acid at 21.5 °C.**

Label position	pH	$k, \text{min}^{-1}$ , by Double Integration	$k, \text{min}^{-1}$ , by $I_{p-p}(0)$
2	$7.0 \pm 0.3$	- <sup>a</sup>	- <sup>a</sup>
13		- <sup>a</sup>	- <sup>a</sup>
2	$3.3 \pm 0.4$	$5.5 \times 10^{-2} \pm 1.1 \times 10^{-2}$	$4.0 \times 10^{-2} \pm 0.0 \times 10^{-2}$
13		$3.2 \times 10^{-2} \pm 0.1 \times 10^{-2}$	$2.1 \times 10^{-2} \pm 0.1 \times 10^{-2}$

<sup>a</sup> Single exponential curve fitting is not applicable.

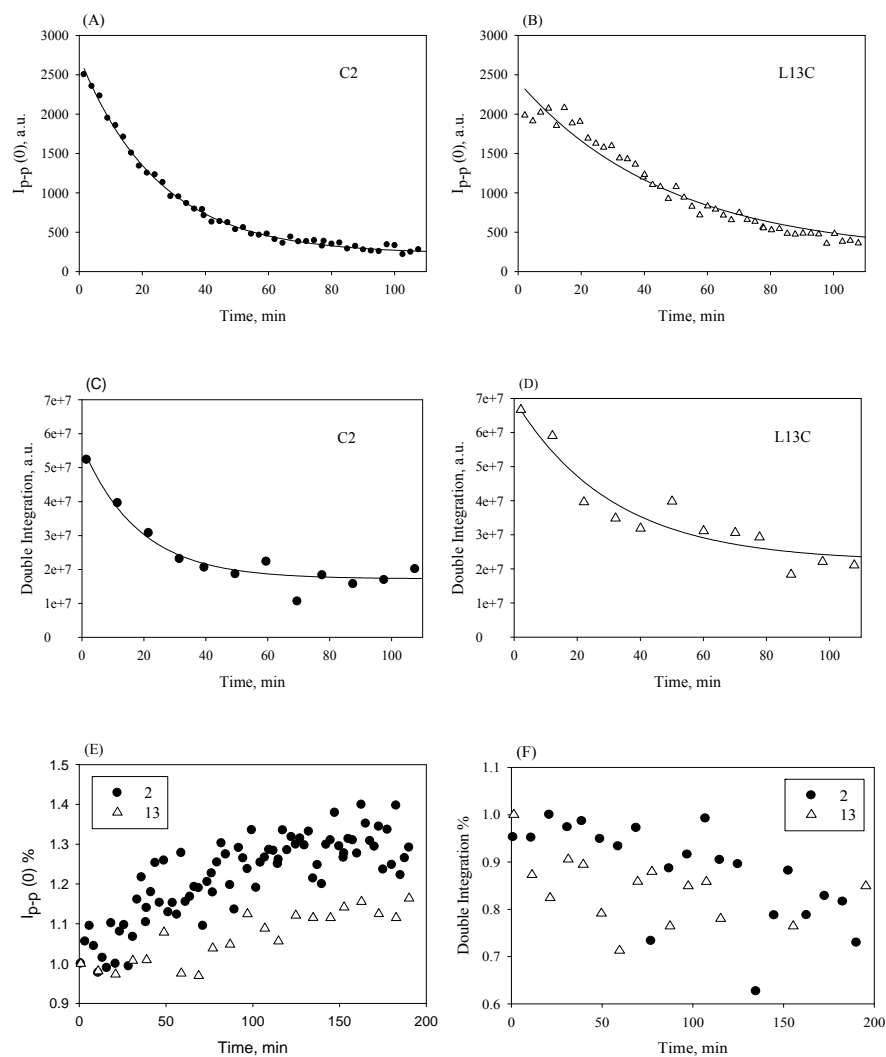


**Figure 5.10** Reduction of MTSL-labeled Cesa TMH peptides co-inserted with 3-fold excess of WALP C8S in DOPC bilayers with ascorbic acid. A and B: the EPR central component intensity decays; C and D: changes in double integrals of the EPR spectra plotted against time (pH = 3.3; T = 21.5 °C, continuous N<sub>2</sub> flow). E and F: change of relative intensities of the EPR central lines and double integrals of the EPR spectra, respectively, at neutral pH. Only 5 spectra were averaged for each data point. Positions of the labeled sites are indicated in the insets.

### 5.3 Conclusion

Our experiments clearly demonstrate that for the aggregated transmembrane helices such as TMH5 from the transmembrane domain of the plant cellulose synthase GhCesA1 from cotton, *Gossypium hirsutum*, the extent of oligomerization at both neutral and acidic pH could be reduced by TMH5 co-insertion with a disaggregant, e.g., a membrane-spanning non-aggregating  $\alpha$ -helical WALP23 peptide. This conclusion is supported by the experimental EPR measurements of the mobility ( $(\Delta H(0))_{p-p}^{-1}$  parameter) and the oxygen accessibility ( $(\Delta\Delta B_{p-p}^L)$  parameter) of the spin-labeled side chains of TMH5, as well as by mapping the polarity profile along the peptide backbone (measuring of the anisotropic nitrogen hyperfine coupling constant  $A_{zz}$  from the rigid-limit X-band EPR spectra). The results of the all three types of the EPR experiments were found to be completely consistent with each other. The rationale for the disaggregating effect of WALP23 peptide is speculated to be a substitution of the hydrogen-bonding and electrostatic interactions between TMH5 helices with weaker Van der Waals interactions between TMH5 and a disaggregant. The helices of WALP23 peptide most likely occupy the lateral position around the TMH5 helices. The discrepancies between the results of the EPR experiments carried out for SL-TMH5 co-inserted with WALP23 peptide and the same experiments performed with the membrane-spanning non-aggregating  $\alpha$ -helical SL-WALP23 peptides were suggested could be explained by water penetration down the pore formed by aggregate of TMH5 peptide. The increased permeability of the lipid bilayer pierced with the TMH5 aggregate to small molecules was demonstrated by comparing the rates of reduction of the nitroxides tethered to

the terminal position and the membrane-buried sites of TMH5 with ascorbic acid/ascorbate. Because of the presence of extrinsic WALP23 peptide, the effect of the peptide's co-insertion on the  $\alpha$ -helical content of the TMH5 cannot be revealed by using CD spectroscopy. However, basing on the observation that co-insertion with WALP23 reduces the side chain mobilities, we speculate that the  $\alpha$ -helical content is increasing upon co-insertion; the intrahelical hydrogen bonding stabilizing the  $\alpha$ -helix make it more rigid, which imposes additional motional restrictions on the side chains.

## APPENDICES

## Appendix A      TMH5 reconstitution into mixed lipid bilayers

### A.1. Room temperature X-band CW EPR

CesA TMH5 peptide was found to be significantly aggregated in lipid bilayers formed from DOPC, DLPC, DMPC and DMPC lipids (see Chapters 3-5). We also tried to reconstitute TMH5 peptide to the vesicles composed from the mixture of DOPC and DLPC at molar ratio of 4:1. A series of the EPR spectra of MTSL-labeled CesA TMH5 variants in this mixed lipid bilayer at pH = 3.3 is shown in Figure A1. Before the EPR measurements all the samples were subjected to 3% (w/v) sucrose purification as described in Chapter 2. Despite that the TMH5 variants other than TMH5 C2 and TMH5 V9C exhibit the spectra typical for the spin-labeled transmembrane  $\alpha$ -helical peptides, showing no intensive aggregation in this mixed lipid bilayers, measurement of the peak-to-peak width of the central EPR line  $\Delta B(0)_{p-p}^{-1}$  indicates the presence of the tertiary contact at the 9<sup>th</sup> position<sup>16</sup> ( $< 0.3$  G) (Figure A2). Therefore, TMH5 peptide is partially oligomerized in mixed DOPC/DLPC vesicles.

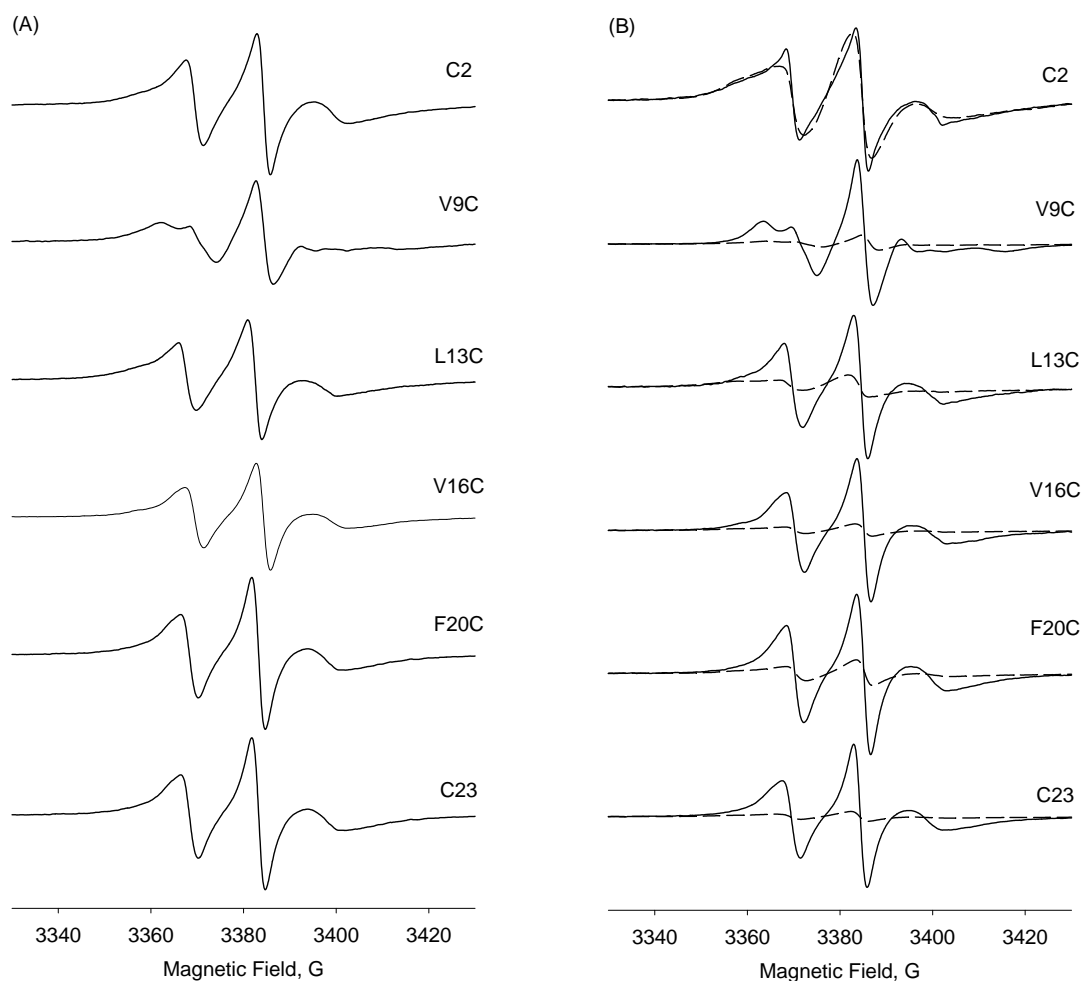


**Figure A1.** Room temperature X-band CW EPR of MTSL-labeled Cesa TMH5 embedded in DOPC/DOPC (4:1) vesicles at pH = 3.3. (A) Before sucrose separation. (B) After 3% (w/v) sucrose separation. The spectra acquired from the top layers are shown in solid lines, the spectra acquired from the bottom layers are shown in dashed lines.

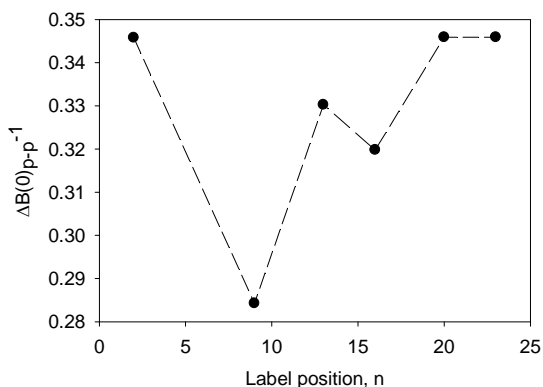


**Figure A2.**  $\Delta B(0)_{p-p}^{-1}$  for TMH5 peptides in DOPC/DLPC (4:1) bilayer plotted against the label positions.

## A.2 Accessibility and polarity profiles

To ascertain the arrangement of TMH5 helices in the mixed-lipid bilayers, we carried out the oxygen accessibilities experiments and probed the local polarity along the peptides' backbone. Only top layer obtained after the sucrose separation were used in these experiments.

The Figure A3 (A) shows how the oxygen-induced line broadening  $\Delta\Delta B_{p-p}^L$  for SL-TMH5 variants in DOPC/DLPC (top layer) at pH = 3.3 (black circles) changes with the position of labeling. For comparison, the data acquired for SL-WALP23 embedded in DOPC bilayers are shown as grey squares. All spin-labeled positions in TMH5 show much weaker broadening effect compared to similar positions of WALP23 peptides in DOPC bilayers, although in general the plot follows the same pattern as WALP23 peptide. Thus, the nitroxide at 13<sup>th</sup> position corresponding to the center of the peptide and located in the most hydrophobic region of the lipid bilayer, shows the most pronounced EPR line broadening

effect. This accessibility profile confirms the transmembrane arrangement of the TMH5 peptide as it was demonstrated in the previous Chapters. Figure A3 (B) shows the polarity profile obtained by measuring the anisotropic nitrogen hyperfine coupling constants  $A_{zz}$  from the 77K rigid-limit EPR spectra of SL-TMH5 in DOPC/DLPC bilayers at pH = 3.3 (black circles) and plotting them against the labeling position. Polarity profile of WALP23 in DOPC (grey squares) at pH 7 is shown for comparison. The  $A_{zz}$  values for the nitroxides in the 2<sup>nd</sup> and 23<sup>rd</sup> positions of the TMH5 and the corresponding positions of the WALP peptide are essentially the same. The magnitude of  $A_{zz}$  for the nitroxides at the other positions of the TMH5 is significantly lower than that for WALP peptide, although the observed trends in the  $A_{zz}$  changes are similar. The polarity profile demonstrates consistency with the accessibility profile, thus confirming the transmembrane arrangement of the TMH peptide.

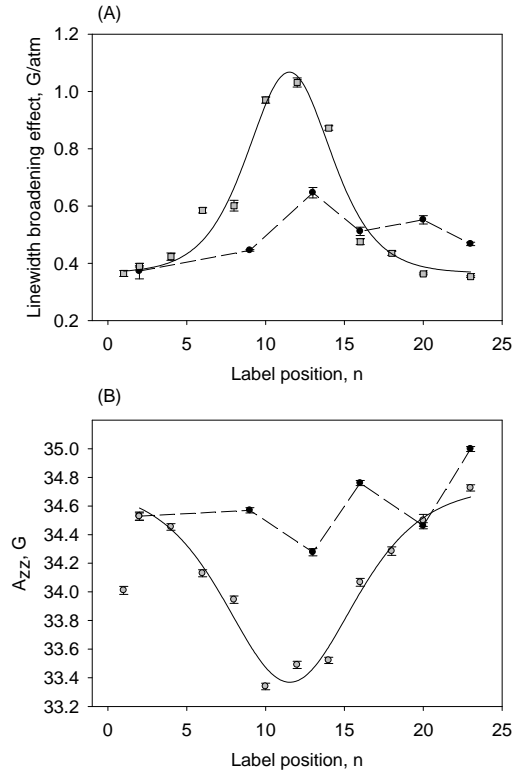


**Figure A3.** (A) Central EPR line width broadening  $\Delta B_{p-p}^L$  induced by oxygen and (B) polarity profile of TMH5 (pH = 3.3) in DOPC/DLPC (4:1) vesicles. (A): Oxygen-induced central EPR line width broadening  $\Delta B_{p-p}^L$  for SL-TMH5 reconstituted to DOPC/DLPC (4:1) vesicles at pH = 3.3 (●) and for MTSL-labeled WALP23 peptide in DOPC lipids at pH = 7.0 (◻) shown as a function of the spin-labeling position. (B): Anisotropic nitrogen hyperfine splitting constants  $A_{zz}$  for SL-TMH5 reconstituted to DOPC/DLPC (4:1) vesicles at pH = 3.3 (●) and for MTSL-labeled WALP23 peptide in DOPC vesicles at pH = 7.0 (◻) shown as a function of the spin-labeling position. Solid lines are the least-squares fits of the experimental data to the Equation 2.3. The dashed lines connecting the data points acquired for the SL-TMH5 serve as guides for an eye.

### A.3 Does DLPC form a microdomain within the DOPC membrane? Experiments with the spin-labeled DLPC lipids.

The experiments with the mixed DOPC/DLPC bilayers raised the following questions: (1) whether DOPC and DLPC lipids are completely miscible or DLPC forms microdomains within the DOPC bilayers and (2) if DLPC forms microdomains, which domain, DOPC- or DLPC-rich, the TMH5 helices prefer to embed? To address these questions, we synthesized a spin-labeled analog of DLPC lipid (SL-DLPC) (Figure A4) and measured the EPR spectra of the DOPC bilayers doped with various amounts of SL-DLPC. As in the experiments with unlabeled DLPC, in the experiments with the spin-labeled DLPC the total DOPC to DLPC molar ratio was kept at 4:1.

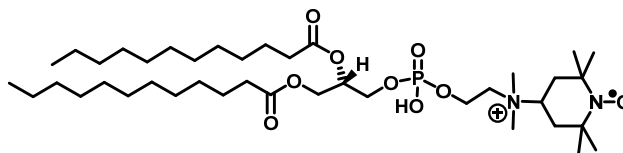


**Figure A4.** Chemical structures of the spin-labeled DLPC lipid.

The X-band EPR spectra of the DOPC bilayers doped with various amounts of the SL-DLPC lipid are shown in Figure A5 (A). The X-band EPR spectrum of the DOPC bilayers doped with 20 mol % of Tempo-POPC is presented in Figure A5 (B) for comparison. A slow-motion three-line EPR spectrum acquired for DOPC/Tempo-POPC (4:1) mixture (Figure A5 (B)) demonstrates that these lipids are completely miscible at these concentration. In contrast, the EPR spectrum of DOPC bilayers doped with 20 mol % of SL-DLPC showed

only a single broad asymmetric line (Figure A5 (A), solid line) characteristic for aggregated spin-labeled lipid. Magnetic dilution of the SL-DLPC lipid with approximately 50 % of the unlabeled DLPC lipid, keeping the total DLPC-DOPC ratio at 1:4 resulted in appearance of a weak three-line pattern (Figure A5 (A), dotted line). And only upon a further dilution, at 1.9 % concentration of SL-DLPC, a three line spectrum similar to that registered for DOPC/Tempo-POPC (4:1) mixture was observed (Figure A5 (A), dashed line).

These observations can be interpreted as follows. Because of the strong dipole-dipole interactions between the adjacent spin labels of the SL-DLPC lipids in these local domains, the three EPR lines collapse into the one broad line. The asymmetry of the spectral line most likely result from the two populations of the paramagnetic species present in the domain: the boundary SL-lipid molecules and the SL-lipid molecules in the interior of the domain. The single broad spectral line is primarily contributed by strongly interacting lipids of the interior. This broad line is supposed to be modulated by a three-line spectrum corresponding to weakly interacting boundary lipids, resulting in the single asymmetric spectral line. Thus, these experiments demonstrate that DOPC and DLPC are not miscible at 4:1 molar ratio and DLPC forms a local domain within DOPC bilayers.

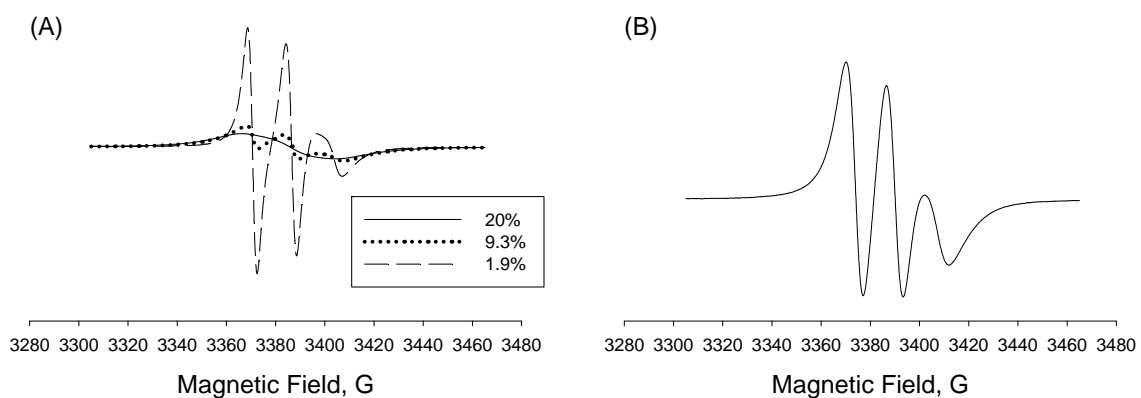


**Figure A5** (A): Room temperature X-band CW EPR spectra of DOPC/DLPC (4:1) vesicles doped with the spin-labeled DLPC, pH = 3.3. (B): DOPC vesicles doped with 20 mol % of Tempo-POPC, pH = 3.3. The concentration of the SL-DLPC (in molar percent) is indicated in the insert. Spectra were normalized by double integration to the same amount of spins.

To ascertain the arrangement of the TMH5 peptide in the mixed DOPC/DLPC (4:1) bilayers, the native TMH5 was reconstituted into DOPC/DLPC (4:1) lipids doped with 10 mol % of SL-DLPC. The total lipid-to-peptide ratio was increased to 20:1 to enhance the effect of the peptide (Figure A6 (A)). With the peptide incorporated, the amplitude of the broad component slightly decreased, while the intensity of the three-line signal slightly increased; this indicates that incorporation of the TMH5 peptide resulted in dilution of the dipolar interactions between the molecules of SL-DLPC. Therefore, it was concluded that the peptide was inserted into the DLPC phase.

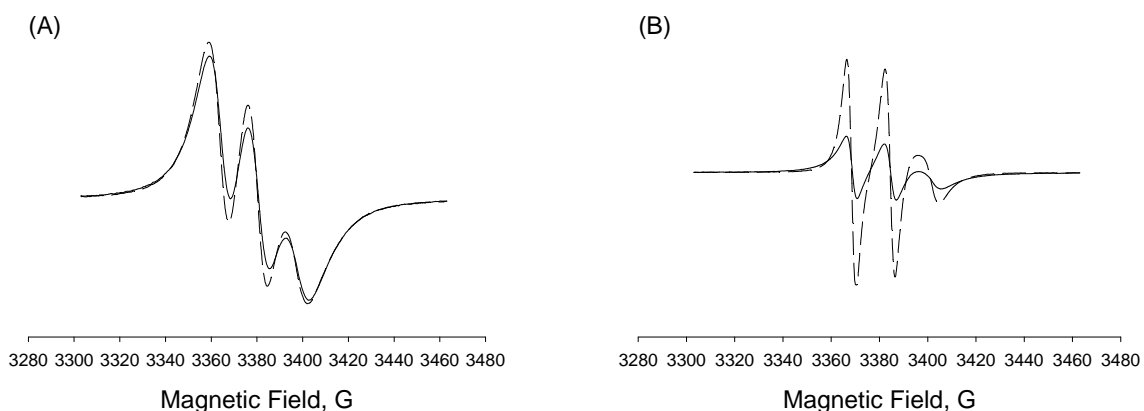


**Figure A6.** Room temperature X-band CW EPR spectra of DOPC/DLPC (4:1) bilayers containing 10 mol % of SL-DLPC (A) and DOPC bilayers doped with only 1 mol % of SL-DLPC (B) are shown in a solid line. Dashed line - in the present of native CesA TMH5 at pH = 3.3. Spectra were normalized by double integration to the same amount of spins.

Figure A6 (B) shows the EPR spectra acquired from DOPC bilayers doped with 1 mol % of SL-DLPC in the absence (solid line) and in the presence (dashed line) of native TMH5 peptide. It is seen that the EPR signal intensity increased, which could be interpreted as a dilution of dipolar interactions between the nitroxides of SL-DLPC by the helices of a peptide. This observation suggests that even at very low concentration (1 mol %) of DLPC in DOPC bilayer, the former lipids are still aggregated to some extent.

**Appendix B      $\alpha$ -Helical membrane-spanning WALP peptide as a reference for  
the determination of membrane arrangement of the transmembrane  
helices.**

**B.1 Introduction**

The polarity gradient across the lipid membrane have been probed with various techniques including neutron diffraction, capacitance measurements, fluorescence and spin-labeling EPR (ref. 155 and refs. cited herein). An  $\alpha$ -helical membrane-spanning WALP23 peptide has been proposed as a ruler to determine the location of the labeled sites within the lipid membrane. WALP23 peptide consists of Leu-Ala repeats capped by terminal Trp<sup>28</sup>; the hydrophobic Leu-Ala repeats are located in the hydrophobic interior of the lipid bilayer, and the capping Trp partitioned into the polar headgroup region serve as the anchors ensuring the peptide consistent registration in the lipid bilayer<sup>74</sup>. The membrane arrangement of this peptide in DOPC bilayers is well characterized by several spectroscopic techniques including circular dichroism (CD) and IR spectroscopy<sup>156</sup>. The sensitivity of the magnetic parameters (e.g.,  $A_{iso}$  and g-factor) of the spin labels to the dielectric permittivity of the local environment allows creating a reference polarity profile of the membrane. This profile can be employed to characterize the local environment of the spin-labeled sites of the Cesa TMH peptide and, hence, its membrane arrangement. The purpose of this section is to set a reference for further studies of the membrane arrangement of Cesa TMH peptides. Thus, the spin-labeled WALP23 peptide variants were characterized in both DOPC and DLPC bilayers. The hydrophobic length of WALP23 peptide has been demonstrated to match well the

hydrophobic thickness of the DOPC bilayers ( $\approx 27 \text{ \AA}$ )<sup>74, 157</sup>. However, a shorter DLPC lipid will assemble into a much thinner membrane ( $\approx 19.5 \text{ \AA}$ ).<sup>74, 157</sup> When WALP23 inserted into the DLPC bilayer, the hydrophobic mismatch will take place, because hydrophobic thickness of the lipid bilayer is not suitable to adapt the hydrophobic transmembrane segment of the peptide<sup>71, 157</sup>. From the theoretical standpoint, there are several possibilities for either protein/peptide or membrane to relieve the energetic constraints caused by the hydrophobic mismatch<sup>71</sup>. When the hydrophobic segment of the protein is longer than the hydrophobic bilayer thickness, the protein might form aggregates, change a tilt, or shorten its backbone to reduce the exposed hydrophobic area. When the hydrophobic parts are shorter compared to the hydrophobic bilayer thickness, this again will induce either the protein aggregation or backbone conformation changes to minimize the hydrophobic mismatch effect. Moreover, when peptide is too short, it could partition into the lipid bilayer surface instead of being inserted. Alternatively, the acyl chains of the lipid may also make changes to match the length of the hydrophobic segment of a peptide/protein. For example, ordering the acyl chain would thicken the bilayer while additional disordering would make the membrane thinner.

The WALP23 peptides spin labeled with methanethiosulfonic acid S-(1-oxy-2,2,5,5-tetramethyl-2,5-dihydro-1*H*-pyrrol-3-ylmethyl) ester (MTSL, spin label III in Figure 1.1) (SL-WALP23, sequences are shown in Table 2.3) reconstituted into DOPC or DLPC bilayers were characterized with the three different EPR-based biophysical methods. First two methods are based on the effect of collision of molecular oxygen with the nitroxide that results in decreasing the relaxation time. Time domain pulse saturation recovery technique that allows for measuring this effect by EPR has been described in the literature<sup>28</sup>.

Measuring the peak-to-peak line width from the continuous wave (CW) EPR spectra in the presence and absence of molecular oxygen<sup>36</sup> also allows to follow the changes in the nitroxide relaxation time. The polarity profiles of SL-WALP23 peptide in DOPC and DLPC bilayers were characterized by measuring the Z component of the hyperfine interaction tensor ( $A_{zz}$ ) of the spin probe in frozen (77K) samples.

## B.2 Results and discussion

### B.2.1 CD characterization of $\alpha$ -helical peptides

The secondary structure of SL-WALP23-C12 was tested by Circular Dichroism (CD) spectroscopy (Figure B1). The CD spectra of WALP peptide exhibit the pronounced minima at 208 and 222 nm<sup>66</sup> thus indicating that the peptide retains  $\alpha$ -helical structure both in DOPC and DLPC bilayers.

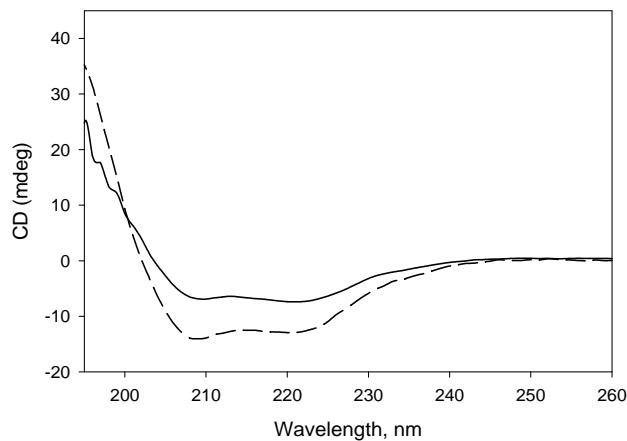


**Figure B1.** Circular dichroism spectra of SL-WALP23-C12 peptide in the bilayers composed of DOPC (solid line) and DLPC (dashed line). Peptide concentrations were the same.

## B.2.2 Measurement of O<sub>2</sub> and NiEDDA relaxation profiles for MTSL-WALP23 peptides in DOPC and DLPC bilayers using pulsed EPR saturation recovery technique

The first 10  $\mu$ s of a pulsed EPR saturation recovery (pSR) curve for SL-WALP23-C4 in DOPC bilayers equilibrated with air, or N<sub>2</sub>, or 50 mM NiEDDA, are shown in Figure B2. Typically, the pSR signals are fitted to a single exponential decay, otherwise using double exponential fits. However, the second exponential component is not significant. The pSR signals were averaged when the magnetic field is set right in the center of the resonance position of field sweep spectrum.

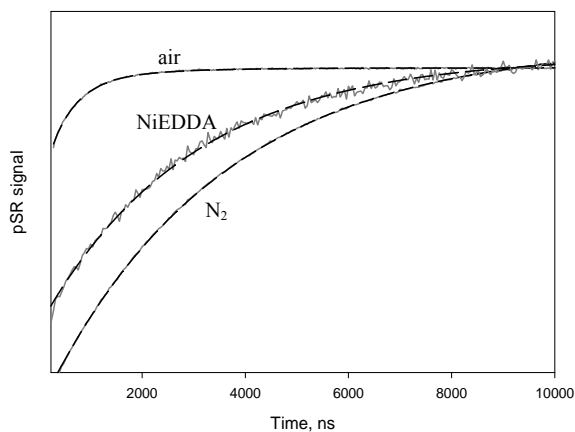


**Figure B2.** First 10  $\mu$ s of the experimental pulse saturation recovery curves of MTSL-WALP23-C4 in the presence and absence of relaxing agents. The  $T_1$  values were obtained from the fitting of the experimental curves by exponential decay function with single or double components. The spectra were normalized by maximum intensity.

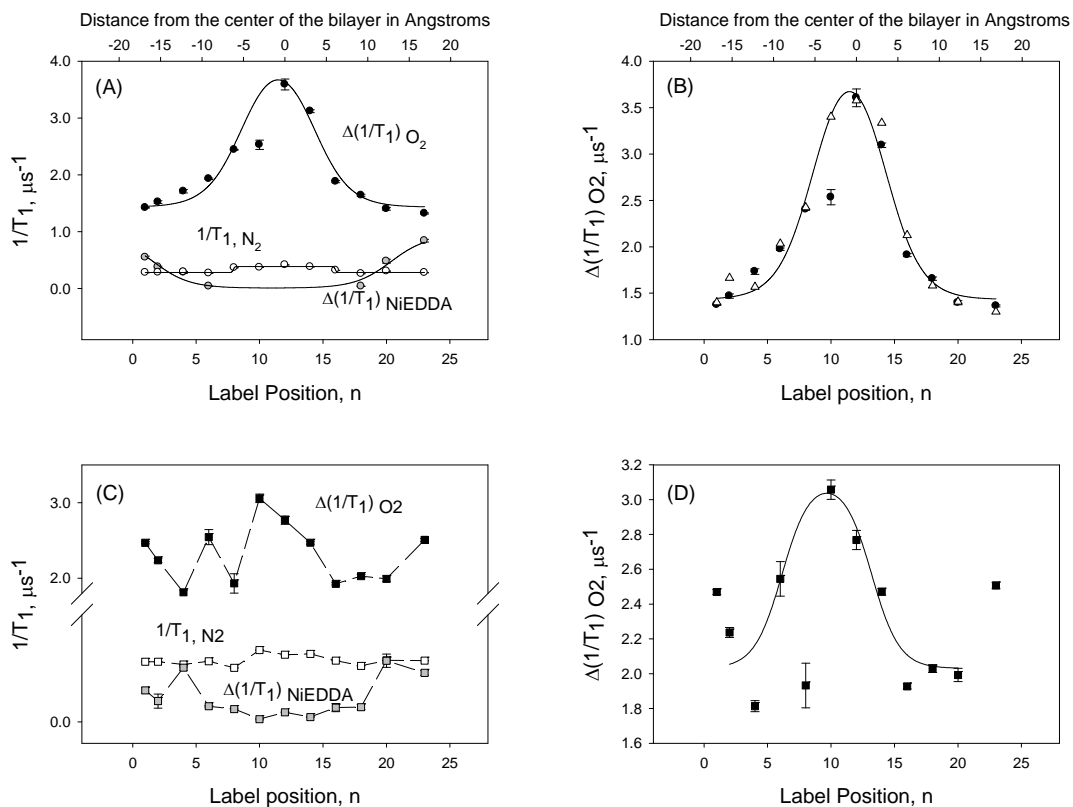


**Figure B3.** Room temperature relaxation rates acquired from the saturation recovery pulsed EPR experiments for the spin-labeled WALP23 peptide reconstituted into DOPC (A) or DLPC (C) bilayers. (B) Comparison of relaxation rate enhancement by air for MTSL-WALP23 in DOPC bilayers ( $\bullet$ ) (room temperature, this study) and data reported by Nielsen *et al*<sup>28</sup> ( $\Delta$ ) (Solid line represent the fits of the experimental data acquired from this work). For the calculation of distance from the center of the bilayer (top X axis) see the Experimental Section. (D) Relaxation rate enhancement by air for MTSL-WALP23 in DLPC bilayers, room temperature. Solid lines represent the least-squares fits of the experimental data to the Equation 2.3. The dashed lines connecting the data points serve as guides for an eye.

Figure B3 shows the  $\Delta(1/T_1)_{\text{air}}$  data for SL-WALP23 in DOPC ((A), black circles) and DLPC ((C), black squares) bilayers. For comparison, the data by Neilson *et al*<sup>28</sup> obtained for SL-WALP23 in DOPC bilayers ((B), white triangles) are also presented. The solid lines represent the best least-squares fits of the experimental data to the symmetric profile, Equation 2.3. The optimized parameters of  $\lambda$ ,  $n_0$ , and  $d$ , are given in Table B1. For the WALP23 peptides perfectly centered in the DOPC bilayer, the  $d$  should be equal to  $d=12$  residues, which is close to the value of  $d=11.5$  residues determined from fitting of the saturation recovery data, see Table B1. The transition region width ( $\lambda$ ) was determined to be  $\lambda=0.22\pm 0.08$  nm. The fitting parameters for the data taken from Neilson *et al*<sup>28</sup> are also presented in Table B1 and as it could be seen these independently obtained two data sets are consistent with each other. Because of the hydrophobic mismatch occurring when WALP23 peptides were incorporated to the DLPC bilayers, the  $\Delta(1/T_1)_{\text{air}}$  data could be successfully fit to the Equation 2.3 only when data measured for the residues 1, 4, 8, and 23 were omitted. We speculate that these data points are falling out of the general trend because of the association of the WALP23 peptide helices induced by the hydrophobic mismatch (see discussion further in the text) and associated displacement of the central amino acid residue from the center of the bilayer close to the lipid bilayer interface. Note, that for WALP23/DLPC the 10<sup>th</sup> residue resides in the center of the bilayers ( $d = 9.62\pm 0.7$  residues,  $\lambda$  is reduces to  $\lambda=0.17\pm 0.1$  nm).

The results of the  $\Delta(1/T_1)_{\text{NiEDDA}}$  measurement for WALP23 peptides both in DOPC ((A), white circles) and DLPC ((C), white squares) bilayers are shown in Figure B3. Note,

that for the residues from 8<sup>th</sup> to 16<sup>th</sup> of the WALP23 peptide the  $\Delta(1/T_1)_{\text{NiEDDA}}$  cannot be measured, because polar NiEDDA does not penetrate into the hydrophobic core of the DOPC bilayer. However, for the same peptide embedded into the shorter DLPC bilayers, some insignificant penetration of NiEDDA to the labeled positions in the center of the bilayer was observed. This effect could be explained by a lipid bilayer distortion caused by the peptide association/hydrophobic mismatch.

### **B.2.3 EPR linewidth ( $T_2$ ) method to measure oxygen permeability for the MTSL-WALP23 peptides embedded into DOPC or DLPC bilayers**

The results of  $\Delta\Delta B_{\text{p-p}}^{\text{L}}$  measurements for MTSL-WALP23 in DOPC and DLPC bilayers acquired under variable  $\text{O}_2$  pressure are shown in Figure B4 in comparison with the pSR data acquired for the samples equilibrated with air at normal pressure.

The optimized parameters  $\lambda$ ,  $n_0$ , and  $d$  are given in Table B1. Fitting of the experimental data for WALP23 in DOPC bilayers to the Equation 2.3 yields  $d=11.5\pm 0.1$  residues. The transition region width ( $\lambda$ ) was found to be  $\lambda=0.21\pm 0.06$  nm. For WALP23 embedded in DLPC bilayers, the  $\Delta\Delta B_{\text{p-p}}^{\text{L}}$  profile fits well to the Equation 2.3 only if data measure for residues 1, 4, 8 and 23 were omitted. For this reason the transition region width ( $\lambda$ ) cannot be accurately determined. For the WALP23 peptides in the DLPC bilayers the maximum oxygen accessibility was found to correspond to the 10<sup>th</sup> residue ( $d=9.62\pm 0.7$ ).

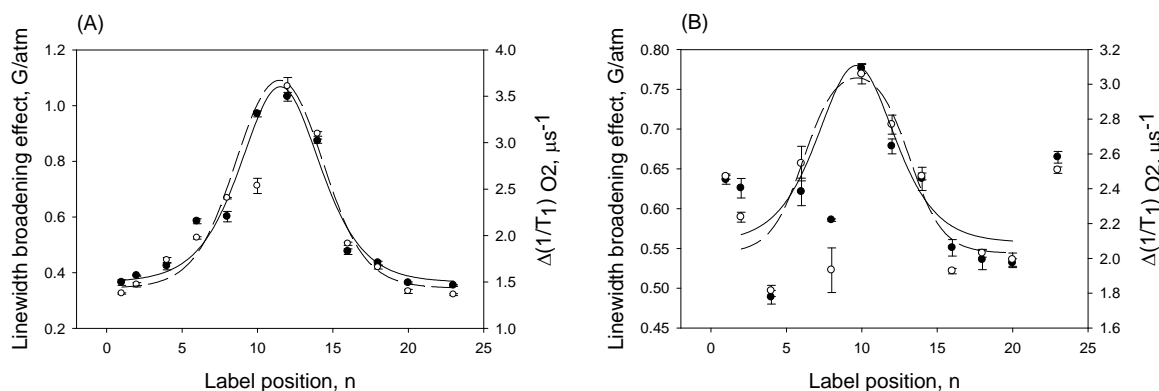


**Figure B4.** Overlap of  $\Delta\Delta B_{p-p}^L$  profiles ( $\bullet$ ) acquired from X-band CW EPR with the relaxation rate profiles ( $\circ$ ) acquired from pulsed saturation recovery EPR for the spin-labeled WALP23 in DOPC (A) and DLPC (B) vesicles. Solid (DOPC) and dashed (DLPC) lines were obtained by least-squares fitting the experimental data to Equation 2.3 using the optimized parameters discussed in the text.

**Table B1.** Optimal least-square fit to Equation 2.3 parameters calculated from various methods.

	pSR MTSL-WALP DOPC	Linewidth MTSL-WALP DOPC	Neilsen <i>et al</i> <sup>28</sup> (pSR, MTWL- WALP, DOPC)	pSR MTSL-WALP DLPC
$\lambda$ , nm	$0.22 \pm 0.08$	$0.21 \pm 0.06$	0.20(5)	$0.17 \pm 0.1$
$n_0$ , nm	$0.42 \pm 0.2$	$0.37 \pm 0.2$	0.49(9)	$0.54 \pm 0.2$
$d$	$11.5 \pm 0.2$ residue position	$11.5 \pm 0.1$ residue position	11.7(2) residue position	$9.67 \pm 0.4$ residue position

#### **B.2.4 Local polarity along the WALP23 peptide helices: measuring anisotropic $A_{zz}$ coupling constant of the spin labels from the rigid-limit spectra of frozen (77K) samples.**

Probing the local polarity along the peptide backbone with EPR is based on the exquisite dependence of the anisotropic nitrogen hyperfine coupling constant  $A_{zz}$  of the nitroxide on the dielectric permittivity of the media<sup>90</sup>. The polar solvents were shown to stabilize the dipolar form of the nitroxide, thus increasing the spin density at the nitrogen atom of the nitroxide group and, therefore, increasing the nitrogen hyperfine coupling constant. In this study, we measured the z component of the anisotropic hyperfine tensor from the least-squares simulation of the high- and low-field components of the rigid-limit spectra of the freeze-quenched in liquid nitrogen (77K) lipid samples containing the inserted peptide. Figure B5 shows the experimental rigid-limit EPR spectra of the SL-WALP23 in DOPC lipid bilayers superimposed with the corresponding simulated high- and low-field spectral components. The distance between the components shown with the arrow represents  $2A_{zz}$  value.

Measuring the anisotropic  $A_{zz}$  for the spin-labeled sites along the peptide backbone would report on the local dielectric nearby the labeled sites, allowing to correlate the position of the labeled site with the specific depth in the lipid bilayer and, hence, to gain the information on the peptide arrangement. Figure B6 shows the polarity profiles based on the experimentally measured  $A_{zz}$  values for SL-WALP23 peptide in DOPC (black circles) and DLPC (white circles) bilayers. As it could be seen, the SL-WALP23 is well registered in the DOPC bilayer with a little “bend” back into membrane at the N-terminal (note the lower  $A_{zz}$  value for SL-WALP23-C1). The residue at the water-lipid interface showed a much higher

$A_{zz}$  coupling, while the smaller  $A_{zz}$  values correspond to the center of the lipid bilayer. For the same peptide inserted into the DLPC bilayers a quite different  $A_{zz}$  profile was obtained. The  $A_{zz}$  data plotted against the labeling position along the peptide backbone revealed the discontinuous pattern indicating a significant distortion of the  $\alpha$ -helix that most likely caused by the hydrophobic mismatch-induced peptide association and displacement of the central amino acid residue from the center of the bilayer close to the lipid bilayer interface.

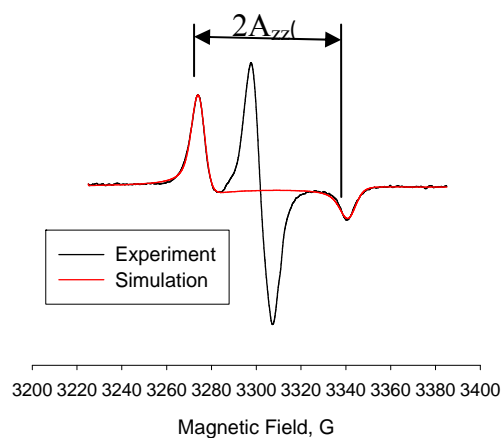


**Figure B5.** Rigid-limit EPR spectra (77K) of MTSL-WALP23-C23 in DOPC bilayers overlapped with the simulated high- and low-field components shown in red.

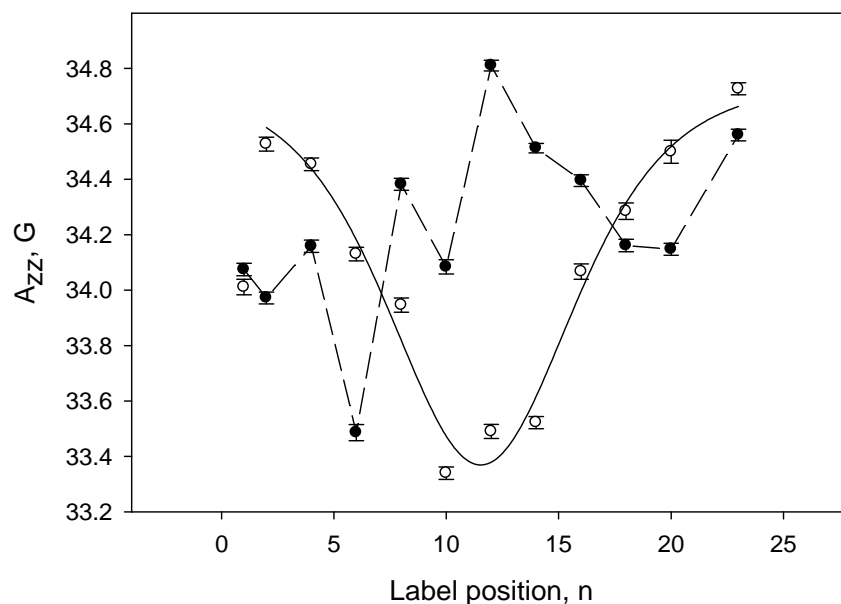


**Figure B6.** The anisotropic nitrogen hyperfine coupling constant  $A_{zz}$  for SL-WALP23 peptide in DOPC (○) and DLPC (●) bilayers. Solid line represents the fit of the experimental data to the Equation 2.3.

### B.2.5 Arrangement of the WALP peptides in DOPC and DLPC bilayers

To summarize, despite that the CD spectra of the MTSL-WALP23 peptide both in DOPC and DLPC bilayers report on a high  $\alpha$ -helical content (Figure B1), their  $A_{zz}$  polarity profiles are completely different. When the hydrophobic length of the WALP peptide matches the thickness of the lipid bilayers (MTSL-WALP23/DOPC), the membrane spanning peptide is well registered in membrane and the hydrophobic profile could be readily fitted with a symmetric, continuous function (Equation 2.3) according to Marsh *et al*<sup>38</sup>. The same peptide experiencing a hydrophobic mismatch in DLPC bilayers shows a significantly altered  $A_{zz}$  profile, that is supposed to be caused by a mismatch-induced peptide aggregation and

associated displacement of the central amino acid residue from the center of the bilayer.

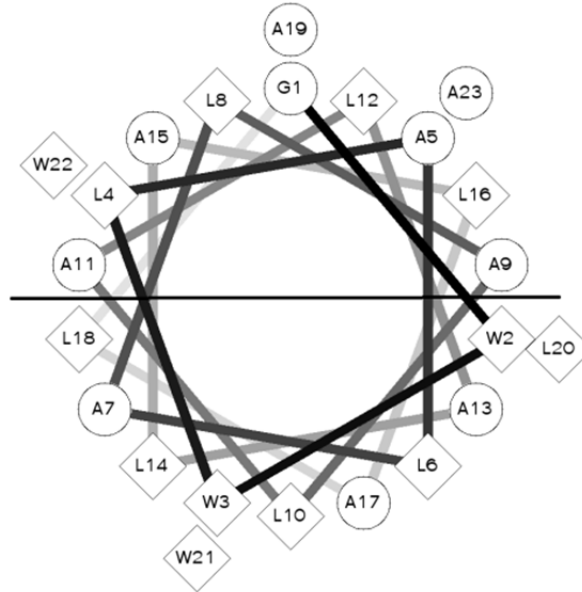


**Figure B7** Helical wheel projection for WALP23 peptide. Residues above the solid line seems to belong to the peptide face involved into association with another peptide molecule. Hydrophilic residues are shown as circles; hydrophobic residues are shown as diamonds; potentially negatively charged residues are shown as triangles, and potentially positively charged residues are shown as pentagons. The diagram is prepared using website created by Don Armstrong and Raphael Zidovetzki<sup>141</sup>.

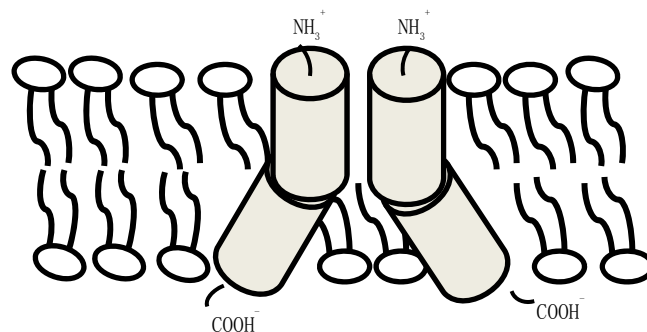


**Figure B8.** A cartoon illustrates the proposed arrangement of the N-terminal and C-terminal domains of the WALP23 peptide in the DLPC bilayers.

We propose a model that is supposed to explain the experimental observations (Figure B8). Thus, as a result of the hydrophobic mismatch the peptide acquires a kink that divides the backbone for the two almost equal parts having different tilt with respect to the bilayer interface – the C-half (close to the C-terminus) with a larger tilt, and the N-half with a smaller tilt. This is in accordance with the NMR data suggesting that the N-terminus of WALP23 peptide in DLPC bilayers has a large tilt ( $20^\circ$ ) than the C-terminus ( $7^\circ$ )<sup>152</sup>. The smaller tilt of the N-terminus is expected to allow for a more tight packing thus providing the condition for the helices to associate. Our oxygen accessibility data (Figure B4 (B)) indicate that unlike in DOPC lipids, in DLPC the center of the peptide (12<sup>th</sup> amino acid residue) does not coincide with the center of the bilayer and shifted toward the bilayer interface so the 10<sup>th</sup> amino acid residue located in the center of the bilayer; these results are consistent with the results of NMR studies<sup>152</sup>. Note that unlike the data for the C-terminus, the data for N-terminus deviate significantly from the bell-shaped profile (Figure B4 (B)). This is most

likely because of stronger packing of the N-half of the peptide so the oxygen accessibility data report on the contacts between the labeled sites and the more polar peptide backbones. For the less tightly packed C-half the oxygen accessibility data report on the interface between the peptide and the lipid acyl chains affording a more continuous trend following the bell-shaped profile. The  $A_{zz}$  data reporting on the polarity nearby the labeled site demonstrate a rather irregular pattern (Figure B6); it could be seen that some positions report on a more polar, and some – on a less polar, than for WALP23/DOPC, environment. We speculate that this results from the combination of the two effects – the interaction (association) of the helices and the displacement of the peptide with respect to the center of the bilayer.

### **B.3 Conclusion**

In this chapter, we carried out a series of EPR experiments with a well-studied spin-labeled WALP23 peptide to create a benchmark for our further EPR experiments with the CesA TMH peptides. Both pSR and linewidth ( $T_2$ ) oxygen profiles acquired in this lab agree well with the reported literature data<sup>28</sup>. Polarity profile acquired for WALP23 peptide in the DOPC bilayers also show a very good agreement with the oxygen accessibility profiles. The oxygen accessibility and polarity measurements carried out for WALP23 peptide in DLPC bilayers (hydrophobic mismatch case) were necessary to correctly interpret the EPR data complicated by the peptide aggregation. Based on the oxygen accessibility and polarity data for the WALP23 peptide in DLPC bilayers a model that describes the peptides' transmembrane arrangement was proposed.

The kinetics of the reduction of SL-WALP23 in DOPC bilayers with ascorbic acid at

neutral and acidic pH was studied by EPR to establish the reference profiles for the reduction experiments with the spin-labeled CesA TMHs. The two reduction kinetic profiles confirm that the bilayer penetration of ascorbic acid at pH = 3.3 (neutral species) compared to that at pH = 7.0 (anionic species). These profiles serve as a benchmark for the reduction of spin-labeled transmembrane non-aggregated peptides. The comparison of the reduction kinetic profiles of SL-WALP23 and SL-TMH5 in the lipid bilayers of the same composition allowed us to shed a light on the details of the membrane arrangement of the latter.

## **Appendix C      Reconstitution of CesaA TMH5 to Nanodiscs for EPR Study**

### **C.1 Introduction**

As it was shown in the previous chapters, although the CesaA TMH5 peptide do insert into the lipid bilayers, they also show a high tendency to aggregation under a broad range of conditions. The nanodiscs, originally developed by Sligar and coworkers in 2002, could be a solution to this problem. Owing to the controlled size of the nanodiscs, they provide only limited space for the insertion of the peptide/protein and were expected to force TMHs to insert in their individual, unaggregated form. This technique has already proved that single molecule of the integral membrane protein could be reconstituted into nanodiscs, making solubilization of membrane proteins much feasible<sup>158</sup>.

Nanodiscs are discoidal nanoscale phospholipid bilayers wrapped up around the edges of the hydrophobic acyl chains of each leaflet by the two molecules of amphipathic membrane scaffold protein (MSP) (Figure C1). In this project, we employed MSP1 to limit the nanodiscs diameter at about 10 nm which is the smallest size of the nanodiscs reported so far. There are two reasons to choose MSP1. First, we want to keep the nanodiscs as small as possible since the cross section of a single transmembrane  $\alpha$ -helix peptide is only around 1nm. A larger diameter of the nanodisc may provide the room for peptide aggregation. Secondly, it is important to keep enough phospholipid molecules surrounding the peptide backbone, typically at least 50 lipid molecules per one peptide helix, to maintain a native environment for transmembrane peptide. The nanodiscs wrapped by MSP1 are well suitable since the number of the lipid molecules they are bearing was calculated to be between 120 and 160 per nanodisc, depending on the size of the lipid polar head group.

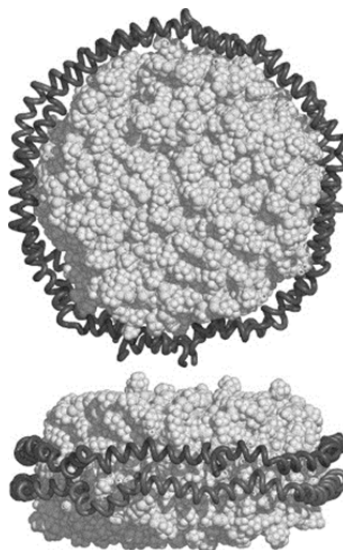


**Figure C1.** This cartoon illustrates the structure of nanodiscs (generated by the PyMOL Molecular Graphics system) modeled using POPC as a lipid. White space filling represents the lipid bilayer and two amphipathic helices of MSP are shown as gray ribbons<sup>159</sup>.

## C.2 Expression and Purification of MSP1

The MSP is engineered based upon the sequence of human serum apolipoprotein AI<sup>159</sup>. MSP1 is the first one being utilized to assemble the nanodiscs and its plasmid is commercially available. This protein contains an N-terminal hexahistidine tag, a protease site as a linker, and the main MSP sequences which contain 10  $\alpha$ -helical segments:

```
MGHHHHHHIEGRLKLLDNWDSVTSTFSKLREQLGPVTQEFWDNLEKETEGLRQEMS
KDLEEVKAKVQPYLDDFQKKWQEEMELYRQKVEPLRAELQEGARQKLHELQEKLS
PLGEEMRDRARAHVDALRTHLAPYSDELQRQLAARLEALKENGGARLAEYHAKAT
EHLSTLSEKAKPALEDLRQGLLPVLESFKVSFLSALEEYTKKLNTQ.
```

The expression of MSP1 was carried out as previously reported with minor

modification<sup>160</sup>. The constructed plasmid in *E. coli* was kindly provided by Prof. Tian from Penn State University. Briefly, 10 mL LB medium containing 50 µg/mL kanamycin were inoculated with single colony from a fresh plate and the culture grown at 37 °C with shaking at 250 rpm until OD<sub>600</sub> reached 0.6-0.8 after about 5 hours. The starting culture was stored at 4 °C overnight. On the following morning, the culture was poured into 1 L sterilized TB-medium containing 10 µg/mL kanamycin and incubated at 37 °C with shaking at 250 rpm. After 4-5 hours when OD<sub>600</sub> reached 2.5-3.0, induction with 1mM IPTG was performed, and the temperature was adjusted to 28 °C one hour after induction. The cells were collected 4 hours after induction by centrifugation at 4000 rpm for 30 min and stored at -80 °C.

To purify MSP1, the cells collected from 1 L culture were re-suspended in 20 mM sodium phosphate buffer pH = 7.4 containing 1mM PMSF and 1% Triton X-100 and lysed by probe sonicator. The mixture was centrifuged at 30000 g for 30 min at 4 °C to obtain clear lysate, and then equilibrate with 2 mL HisPur™ Ni-NTA resin overnight. The resin was washed with 3 bed volumes of each following buffers<sup>161</sup>: (1) 0.1 M sodium phosphate buffer , 0.3 M NaCl, pH = 7.4; (2) 0.1 M sodium phosphate buffer , 0.15 M NaCl, pH = 7.4; (3) 0.1 M sodium phosphate buffer , pH = 7.4; MSP1 was eluted by 0.1 M sodium phosphate buffer, 50 mM imidazole, pH = 7.4. The collected fraction was examined by UV-vis A<sub>280</sub>) and the purity was checked using polyacrylamide gel electrophoresis (SDS, 4%), Figure C4. The fractions containing MSP1 were pooled and dialyzed against 10 mM Tris/HCL, 0.1 M NaCl, 1mM EDTA, pH = 7.4 in the cold room for 2 days with buffer changed twice a day. The protein concentration was determined by A<sub>280</sub>, extinction coefficient  $\epsilon=23950 \text{ M}^{-1}\text{cm}^{-1}$ .<sup>159</sup> The identity of MSP1 was also confirmed by MALDI-TOF/TOF mass spectrometry. A

solution of the protein in water was spotted onto the MALDI (positive ion mode) plate along with the matrix (sinapic acid in 50% acetonitrile/50% water/0.1% TFA).

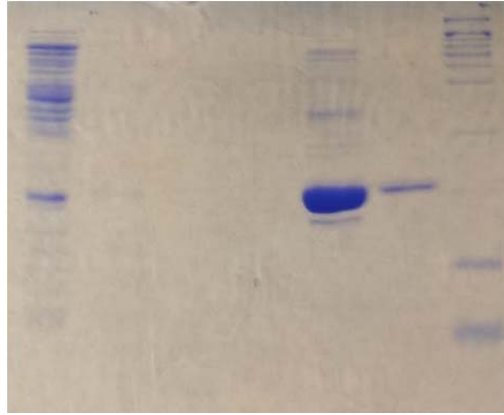


**Figure C2.** SDS-page of MSP1 purification fractions. Lane 1: cell lysis after Ni-NTA binding; Lane 2: Equilibrium; Lane 3: Washing 1; Lane 4: Washing 2; Lane 5: Elution 1; Lane 6: Elution 2; Lane 7: Ladder (Protein Molecular Weight Standards (broad range) (Novex®) P-6649).

### **C.3 Self-Assembly, purification and characterization of POPC nanodiscs**

POPC was chosen as a candidate to assemble the nanodiscs using purified MSP1; application of this phospholipid is well documented in the literature. The literature experimental procedure with minor modifications was used. 20% (w/v) POPC lipid vesicles were first prepared as described here. A chloroform solution of POPC (Avanti Polar Lipids, Alabaster, AL) was placed into a conical vial and chloroform was removed by N<sub>2</sub> flow followed by vacuum desiccation overnight. The lipid film was hydrated with a required buffer solution. The multilamellar vesicles were formed using 10 consecutive freeze-thaw

cycles between liquid nitrogen and 37 °C water bath, followed by vortexing. Purified MSP1 protein and POPC vesicles were then co-dissolved at 1:70 molar ratio in a buffer containing cholate. The mixture was equilibrated under room temperature for 1 hour. Cholate was removed by Biobeads SM2 in the cold room overnight with gentle agitation. During this step, the self-assembly of nanodiscs was initiated. The Biobeads were removed by brief centrifugation. The sample was purified by size exclusion chromatography (SEC) using a Sephacryl S-300 16/60 column, flow rate of 1 mL/min, and 0.5 M sodium phosphate containing 0.15 M NaCl, pH = 7.2, as an eluent. The absorbance was continuously monitored at 280nm.

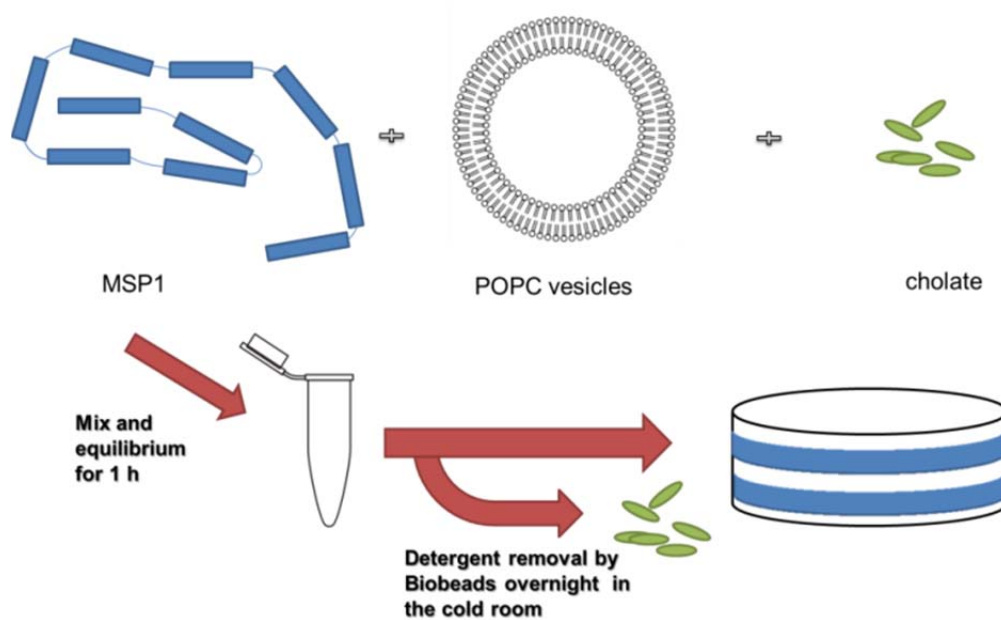


**Figure C3.** Cartoon illustrates the preparation of nanodiscs.

POPC nanodiscs eluted with a shoulder peak (Figure C4 (A)) as reported<sup>162</sup>. The first sharp peak eluted at about 40 mL contained large aggregates of MSP1 and POPC lipids. The particle sizes of the fractions collected from the main peak were characterized by dynamic light scattering (DLS) (Figure C4 (B)). The particle size was found to be  $11.5 \pm 3.1$  nm. There is slightly different from the reported 9.8nm measured by small-angle x-ray scattering<sup>162</sup>. This is most likely because the volume distribution was calculated from the intensity distribution assuming that particles are spherical, which is not true for discoidal nanodiscs.

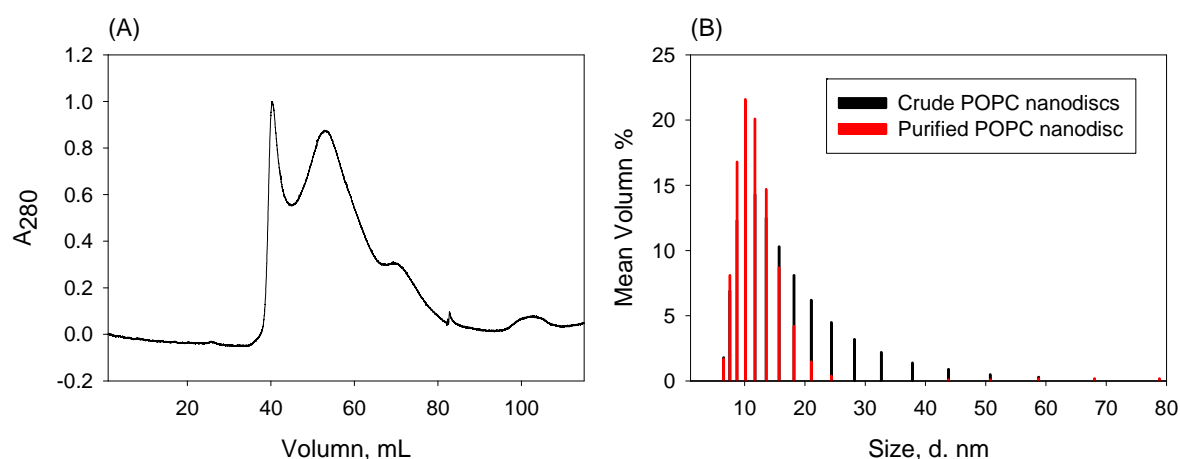


**Figure C4.** Characterization of POPC nanodiscs. (A): SEC purification of POPC nanodiscs. The elution profile was normalized to maximum absorbance at 280 nm. (B): Dynamic light scattering size distribution for the mixture of POPC nanodiscs (black) and after chromatography (red).

#### **C.4 Self-Assembly, purification and characterization of DOPC nanodiscs**

For the reconstitution of TMHs, the nanodiscs containing DOPC lipids were prepared (for the discussion of the lipid composition suitable for TMHs reconstitution, see previous Chapters). It has been shown, that the lipid-to-MSP stoichiometry is critical in the process of self-assembly of nanodiscs with homogenous size<sup>160</sup>. Even if the ratio is slightly off the optimal, the aggregation will occur as seen the size exclusion chromatography. If ratio is far from the optimum, a broad nanodiscs size distribution will be observed. Therefore, the optimal lipid-to-MSP ratio has to be found when the new lipid composition is employed. In order to find this ratio, we titrated MSP1 with DOPC lipids at 1:100, 1:70, 1:50 (MSP1: lipid) ratio. The elution profiles of both 1:100 and 1:70 showed the formation of aggregates that were eluted at about 40 mL (Figure C5). However, the DOPC nanodiscs assembled at 1:50 (MSP1: lipid) ratio gave mostly homogenous particle distribution as indicated by SEC elution profile (Figure C6 (A)) with the elution volume at about 55 mL. The fractions collected from main peak were pooled and the particle size was characterized by DLS (Figure C6 (B)) as  $14.4 \pm 3.7$  nm. The size of DOPC nanodiscs is slightly larger than that of POPC nanodiscs. The protein-to-lipid ratio higher than 1:50 was not tested.

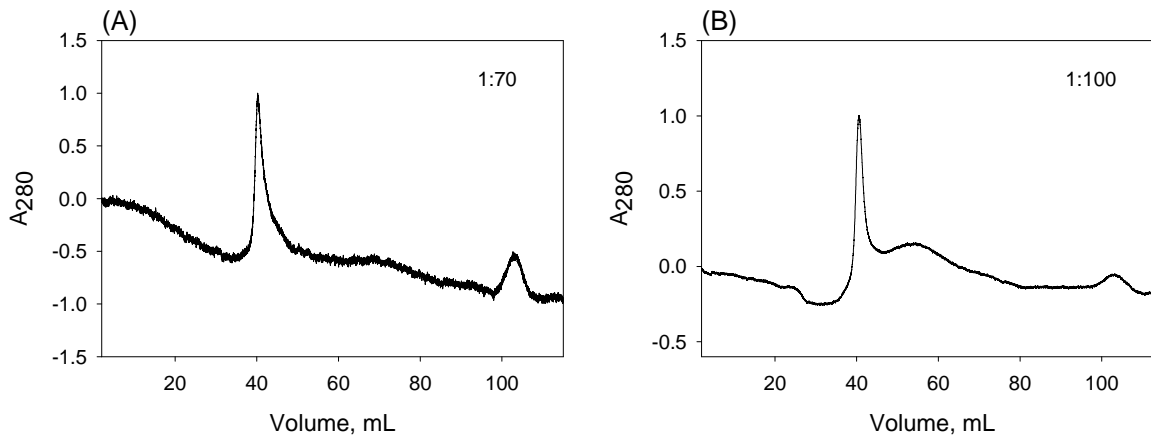


**Figure C5.** SEC purification of DOPC nanodiscs obtained at MSP1-to-DOPC molar ratio of 1:70 (A) and 1:100 (B). The elution profile was normalized to maximum absorbance at 280 nm.

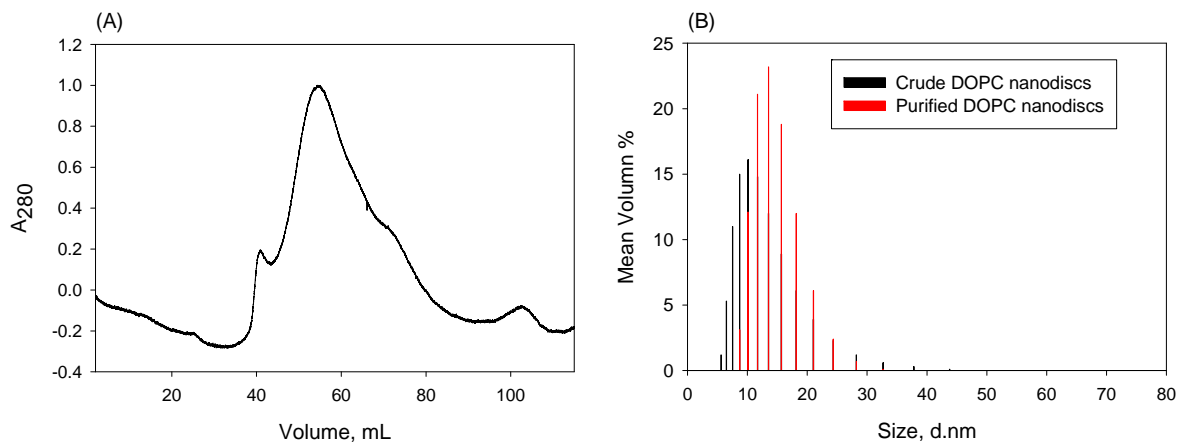


**Figure C6.** Characterization of DOPC nanodiscs. (A): SEC purification of DOPC nanodiscs (MSP1:DOPC = 1:50). The elution profile was normalized to maximum absorbance at 280 nm. (B): DLS reported size distribution of DOPC nanodiscs assembly mixture (black) and main peak collected from chromatography, i.e. the purified DOPC nanodiscs (red).

## **C.5 Self-Assembly, purification and characterization of DOPC nanodiscs containing SL-TMH5 peptide**

### **C.5.1 Reconstitution of SL-TMH5 peptide into the nanodiscs**

To incorporate the MTSL-labeled CesaA TMH5 the latter was included into the nanodiscs assembly mixture. Spin-labeling of TMH5 was carried out in water-miscible tetrafluoroethanol (TFE) containing trace amounts of trifluoroacetic acid and triethylamine that were expected to be removed by Biobeads along with cholate; thus, first we tried to directly mix the peptide in TFE solution with the assembly mixture. However, both the elution profile and particle size distribution measured by DLS showed that the nanodiscs with required size were not formed. Thus, SEC showed no peaks at about 50 mL elution volume (Figure C7, black trace). DLS measured for the two fractions eluted at about 40 mL and 70 mL yielded  $37.1 \pm 25.3$  nm and  $8.92 \pm 7.08$  nm, respectively (data not shown). The size distribution for the nanodisc assembly mixture was found to be much wider compared to that for empty DOPC nanodiscs at the same MSP: DOPC molar ratio (Figure C8 (A)).

Therefore, an alternative protocol was developed. The solvents from the peptide labeling reaction mixture were removed under N<sub>2</sub> flow to give a thin film of SL-TMH5 peptide. The nanodisc assembly mixture was added with a pipette to the vial to dissolve the film of SL-TMH5. The rest of the procedure remains the same as described above. The size distribution for the assembly mixture was found to be much narrower compared to that of the one prepared in the presence of TFE and close to that observed for empty nanodisc assembly mixture. The size of the particles collected from the fraction eluted at about 50 mL elution volume (Figure C7, red trace) was found to be  $12.4 \pm 7.1$  nm (Figure C8 (B)), which is

comparable with the size of empty DOPC nanodiscs. Based on this observation, we concluded that the presence of organic solvents seems to impede the nanodisc assembly.

We also tried to mix the reagents in different order. Thus, we first mixed a TFE solution of the SL-TMH5 peptide with a chloroform solution of DOPC. Organic solvents were removed under N<sub>2</sub> flow; the residue was incubated in a vacuum desiccator overnight and rehydrated along with the DOPC nanodiscs forming vesicles. The rest of the procedure remains the same as described previously. However, according to the FPLC elution profile, there was no significant improvement observed (data not shown). Therefore, the SL-TMH5 DOPC nanodiscs were prepared according to the second protocol described above, unless otherwise stated.

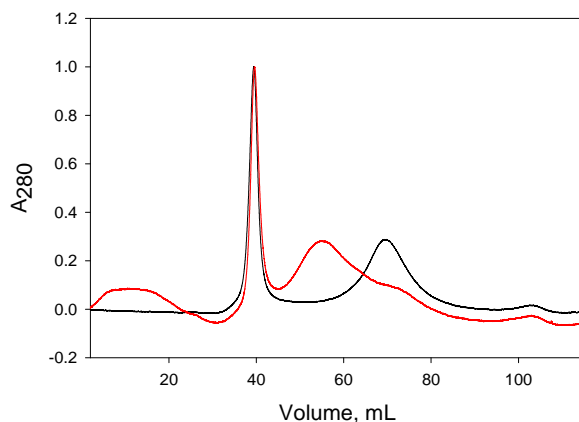


**Figure C7.** SEC purification of DOPC nanodiscs (MSP1:DOPC lipids = 1:50) assembly mixture containing MTSL labeled CesaA TMH5 L13. The MSP1:peptide ratio was 2:1. The elution profile was normalized to maximum absorbance at 280 nm. (black trace): The spin-labeled peptide was introduced into DOPC nanodiscs in the presence of TFE and (red trace) in the absent of TFE.

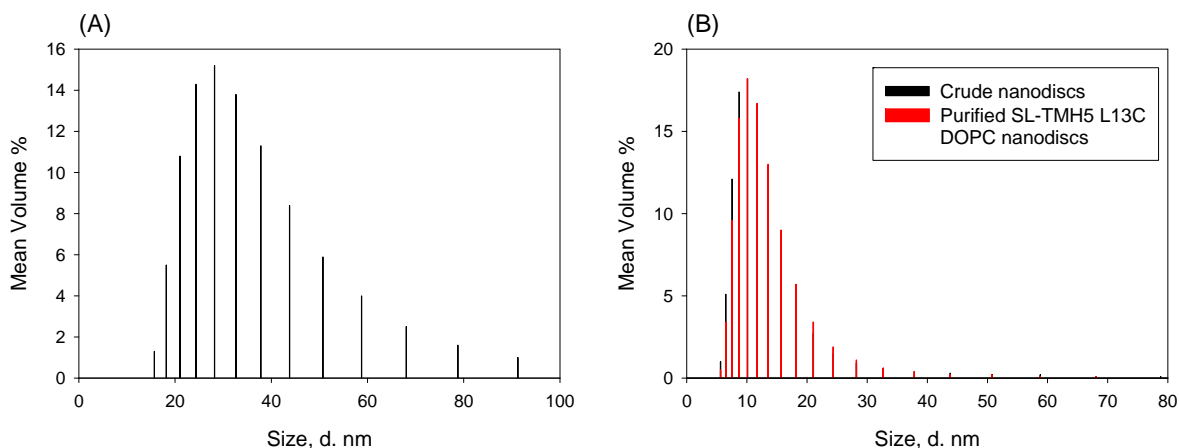


**Figure C8.** Dynamic light scattering size distribution for MTSL-labeled Cesa TMH5 L13 DOPC nanodiscs with peptide introduced with TFE ((A); for the elution profile see Figure C7, black trace) and without TFE ((B), black, for the elution profile see Error! Reference source not found., red trace). The DLS data for the purified nanodiscs containing TMH5 are shown in red (B).

### C.5.2 Lipid to MSP ratio when MTSL-Cesa TMH5 incorporated into nanodiscs

To overcome the self-aggregation of protein assembled into nanodiscs, a high MSP to target protein ratio has been suggested<sup>158</sup>. We tested the nanodiscs prepared at 2:1, 4:1 and 8:1 MSP1:TMH5 ratio (lipid-to-MSP1 ratio was kept at 50:1), but the EPR spectra showed that all the samples contained a fraction of the aggregated peptide. An example of the EPR spectrum of aggregated MTSL-TMH5 L13C variant incorporated in DOPC nanodiscs is shown in Figure C9.

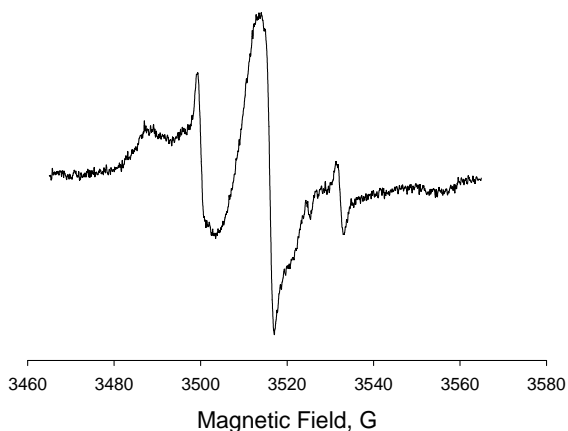


**Figure C9.** Room temperature X-band EPR spectrum of MTSL labeled CesA TMH5 L13 DOPC nanodiscs, pH = 7.0. MSP1:peptide molar ratio was 2:1. Lipid: peptide ratio was 50:1. Spectrum indicates that the labeled TMH5 is mostly aggregated in the nanodiscs.

A certain amount of lipid molecules will be replaced by the peptide molecules, decreasing the number of lipid molecules per nanodiscs, so the lipids-to-MSP ratio has to be further optimized. When the lipids-to-MSP ratio was decreased to 40:1, two well-resolved peaks were observed on the SEC elution profile (Figure C10 (A)). EPR spectra of both fractions (eluted at about 50 mL and 60 mL) are shown in Figure C11. The fraction eluted at *ca.* 50 mL (A) contains aggregated peptide (Figure C11 (A)), and its DLS (Figure C10 (B)), blue lines) showed the larger nanodiscs size ( $13.6 \pm 4.9$  nm) compared to the fraction eluted at about 60 mL ( $10.4 \pm 3.0$  nm, Figure C10 (B), red lines). The EPR spectrum of the fraction containing smaller nanodiscs (Figure C11 (B)) revealed the EPR lineshape of a typical non-aggregated spin-labeled peptide reconstituted to the lipid bilayer.

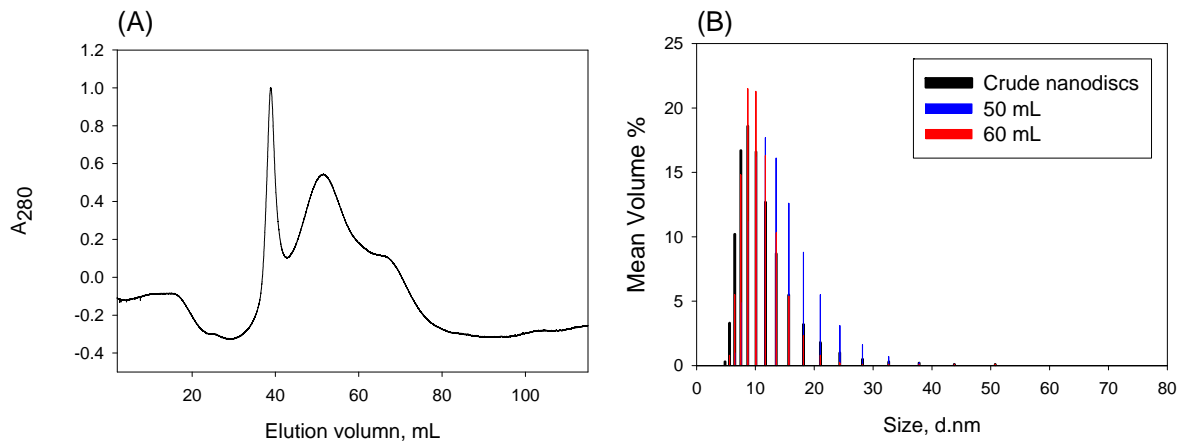


**Figure C10.** Characterization of MTSL-CesA TMH5 L13C peptide reconstituted into DOPC nanodiscs. (A): SEC purification of DOPC nanodiscs (MSP1: DOPC lipids = 1:40) assembly mixture containing MTSL labeled CesA TMH5 L13C. The MSP1:peptide ratio was 5:1. The elution profile was normalized to maximum absorbance at 280 nm. (B) Dynamic light scattering size distribution for MTSL labeled CesA TMH5 L13/DOPC nanodiscs assembly mixture (black). The size distribution for purified fractions of MTSL labeled CesA TMH5 L13/DOPC nanodiscs (blue, fraction collected at 50 mL), (red, fraction collected at 60 mL).

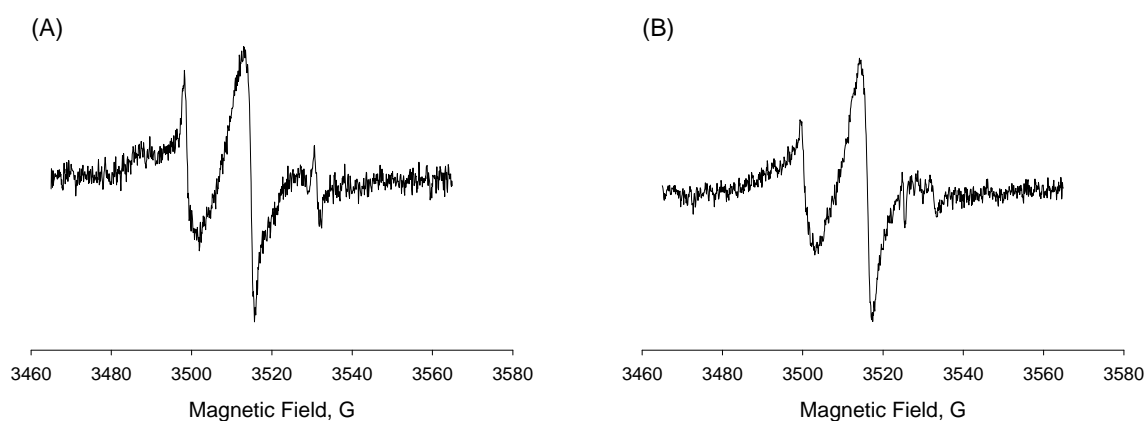


**Figure C11.** Room temperature X-band EPR spectrum of the purified fractions collected at about 50 mL (A) and 60 mL (B) for MTSL labeled CesA TMH5 L13/DOPC nanodiscs, pH = 7.0. MSP1: peptide molar ratio was 5:1.

## C.6 Conclusions

The protocol for CesATMH5 assembly into DOPC nanodiscs was established. The purpose of using nanodiscs was to reconstitute TMH5 peptide into dispersed nanodisc bilayers, thereby promoting disaggregation of TMH. According to the SEC profile and the EPR spectra, the DOPC nanodiscs contain the fraction of disaggregated SL-TMH5 L13C peptide; however, the majority of the peptide was found to be reconstituted in oligomerized form. Considering the preparation efforts and the cost of the materials, this technique is not suitable for biophysical studies of small aggregating peptides, such as CesA TMH peptides.

## Appendix D EPR Power Saturation Experiments at 77K

The goal of this section is to determine a microwave power level for 77K EPR studies to avoid saturation of EPR signal at 77K. For this purpose, the magnitude of the anisotropic nitrogen hyperfine coupling constant  $A_{zz}$  was measured as the function of the square root (sqrt) of incident microwave power ( $B_1$ ) at 77K. WALP23 peptides spin-labeled at 12<sup>th</sup>, 16<sup>th</sup>, or 23<sup>rd</sup> positions reconstituted into DOPC bilayers were employed in this study. The plot of  $A_{zz}$  against sqrt of  $B_1$  is shown in Figure D1. With  $B_1$  increasing, the  $A_{zz}$  values were found to decrease non-linearly with  $A_{zz}$  for SL-WALP23-16 and -12 reaching the “plateau” at sqrt of  $B_1$  of approximately 6 a.u., while continuing to decrease for SL-WALP23-23.

We hypothesize that the dependence of apparent  $A_{zz}$  on  $B_1$  could be related to different relaxation properties of hydrogen-bonded and non-hydrogen-bonded nitroxides. To test this hypothesis, we carried out the 77 K power saturation experiments using 1mM solutions of MTSL in water/glycerol (1:40 v/v) mixture (hydrogen bonded nitroxide) and toluene (non-hydrogen bonded nitroxide), respectively. The two well-distinguishable  $A_{zz}$  vs. sqrt of  $B_1$  plots for both solvents are shown in Figure D2. For a solution in water/glycerol, the plot demonstrates a rather steep slope; if the incident microwave power increases from 45 to 5 dB ( $6.2346 \times 10^{-3}$  to 63.246 mW), the  $A_{zz}$  decreases for about 6 G (from 36.325 to 30.187 G). For the same nitroxide in a toluene solution, the  $A_{zz}$  vs. sqrt of  $B_1$  plot demonstrates a much more gradual slope. Thus, for the same microwave power range, the  $A_{zz}$  in toluene drops for only 1.3 G (from 33.9145 to 32.569 G). Thus, our experimental observations support our hypothesis on the significant effect of the applied microwave power on the

relaxation properties of the hydrogen-bonded nitroxides.

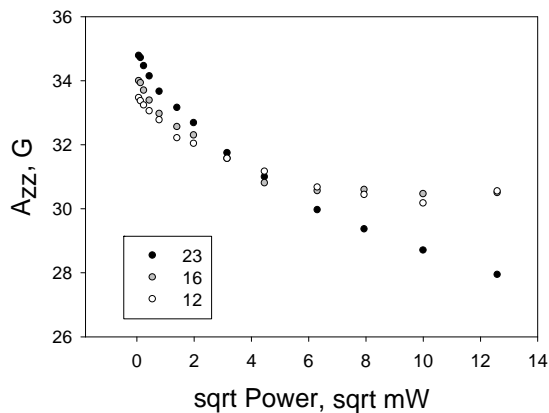


**Figure D1.** An  $A_{zz}$  vs.  $B_1$  plots for MTSL-WALP peptides embedded into DOPC membrane at 77K. The positions of labeling are indicated in the inset.

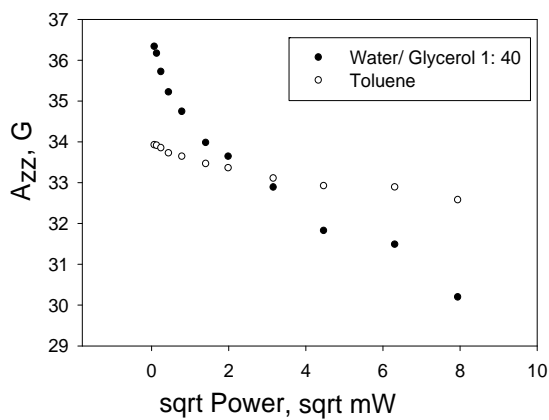


**Figure D2.** An  $A_{zz}$  vs.  $B_1$  plots for 1mM MTSL in a frozen glass (water-glycerol mixture at 40:1 v/v ratio) and in toluene at 77K. The solvents are indicated in the inset.

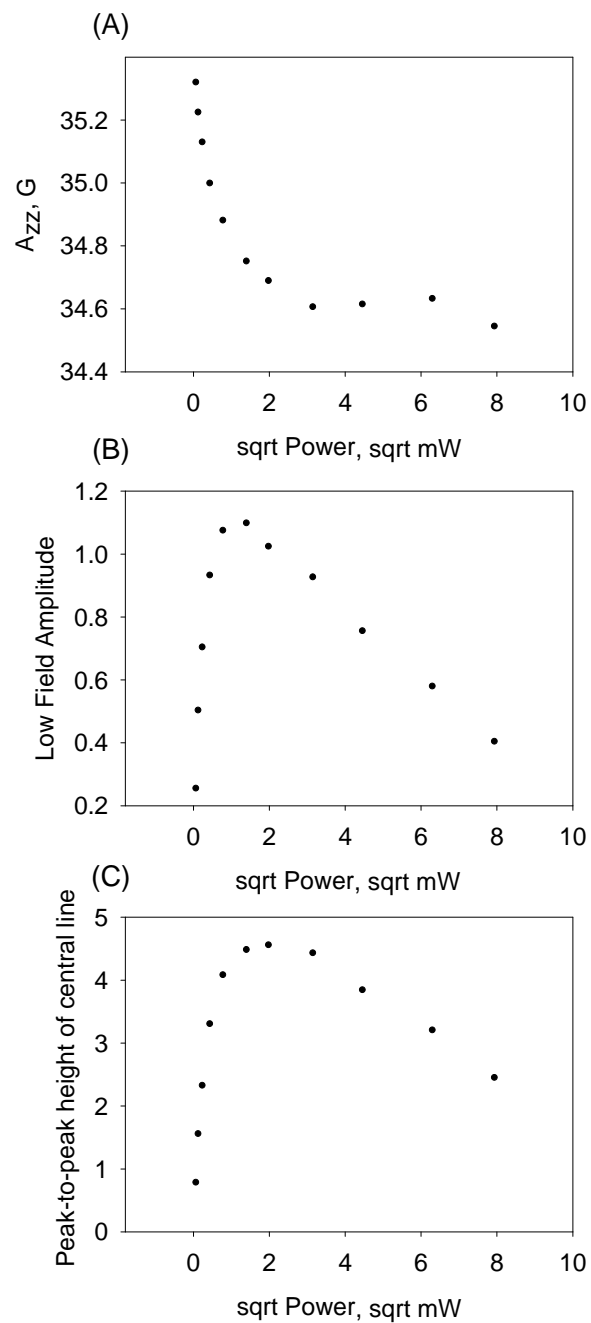


**Figure D3.** (A) An  $A_{zz}$  vs.  $B_1$  plot for 1mM PDT in isopropanol- $d_8$  at 77K. The corresponding power saturation curves for the low-field component (B) and the central component (B) for 1mM PDT in an isopropanol- $d_8$  at 77K.

## Appendix E      References

1. Singer, S. J.; Nicolson, G. L.,The fluid mosaic model of the structure of cell membranes. *Science* **1972**, *175* (23), 720-731.
2. Popot, J.-L.; Engelman, D. M.,Membrane protein folding and oligomerization: the two-stage model. *Biochemistry* **1990**, *29* (17), 4031-4037.
3. von Heijne, G.; Rees, D.,Membranes: reading between the lines. *Current opinion in structural biology* **2008**, *18* (4), 403-405.
4. Boyd, D.; Schierle, C.; Beckwith, J.,How many membrane proteins are there? *Protein Science* **1998**, *7* (1), 201-205.
5. Tanford, C., *The Hydrophobic Effect: Formation of Micelles and Biological Membranes 2d Ed.* J. Wiley.: 1980.
6. Rees, D.; DeAntonio, L.; Eisenberg, D.,Hydrophobic organization of membrane proteins. *Science* **1989**, *245* (4917), 510-513.
7. White, S. H.; Wimley, W. C.,Peptides in lipid bilayers: structural and thermodynamic basis for partitioning and folding. *Current Opinion in Structural Biology* **1994**, *4* (1), 79-86.

8. Finkelstein, A., Water movement through lipid bilayer, pores and plasma membranes. *Theory and Reality* **1987**, 4.
9. Brown, B. S., *Biological membranes*. Biochemical Society: 1996.
10. Wallin, E.; Heijne, G. V., Genome - wide analysis of integral membrane proteins from eubacterial, archaean, and eukaryotic organisms. *Protein Science* **1998**, 7 (4), 1029-1038.
11. White, S. H. The Stephen White laboratory at UC Irvine latest membrane protein structures database. [http://blanco.biomol.uci.edu/Membrane\\_Proteins\\_xtal.html](http://blanco.biomol.uci.edu/Membrane_Proteins_xtal.html). (accessed 5/27/2014).
12. White, S. H., The progress of membrane protein structure determination. *Protein Science* **2004**, 13 (7), 1948-1949.
13. Fanucci, G. E.; Cafiso, D. S., Recent advances and applications of site-directed spin labeling. *Current opinion in structural biology* **2006**, 16 (5), 644-653.
14. Wang, H.-L.; Cheng, X.; Sine, S. M., Intramembrane proton binding site linked to activation of bacterial pentameric ion channel. *Journal of Biological Chemistry* **2012**, 287 (9), 6482-6489.
15. Oh, K. J.; Altenbach, C.; Collier, R. J.; Hubbell, W. L., Site-Directed Spin Labeling of

Proteins. In *Bacterial Toxins: Methods and Protocols*, Springer: 2000; pp 147-169.

16. Mchaourab, H. S.; Lietzow, M. A.; Hideg, K.; Hubbell, W. L., Motion of spin-labeled side chains in T4 lysozyme. Correlation with protein structure and dynamics. *Biochemistry* **1996**, *35* (24), 7692-7704.

17. Delmer, D. P., Cellulose biosynthesis: exciting times for a difficult field of study. *Annual review of plant biology* **1999**, *50* (1), 245-276.

18. Glaser, L., The synthesis of cellulose in cell-free extracts of *Acetobacter xylinum*. *Journal of Biological Chemistry* **1958**, *232* (2), 627-636.

19. Morgan, J. L.; Strumillo, J.; Zimmer, J., Crystallographic snapshot of cellulose synthesis and membrane translocation. *Nature* **2013**, *493* (7431), 181-186.

20. Slabaugh, E.; Davis, J. K.; Haigler, C. H.; Yingling, Y. G.; Zimmer, J., Cellulose synthases: new insights from crystallography and modeling. *Trends in plant science* **2013**.

21. Richmond, T., Higher plant cellulose synthases. *Genome Biol* **2000**, *1* (4), 3001.1-3001.6.

22. Haigler, C. H.; Blanton, R. L., New hope for old dreams: evidence that plant cellulose synthase genes have finally been identified. *Proceedings of the National Academy of*

*Sciences of the United States of America* **1996**, 93 (22), 12082.

23. Sethaphong, L.; Haigler, C. H.; Kubicki, J. D.; Zimmer, J.; Bonetta, D.; DeBolt, S.; Yingling, Y. G., Tertiary model of a plant cellulose synthase. *Proceedings of the National Academy of Sciences* **2013**, 110 (18), 7512-7517.

24. Atkins, P.; Paula, J., *Physical Chemistry*, 8th. Oxford University Press: Oxford: 2006.

25. Wertz, J. E.; Bolton, J. R., *Electron spin resonance: elementary theory and practical applications*. Chapman and Hall: 1972.

26. Altenbach, C.; Froncisz, W.; Hemker, R.; Mchaourab, H.; Hubbell, W. L., Accessibility of nitroxide side chains: absolute Heisenberg exchange rates from power saturation EPR. *Biophysical journal* **2005**, 89 (3), 2103-2112.

27. Hubbell, W. L.; Altenbach, C., Investigation of structure and dynamics in membrane proteins using site-directed spin labeling. *Current Opinion in Structural Biology* **1994**, 4 (4), 566-573.

28. Nielsen, R. D.; Che, K.; Gelb, M. H.; Robinson, B. H., A ruler for determining the position of proteins in membranes. *Journal of the American Chemical Society* **2005**, 127 (17), 6430-6442.

29. Perozo, E.; Cortes, D. M.; Cuello, L. G., Three-dimensional architecture and gating mechanism of a K<sup>+</sup> channel studied by EPR spectroscopy. *Nature Structural & Molecular Biology* **1998**, *5* (6), 459-469.
30. Farahbakhsh, Z. T.; Altenbach, C.; Hubbell, W. L., Spin labeled cysteines as sensors for protein - lipid interaction and conformation in rhodopsin. *Photochemistry and photobiology* **1992**, *56* (6), 1019-1033.
31. Pyka, J.; Ilnicki, J.; Altenbach, C.; Hubbell, W. L.; Froncisz, W., Accessibility and dynamics of nitroxide side chains in T4 lysozyme measured by saturation recovery EPR. *Biophysical journal* **2005**, *89* (3), 2059-2068.
32. Altenbach, C.; Greenhalgh, D. A.; Khorana, H. G.; Hubbell, W. L., A collision gradient method to determine the immersion depth of nitroxides in lipid bilayers: application to spin-labeled mutants of bacteriorhodopsin. *Proceedings of the National Academy of Sciences* **1994**, *91* (5), 1667-1671.
33. Killian, J. A.; Salemink, I.; de Planque, M. R.; Lindblom, G.; Koeppe, R. E., 2nd; Greathouse, D. V., Induction of nonbilayer structures in diacylphosphatidylcholine model membranes by transmembrane alpha-helical peptides: importance of hydrophobic mismatch and proposed role of tryptophans. *Biochemistry* **1996**, *35* (3), 1037-45.

34. Siegel, D.; Cherezov, V.; Greathouse, D.; Koeppe II, R.; Killian, J. A.; Caffrey, M., Transmembrane peptides stabilize inverted cubic phases in a biphasic length-dependent manner: implications for protein-induced membrane fusion. *Biophysical journal* **2006**, *90* (1), 200-211.
35. Alaouie, A. M.; Smirnov, A. I., Ultra-stable temperature control in EPR experiments: thermodynamics of gel-to-liquid phase transition in spin-labeled phospholipid bilayers and bilayer perturbations by spin labels. *Journal of Magnetic Resonance* **2006**, *182* (2), 229-238.
36. Smirnov, A. I.; Clarkson, R.; Belford, R., EPR Linewidth ( $t_2$ ) method to measure oxygen permeability of phospholipid bilayers and its use to study the effect of low ethanol concentrations. *Journal of Magnetic Resonance, Series B* **1996**, *111* (2), 149-157.
37. Dzikovski, B. G.; Livshits, V. A.; Marsh, D., Oxygen permeation profile in lipid membranes: comparison with transmembrane polarity profile. *Biophysical journal* **2003**, *85* (2), 1005-1012.
38. Marsh, D.; Dzikovski, B. G.; Livshits, V. A., Oxygen profiles in membranes. *Biophysical journal* **2006**, *90* (7), L49-L51.
39. Mutwil, M.; Debolt, S.; Persson, S., Cellulose synthesis: a complex complex. *Current opinion in plant biology* **2008**, *11* (3), 252-257.

40. Grishammer, R.; Tateu, C., Overexpression of integral membrane proteins for structural studies. *Quarterly reviews of biophysics* **1995**, *28* (03), 315-422.
41. Fleishman, S. J.; Ben-Tal, N., Progress in structure prediction of  $\alpha$ -helical membrane proteins. *Current opinion in structural biology* **2006**, *16* (4), 496-504.
42. Arinaminpathy, Y.; Khurana, E.; Engelman, D. M.; Gerstein, M. B., Computational analysis of membrane proteins: the largest class of drug targets. *Drug discovery today* **2009**, *14* (23), 1130-1135.
43. Liang, J.; Naveed, H.; Jimenez-Morales, D.; Adamian, L.; Lin, M., Computational studies of membrane proteins: Models and predictions for biological understanding. *Biochimica et Biophysica Acta (BBA)-Biomembranes* **2012**, *1818* (4), 927-941.
44. Senes, A., Computational design of membrane proteins. *Current opinion in structural biology* **2011**, *21* (4), 460-466.
45. Chen, K.-Y. M.; Sun, J.; Salvo, J. S.; Baker, D.; Barth, P., High-resolution modeling of transmembrane helical protein structures from distant homologues. *PLoS computational biology* **2014**, *10* (5), e1003636.
46. Opella, S. J., Structure determination of membrane proteins by nuclear magnetic resonance spectroscopy. *Annual Review of Analytical Chemistry* **2013**, *6*, 305-328.

47. Qureshi, T.; Goto, N. K., Contemporary methods in structure determination of membrane proteins by solution NMR. In *NMR of Proteins and Small Biomolecules*, Springer: 2012; pp 123-185.
48. Stahlberg, H.; Fotiadis, D.; Scheuring, S.; Rémygy, H.; Braun, T.; Mitsuoka, K.; Fujiyoshi, Y.; Engel, A., Two-dimensional crystals: a powerful approach to assess structure, function and dynamics of membrane proteins. *FEBS letters* **2001**, *504* (3), 166-172.
49. Saibil, H. R., Conformational changes studied by cryo-electron microscopy. *Nature Structural & Molecular Biology* **2000**, *7* (9), 711-714.
50. Scheuring, S.; Müller, D. J.; Stahlberg, H.; Engel, H.-A.; Engel, A., Sampling the conformational space of membrane protein surfaces with the AFM. *European Biophysics Journal* **2002**, *31* (3), 172-178.
51. Nazarov, P. V.; Koehorst, R.; Vos, W. L.; Apanasovich, V. V.; Hemminga, M. A., FRET study of membrane proteins: simulation-based fitting for analysis of membrane protein embedment and association. *Biophysical journal* **2006**, *91* (2), 454-466.
52. Nazarov, P. V.; Koehorst, R.; Vos, W. L.; Apanasovich, V. V.; Hemminga, M. A., FRET study of membrane proteins: determination of the tilt and orientation of the N-terminal domain of M13 major coat protein. *Biophysical journal* **2007**, *92* (4), 1296-1305.

53. Kang, G.; López-Peña, I.; Oklejas, V.; Gary, C. S.; Cao, W.; Kim, J. E., Förster resonance energy transfer as a probe of membrane protein folding. *Biochimica et Biophysica Acta (BBA)-Biomembranes* **2012**, *1818* (2), 154-161.
54. Förster, T., Energy migration and fluorescence. *Journal of biomedical optics* **2012**, *17* (1), 0110021-01100210.
55. Rieger, R.; Nienhaus, G. U., A combined single-molecule FRET and tryptophan fluorescence study of RNase H folding under acidic conditions. *Chemical Physics* **2012**, *396*, 3-9.
56. Zhang, Y.; Yang, X.; Liu, L.; Huang, Z.; Pu, J.; Long, G.; Zhang, L.; Liu, D.; Xu, B.; Liao, J., Comparison of Förster-Resonance-Energy-Transfer Acceptors for Tryptophan and Tyrosine Residues in Native Proteins as Donors. *Journal of fluorescence* **2013**, 1-11.
57. Mchaourab, H. S.; Steed, P. R.; Kazmier, K., Toward the fourth dimension of membrane protein structure: insight into dynamics from spin-labeling EPR spectroscopy. *Structure* **2011**, *19* (11), 1549-1561.
58. Sahu, I. D.; McCarrick, R. M.; Troxel, K. R.; Zhang, R.; Smith, H. J.; Dunagan, M. M.; Swartz, M. S.; Rajan, P. V.; Kroncke, B. M.; Sanders, C. R., DEER EPR Measurements for Membrane Protein Structures via Bifunctional Spin Labels and Lipodisq Nanoparticles. *Biochemistry* **2013**, *52* (38), 6627-6632.

59. Ganguly, S.; Weiner, B. E.; Meiler, J., Membrane protein structure determination using paramagnetic tags. *Structure* **2011**, *19* (4), 441-443.
60. Deber, C. M.; Wang, C.; Liu, L. P.; Prior, A. S.; Agrawal, S.; Muskat, B. L.; Cuticchia, A. J., TM Finder: a prediction program for transmembrane protein segments using a combination of hydrophobicity and nonpolar phase helicity scales. *Protein Science* **2001**, *10* (1), 212-219.
61. Jao, S.-C.; Ma, K.; Talafous, J.; Orlando, R.; Zagorski, M. G., Trifluoroacetic acid pretreatment reproducibly disaggregates the amyloid  $\beta$ -peptide. *Amyloid* **1997**, *4* (4), 240-252.
62. Chen, S.; Wetzel, R., Solubilization and disaggregation of polyglutamine peptides. *Protein Science* **2001**, *10* (4), 887-891.
63. Wosten, H. A.; De Vries, O. M.; Wessels, J. G., Interfacial self-assembly of a fungal hydrophobin into a hydrophobic rodlet layer. *The Plant Cell Online* **1993**, *5* (11), 1567-1574.
64. Talbot, N. J., Aerial morphogenesis: enter the chaplins. *Current Biology* **2003**, *13* (18), R696-R698.
65. Sen, V. D.; Golubev, V. A., Kinetics and mechanism for acid-catalyzed disproportionation of 2, 2, 6, 6-tetramethylpiperidine-1-oxyl. *Journal of Physical*

*Organic Chemistry* **2009**, 22 (2), 138-143.

66. Legardinier, S.; Raguénès-Nicol, C.; Tascon, C.; Rocher, C.; Hardy, S.; Hubert, J.-F.; Le Rumeur, E., Mapping of the lipid-binding and stability properties of the central rod domain of human dystrophin. *Journal of molecular biology* **2009**, 389 (3), 546-558.

67. Luo, P.; Baldwin, R. L., Mechanism of helix induction by trifluoroethanol: a framework for extrapolating the helix-forming properties of peptides from trifluoroethanol/water mixtures back to water. *Biochemistry* **1997**, 36 (27), 8413-8421.

68. Zhou, N.; Kay, C.; Hodges, R., Synthetic model proteins. Positional effects of interchain hydrophobic interactions on stability of two-stranded alpha-helical coiled-coils. *Journal of Biological Chemistry* **1992**, 267 (4), 2664-2670.

69. Cooper, T. M.; Woody, R. W., The effect of conformation on the CD of interacting helices: a theoretical study of tropomyosin. *Biopolymers* **1990**, 30 (7 - 8), 657-676.

70. Bessueille, L.; Sindt, N.; Guichardant, M.; Djerbi, S.; Teeri, T.; Bulone, V., Plasma membrane microdomains from hybrid aspen cells are involved in cell wall polysaccharide biosynthesis. *Biochem. J* **2009**, 420, 93-103.

71. Killian, J. A., Hydrophobic mismatch between proteins and lipids in membranes. *Biochimica et Biophysica Acta (BBA)-Reviews on Biomembranes* **1998**, 1376 (3), 401-416.

72. Wanjie, S. W.; Welti, R.; Moreau, R. A.; Chapman, K. D., Identification and quantification of glycerolipids in cotton fibers: reconciliation with metabolic pathway predictions from DNA databases. *Lipids* **2005**, *40* (8), 773-785.
73. Marsh, D.; Horváth, L. I., Structure, dynamics and composition of the lipid-protein interface. Perspectives from spin-labelling. *Biochimica et Biophysica Acta (BBA)-Reviews on Biomembranes* **1998**, *1376* (3), 267-296.
74. Vostrikov, V. V.; Koeppe, R. E., Response of GWALP transmembrane peptides to changes in the tryptophan anchor positions. *Biochemistry* **2011**, *50* (35), 7522-7535.
75. Scarpelli, F.; Drescher, M.; Rutters-Meijneke, T.; Holt, A.; Rijkers, D. T.; Killian, J. A.; Huber, M., Aggregation of transmembrane peptides studied by spin-label EPR. *The Journal of Physical Chemistry B* **2009**, *113* (36), 12257-12264.
76. Sepkhanova, I.; Drescher, M.; Meeuwenoord, N. J.; Limpens, R. W.; Koning, R. I.; Filippov, D. V.; Huber, M., Monitoring Alzheimer amyloid peptide aggregation by EPR. *Applied magnetic resonance* **2009**, *36* (2-4), 209-222.
77. Smirnov, A. I., Post-processing of EPR spectra by convolution filtering: calculation of a harmonics' series and automatic separation of fast-motion components from spin-label EPR spectra. *Journal of Magnetic Resonance* **2008**, *190* (1), 154-159.

78. Silvius, J., Thermotropic phase transitions of pure lipids in model membranes and their modifications by membrane proteins. *Lipid-protein interactions* **1982**, 2, 239-281.
79. Zhou, F. X.; Cocco, M. J.; Russ, W. P.; Brunger, A. T.; Engelman, D. M., Interhelical hydrogen bonding drives strong interactions in membrane proteins. *Nature Structural & Molecular Biology* **2000**, 7 (2), 154-160.
80. Schmid, A. W.; Condeelis, E.; Tuchscherer, G.; Chiappe, D.; Mutter, M.; Vogel, H.; Moniatte, M.; Tsybin, Y. O., Tissue transglutaminase-mediated glutamine deamidation of  $\beta$ -amyloid peptide increases peptide solubility, whereas enzymatic cross-linking and peptide fragmentation may serve as molecular triggers for rapid peptide aggregation. *Journal of Biological Chemistry* **2011**, 286 (14), 12172-12188.
81. Surewicz, W. K.; Mantsch, H. H.; Chapman, D., Determination of protein secondary structure by Fourier transform infrared spectroscopy: a critical assessment. *Biochemistry* **1993**, 32 (2), 389-394.
82. Smith, S. O.; Eilers, M.; Song, D.; Crocker, E.; Ying, W.; Groesbeck, M.; Metz, G.; Ziliox, M.; Aimoto, S., Implications of threonine hydrogen bonding in the glycoporphin A transmembrane helix dimer. *Biophysical journal* **2002**, 82 (5), 2476-2486.
83. Dong, A.; Matsuura, J.; Manning, M. C.; Carpenter, J. F., Intermolecular  $\beta$ -sheet results from trifluoroethanol-induced nonnative  $\alpha$ -helical structure in  $\beta$ -sheet predominant

proteins: infrared and circular dichroism spectroscopic study. *Archives of biochemistry and biophysics* **1998**, 355 (2), 275-281.

84. Dong, A.; Caughey, W. S.,[9] Infrared methods for study of hemoglobin reactions and structures. *Methods in enzymology* **1994**, 232, 139-175.

85. Smith, I. C.; Ekiel, I. H.,Phosphorus-31 NMR of phospholipids in membranes, Chapter 5. *Phosphorus-31 NMR: Principles and applications* **1984**, 447-474.

86. Seelig, J., <sup>31</sup>P nuclear magnetic resonance and the head group structure of phospholipids in membranes. *Biochimica et Biophysica Acta (BBA)-Reviews on Biomembranes* **1978**, 515 (2), 105-140.

87. Cullis, P. t.; De Kruijff, B.,Lipid polymorphism and the functional roles of lipids in biological membranes. *Biochimica et Biophysica Acta (BBA)-Reviews on Biomembranes* **1979**, 559 (4), 399-420.

88. Thayer, A. M.; Kohler, S. J.,Phosphorus-31 nuclear magnetic resonance spectra characteristic of hexagonal and isotropic phospholipid phases generated from phosphatidylethanolamine in the bilayer phase. *Biochemistry* **1981**, 20 (24), 6831-6834.

89. Lai, C.-S.; Hopwood, L. E.; Hyde, J. S.; Lukiewicz, S.,ESR studies of O<sub>2</sub> uptake by Chinese hamster ovary cells during the cell cycle. *Proceedings of the National Academy of*

*Sciences* **1982**, 79 (4), 1166-1170.

90. Marsh, D., Polarity and permeation profiles in lipid membranes. *Proceedings of the National Academy of Sciences* **2001**, 98 (14), 7777-7782.

91. Steinhoff, H.-J.; Pfeiffer, M.; Rink, T.; Burlon, O.; Kurz, M.; Riesle, J.; Heuberger, E.; Gerwert, K.; Oesterhelt, D., Azide reduces the hydrophobic barrier of the bacteriorhodopsin proton channel. *Biophysical journal* **1999**, 76 (5), 2702-2710.

92. Chen, X.; Sa'adedin, F.; Deme, B.; Rao, P.; Bradshaw, J., Insertion of TAT peptide and perturbation of negatively charged model phospholipid bilayer revealed by neutron diffraction. *Biochimica et Biophysica Acta (BBA)-Biomembranes* **2013**, 1828 (8), 1982-1988.

93. Lemkul, J. A.; Bevan, D. R., A comparative molecular dynamics analysis of the amyloid  $\beta$ -peptide in a lipid bilayer. *Archives of biochemistry and biophysics* **2008**, 470 (1), 54-63.

94. Berneche, S.; Nina, M.; Roux, B., Molecular dynamics simulation of melittin in a dimyristoylphosphatidylcholine bilayer membrane. *Biophysical journal* **1998**, 75 (4), 1603-1618.

95. Bachar, M.; Becker, O. M., Melittin at a membrane/water interface: effects on water orientation and water penetration. *The Journal of chemical physics* **1999**, 111 (18), 8672-

8685.

96. Bachar, M.; Becker, O. M., Protein-induced membrane disorder: a molecular dynamics study of melittin in a dipalmitoylphosphatidylcholine bilayer. *Biophysical journal* **2000**, *78* (3), 1359-1375.

97. Galdiero, S.; Falanga, A.; Cantisani, M.; Vitiello, M.; Morelli, G.; Galdiero, M., Peptide-lipid interactions: experiments and applications. *International journal of molecular sciences* **2013**, *14* (9), 18758-18789.

98. Griffith, O. H.; Jost, P., Lipid spin labels in biological membranes. *Spin Labeling Theory and Applications* **1976**, *1*, 453-523.

99. McConnell, H. M.; Hubbell, W. L., Molecular motion in spin-labeled phospholipids and membranes. *Journal of the American Chemical Society* **1971**, *93* (2), 314-326.

100. Jost, P.; Libertini, L. J.; Hebert, V. C.; Griffith, O. H., Lipid spin labels in lecithin multilayers. A study of motion along fatty acid chains. *Journal of molecular biology* **1971**, *59* (1), 77-98.

101. Knauer, B. R.; Napier, J. J., The nitrogen hyperfine splitting constant of the nitroxide functional group as a solvent polarity parameter. The relative importance for a solvent polarity parameter of its being a cybotactic probe vs. its being a model process. *Journal of*

*the American Chemical Society* **1976**, 98 (15), 4395-4400.

102. Hol, W. G.; Halie, L. M.; Sander, C.,Dipoles of the alpha-helix and beta-sheet: their role in protein folding. *Nature* **1981**, 294, 532-536.

103. Landolt-Marticorena, C.; Williams, K. A.; Deber, C. M.; Reithmeier, R. A.,Non-random distribution of amino acids in the transmembrane segments of human type I single span membrane proteins. *Journal of molecular biology* **1993**, 229 (3), 602-608.

104. Bañó-Polo, M.; Baeza-Delgado, C.; Orzáez, M.; Marti-Renom, M. A.; Abad, C.; Mingarro, I.,Polar/Ionizable residues in transmembrane segments: effects on helix-helix packing. *PloS one* **2012**, 7 (9), e44263.

105. Baeza-Delgado, C.; Marti-Renom, M. A.; Mingarro, I.,Structure-based statistical analysis of transmembrane helices. *European biophysics journal : EBJ* **2013**, 42 (2-3), 199-207.

106. Illergård, K.; Kauko, A.; Elofsson, A.,Why are polar residues within the membrane core evolutionary conserved? *Proteins: Structure, Function, and Bioinformatics* **2011**, 79 (1), 79-91.

107. Wong, W.-C.; Maurer-Stroh, S.; Eisenhaber, F.,Not all transmembrane helices are born equal: Towards the extension of the sequence homology concept to membrane proteins.

108. Zhou, F. X.; Merianos, H. J.; Brunger, A. T.; Engelman, D. M., Polar residues drive association of polyleucine transmembrane helices. *Proceedings of the National Academy of Sciences* **2001**, *98* (5), 2250-2255.

109. Gratkowski, H.; Lear, J. D.; DeGrado, W. F., Polar side chains drive the association of model transmembrane peptides. *Proceedings of the National Academy of Sciences* **2001**, *98* (3), 880-885.

110. Bechinger, B., Towards membrane protein design: pH-sensitive topology of histidine-containing polypeptides. *Journal of molecular biology* **1996**, *263* (5), 768-775.

111. Lew, S.; Ren, J.; London, E., The effects of polar and/or ionizable residues in the core and flanking regions of hydrophobic helices on transmembrane conformation and oligomerization. *Biochemistry* **2000**, *39* (32), 9632-9640.

112. Lew, S.; Caputo, G. A.; London, E., The effect of interactions involving ionizable residues flanking membrane-inserted hydrophobic helices upon helix-helix interaction. *Biochemistry* **2003**, *42* (36), 10833-10842.

113. Caputo, G. A.; London, E., Position and ionization state of Asp in the core of membrane-inserted  $\alpha$  helices control both the equilibrium between transmembrane and

nontransmembrane helix topography and transmembrane helix positioning. *Biochemistry* **2004**, *43* (27), 8794-8806.

114. Aisenbrey, C.; Goormaghtigh, E.; Ruyschaert, J.-M.; Bechinger, B., Translocation of amino acyl residues from the membrane interface to the hydrophobic core: thermodynamic model and experimental analysis using ATR-FTIR spectroscopy. *Molecular membrane biology* **2006**, *23* (4), 363-374.

115. Sparr, E.; Ash, W. L.; Nazarov, P. V.; Rijkers, D. T.; Hemminga, M. A.; Tieleman, D. P.; Killian, J. A., Self-association of transmembrane  $\alpha$ -helices in model membranes importance of helix orientation and role of hydrophobic mismatch. *Journal of Biological Chemistry* **2005**, *280* (47), 39324-39331.

116. Sheridan, R. P.; Levy, R. M.; Salemme, F.,  $\alpha$ -Helix dipole model and electrostatic stabilization of 4- $\alpha$ -helical proteins. *Proceedings of the National Academy of Sciences* **1982**, *79* (15), 4545-4549.

117. Hol, W.; Van Duijnen, P. T.; Berendsen, H., The  $\alpha$ -helix dipole and the properties of proteins. *Nature* **1978**, *273* (5662), 443-446.

118. Edgcomb, S. P.; Murphy, K. P., Variability in the pKa of histidine side - chains correlates with burial within proteins. *Proteins: Structure, Function, and Bioinformatics*

**2002**, *49* (1), 1-6.

119. Greenfield, N. J.; Fasman, G. D., Computed circular dichroism spectra for the evaluation of protein conformation. *Biochemistry* **1969**, *8* (10), 4108-4116.

120. Jost, P. C.; Griffith, O. H.; Capaldi, R. A.; Vanderkooi, G., Evidence for boundary lipid in membranes. *Proceedings of the National Academy of Sciences* **1973**, *70* (2), 480-484.

121. Marsh, D., Specificity of lipid-protein interactions. *Biomembranes: A Multi-Volume Treatise* **1995**, *1*, 137-186.

122. Ge, M.; Freed, J. H., Electron-spin resonance study of aggregation of gramicidin in dipalmitoylphosphatidylcholine bilayers and hydrophobic mismatch. *Biophysical journal* **1999**, *76* (1), 264-280.

123. Costa-Filho, A. J.; Crepeau, R. H.; Borbat, P. P.; Ge, M.; Freed, J. H., Lipid-gramicidin interactions: dynamic structure of the boundary lipid by 2D-ELDOR. *Biophysical journal* **2003**, *84* (5), 3364-3378.

124. Knowles, P. F.; Watts, A.; Marsh, D., Spin-label studies of lipid immobilization in dimyristoylphosphatidylcholine-substituted cytochrome oxidase. *Biochemistry* **1979**, *18* (21), 4480-4487.

125. Devaux, P. F.; Seigneuret, M., Specificity of lipid-protein interactions as determined by spectroscopic techniques. *Biochimica et Biophysica Acta (BBA)-Reviews on Biomembranes* **1985**, 822 (1), 63-125.
126. Griffith, O. H.; McMillen, D. A.; Keana, J. F.; Jost, P. C., Lipid-protein interactions in cytochrome c oxidase. A comparison of covalently attached phospholipid photo-spin label with label free to diffuse in the bilayer. *Biochemistry* **1986**, 25 (3), 574-584.
127. Dalton, L. A.; McIntyre, J. O.; Fleischer, S., Distance estimate of the active center of D-. beta.-hydroxybutyrate dehydrogenase from the membrane surface. *Biochemistry* **1987**, 26 (8), 2117-2130.
128. Kyrychenko, A.; Ladokhin, A. S., Molecular dynamics simulations of depth distribution of spin-labeled phospholipids within lipid bilayer. *The Journal of Physical Chemistry B* **2013**, 117 (19), 5875-5885.
129. Adamian, L.; Liang, J., Interhelical hydrogen bonds and spatial motifs in membrane proteins: polar clamps and serine zippers. *Proteins* **2002**, 47 (2), 209-18.
130. Choma, C.; Gratkowski, H.; Lear, J. D.; DeGrado, W. F., Asparagine-mediated self-association of a model transmembrane helix. *Nature Structural & Molecular Biology* **2000**, 7 (2), 161-166.

131. Mazzuca, C.; Orioni, B.; Coletta, M.; Formaggio, F.; Toniolo, C.; Maulucci, G.; De Spirito, M.; Pispisa, B.; Venanzi, M.; Stella, L., Fluctuations and the rate-limiting step of peptide-induced membrane leakage. *Biophysical journal* **2010**, *99* (6), 1791-1800.
132. Poojari, C.; Xiao, D.; Batista, V. S.; Strodel, B., Membrane Permeation Induced by Aggregates of Human Islet Amyloid Polypeptides. *Biophysical journal* **2013**, *105* (10), 2323-2332.
133. Hermansson, M.; von Heijne, G., Inter-helical hydrogen bond formation during membrane protein integration into the ER membrane. *Journal of molecular biology* **2003**, *334* (4), 803-809.
134. Chin, C.-N.; von Heijne, G., Charge pair interactions in a model transmembrane helix in the ER membrane. *Journal of molecular biology* **2000**, *303* (1), 1-5.
135. MacKenzie, K. R.; Prestegard, J. H.; Engelman, D. M., A transmembrane helix dimer: structure and implications. *Science* **1997**, *276* (5309), 131-133.
136. Javadpour, M. M.; Eilers, M.; Groesbeek, M.; Smith, S. O., Helix packing in polytopic membrane proteins: role of glycine in transmembrane helix association. *Biophysical journal* **1999**, *77* (3), 1609-1618.
137. White, S. H.; Wimley, W. C., Membrane protein folding and stability: physical

principles. *Annual review of biophysics and biomolecular structure* **1999**, 28 (1), 319-365.

138. Ben-Tal, N.; Honig, B., Helix-helix interactions in lipid bilayers. *Biophysical journal* **1996**, 71 (6), 3046-3050.

139. Sperotto, M. M., A theoretical model for the association of amphiphilic transmembrane peptides in lipid bilayers. *European biophysics journal* **1997**, 26 (5), 405-416.

140. Lear, J.; Gratkowski, H.; DeGrado, W., De novo design, synthesis and characterization of membrane-active peptides. *Biochemical Society Transactions* **2001**, 29 (Pt 4), 559-564.

141. Armstrong, D.; Zidovetzki, R.  
<http://rzlab.ucr.edu/scripts/wheel/wheel.cgi?sequence=ABCDEFGHIJKLMNOPS&submit=Submit>.

142. Harper, E. T.; Rose, G. D., Helix stop signals in proteins and peptides: the capping box. *Biochemistry* **1993**, 32 (30), 7605-7609.

143. Eswar, N.; Ramakrishnan, C., Deterministic features of side-chain main-chain hydrogen bonds in globular protein structures. *Protein engineering* **2000**, 13 (4), 227-238.

144. Worth, C. L.; Blundell, T. L., Satisfaction of hydrogen - bonding potential influences

the conservation of polar sidechains. *Proteins: Structure, Function, and Bioinformatics* **2009**, 75 (2), 413-429.

145. Schell, D.; Tsai, J.; Scholtz, J. M.; Pace, C. N., Hydrogen bonding increases packing density in the protein interior. *Proteins: Structure, Function, and Bioinformatics* **2006**, 63 (2), 278-282.

146. Budil, D. E.; Lee, S.; Saxena, S.; Freed, J. H., Nonlinear-least-squares analysis of slow-motion EPR spectra in one and two dimensions using a modified Levenberg–Marquardt algorithm. *Journal of Magnetic Resonance, Series A* **1996**, 120 (2), 155-189.

147. Gorbitz, C. H.; Etter, M. C., Hydrogen bonds to carboxylate groups. Syn/anti distributions and steric effects. *Journal of the American Chemical Society* **1992**, 114 (2), 627-631.

148. Gorbitz, C. H.; Etter, M. C., Hydrogen bonds to carboxylate groups. The question of three-centre interactions. *Journal of the Chemical Society, Perkin Transactions 2* **1992**, (1), 131-135.

149. Chaudhuri, A.; Halder, S.; Sun, H.; Koeppe, R. E., 2nd; Chattopadhyay, A., Importance of indole N-H hydrogen bonding in the organization and dynamics of gramicidin channels. *Biochimica et biophysica acta* **2014**, 1838 (1 Pt B), 419-28.

150. Yau, W.-M.; Wimley, W. C.; Gawrisch, K.; White, S. H., The preference of tryptophan for membrane interfaces. *Biochemistry* **1998**, *37* (42), 14713-14718.
151. Stoll, S.; Shafaat, H. S.; Krzystek, J.; Ozarowski, A.; Tauber, M. J.; Kim, J. E.; Britt, R. D., Hydrogen bonding of tryptophan radicals revealed by EPR at 700 GHz. *Journal of the American Chemical Society* **2011**, *133* (45), 18098-18101.
152. Daily, A. E.; Greathouse, D. V.; Van der Wel, P. C., Helical distortion in tryptophan- and lysine-anchored membrane-spanning  $\alpha$ -helices as a function of hydrophobic mismatch: a solid-state deuterium nmr investigation using the geometric analysis of labeled alanines method. *Biophysical journal* **2008**, *94* (2), 480-491.
153. Schreier-Muccillo, S.; Marsh, D.; Smith, I., Monitoring the permeability profile of lipid membranes with spin probes. *Archives of biochemistry and biophysics* **1976**, *172* (1), 1-11.
154. Nusair, N. A.; Mayo, D. J.; Dorozenski, T. D.; Cardon, T. B.; Inbaraj, J. J.; Karp, E. S.; Newstadt, J. P.; Grosser, S. M.; Lorigan, G. A., Time-resolved EPR immersion depth studies of a transmembrane peptide incorporated into bicelles. *Biochimica et Biophysica Acta (BBA)-Biomembranes* **2012**, *1818* (3), 821-828.
155. Subczynski, W. K.; Wisniewska, A.; Yin, J.-J.; Hyde, J. S.; Kusumi, A., Hydrophobic barriers of lipid bilayer membranes formed by reduction of water penetration by alkyl chain

unsaturation and cholesterol. *Biochemistry* **1994**, 33 (24), 7670-7681.

156. Killian, J. A.; Salemink, I.; de Planque, M. R.; Lindblom, G.; Koeppe, R. E.; Greathouse, D. V., Induction of nonbilayer structures in diacylphosphatidylcholine model membranes by transmembrane  $\alpha$ -helical peptides: importance of hydrophobic mismatch and proposed role of tryptophans. *Biochemistry* **1996**, 35 (3), 1037-1045.

157. de Planque, M. R.; Greathouse, D. V.; Koeppe, R. E.; Schäfer, H.; Marsh, D.; Killian, J. A., Influence of lipid/peptide hydrophobic mismatch on the thickness of diacylphosphatidylcholine bilayers. A  $^2\text{H}$  NMR and ESR study using designed transmembrane  $\alpha$ -helical peptides and gramicidin A. *Biochemistry* **1998**, 37 (26), 9333-9345.

158. Bayburt, T. H.; Sligar, S. G., Membrane protein assembly into Nanodiscs. *FEBS letters* **2010**, 584 (9), 1721-1727.

159. Ritchie, T.; Grinkova, Y.; Bayburt, T.; Denisov, I.; Zolnerciks, J.; Atkins, W.; Sligar, S., Reconstitution of membrane proteins in phospholipid bilayer nanodiscs. *Methods in enzymology* **2009**, 464, 211-231.

160. Bayburt, T. H.; Grinkova, Y. V.; Sligar, S. G., Self-assembly of discoidal phospholipid bilayer nanoparticles with membrane scaffold proteins. *Nano Letters* **2002**, 2 (8), 853-856.

161. Bayburt, T. H.; Sligar, S. G., Self - assembly of single integral membrane proteins into

soluble nanoscale phospholipid bilayers. *Protein science* **2003**, *12* (11), 2476-2481.

162. Denisov, I.; Grinkova, Y.; Lazarides, A.; Sligar, S., Directed self-assembly of monodisperse phospholipid bilayer Nanodiscs with controlled size. *Journal of the American Chemical Society* **2004**, *126* (11), 3477-3487.